



## Durham E-Theses

---

# *The Importance of Sintering with Crystals in Volcanic Regimes*

HAVARD, TEGAN,ALEXANDRA

### How to cite:

---

HAVARD, TEGAN,ALEXANDRA (2020) *The Importance of Sintering with Crystals in Volcanic Regimes*, Durham theses, Durham University. Available at Durham E-Theses Online:  
<http://etheses.dur.ac.uk/13663/>

### Use policy

---

The full-text may be used and/or reproduced, and given to third parties in any format or medium, without prior permission or charge, for personal research or study, educational, or not-for-profit purposes provided that:

- a full bibliographic reference is made to the original source
- a [link](#) is made to the metadata record in Durham E-Theses
- the full-text is not changed in any way

The full-text must not be sold in any format or medium without the formal permission of the copyright holders.

Please consult the [full Durham E-Theses policy](#) for further details.

---

Academic Support Office, Durham University, University Office, Old Elvet, Durham DH1 3HP  
e-mail: [e-theses.admin@dur.ac.uk](mailto:e-theses.admin@dur.ac.uk) Tel: +44 0191 334 6107  
<http://etheses.dur.ac.uk>

# The Importance of Sintering with Crystals in Volcanic Regimes

Tegan A. Havard

Master of Science by Research

Supervised by

Dr Katherine J. Dobson and Dr Fabian B. Wadsworth

January 2020

University of Durham, Department of Earth Sciences

# The Importance of Sintering with Crystals in Volcanic Regimes

Tegan A. Havard

## Abstract

Sintering, or welding, in silicic volcanic conduits limits outgassing, and outgassing from these conduits has a first order effect on determining the explosivity of an eruption (Cassidy et al., 2018). Crystals in volcanic systems can act as rigid inclusions; particles that are not involved in the sintering process but can have a significant effect on porosity and permeability. However, the role of crystals in sintering in a volcanological context has rarely been investigated previously. Here, analogue glass and crystal mixtures were sintered *in situ* using 4D x-ray tomography data collected in real time at the Diamond Light Source JEEP (i12) beamline synchrotron. This non-destructive technique captures high resolution 3D images at multiple points allowing the visualisation and quantification of interior and exterior changes. The data were processed using a 3D visualisation software to quantify porosity and connectivity.

When crystals are included in the starting mixture, the total porosity decreases, the disconnected porosity increases through the experiment, and the final porosity is higher with greater crystal content. The pore network preferentially disconnects through the z-axis first before pores are disconnected through other axes. A high connectivity is maintained to lower porosities (i.e. for a longer period of time) compared to crystal-free systems, suggesting that degassing is more efficient which may reduce the frequency of explosive events or quicken the transition to effusive behaviour. The results demonstrate that crystals do have an impact on sintering behaviour and further work is required to establish the effects of even greater crystal content and of different pressure conditions.

# Table of Contents

1. Introduction.....	8
1.1 Thesis Structure.....	13
2. Literature Review.....	14
2.1 Overview .....	14
2.2 Experimental methods.....	18
2.3 Sintering with rigid inclusion experiments .....	18
2.4 Sintering with rigid inclusion models .....	20
2.5 Sintering with and without rigid inclusions in volcanology .....	21
2.6 Tuffisite veins.....	23
3. Methodology and Methods .....	27
3.1 Sample Preparation .....	27
3.2 Imaging.....	29
3.3 High temperature <i>in situ</i> experiment on i12.....	29
3.4 Post-processing.....	32
3.4.1 Terminology .....	32
3.4.2. Initial processing and noise reduction .....	33
3.4.3 Quantifying porosity.....	35
3.4.3.1 Normalizing porosity .....	38
3.4.3.2 Connectivity.....	42
3.4.3.3 Pore population analysis .....	42
3.4.4 FIJI ImageJ Weka classification.....	43
3.4.5 Phases .....	47
3.4.6 Calculating volume fractions.....	51
3.4.7 Crystal particle analysis.....	52
3.4.8 Crystal interfaces .....	53
3.4.9 Digital Volume Correlation (DVC) analysis.....	55
4. Results.....	58
4.1 Quantified porosity.....	58
4.1.1 Total and disconnected porosities.....	58
4.1.2 Final porosities .....	79
4.1.3 Normalized porosity .....	80

4.1.4 Connectivity.....	83
4.1.5 Pore analysis .....	84
4.2 Volume fractions .....	89
4.3 Olivine analysis .....	92
4.3.1 Crystal interfaces .....	94
4.4 DVC .....	95
4.4.1 Experiment 10_880.....	95
4.4.2 Experiment 30_860.....	98
5. Discussion .....	101
5.1 Discussion of results.....	101
5.1.1 Overall, disconnected, and final porosities.....	101
5.1.2 Normalised data .....	105
5.1.3 Connectivity.....	108
5.1.4 Pore analysis .....	109
5.1.5 Volume fractions .....	110
5.1.6 Olivine analysis .....	111
5.1.7 DVC discussion .....	114
5.2 Crystals in experiments and nature .....	115
5.2.1 Volcanic processes .....	115
5.2.1.1 Tuffisite veins and crystals .....	116
5.2.1.2 Welded ignimbrites.....	119
5.2.2 Experiments to nature .....	119
5.2.2.1 Particle size distribution.....	120
5.2.2.2 Geochemistry .....	121
6. Conclusions.....	122
Appendix.....	124
References.....	128

# Nomenclature

$a_i$	Initial pore size [m].
$C$	Connectivity.
$C_p$	Heat capacity [J/kg/°K].
$\eta$	Viscosity with suspended particles [Pa.s].
$\varphi$	Porosity.
$\varphi'$	Connected porosity.
$\varphi_c$	Percolation threshold.
$\varphi_i$	Initial porosity.
$\varphi_m$	Maximum packing fraction.
$\varphi_{pvol}$	Total volume fraction of all phases.
$\varphi_x$	Crystal volume fraction.
$\varphi_{xvol}$	Total crystal volume fraction.
$\bar{\varphi}$	Normalized porosity.
$M_g$	Mass of glass.
$M_{xl}$	Mass of crystal.
$\mu$	Viscosity [Pa.s].
$N_e$	Number of voxels of material in the exterior.
$N_s$	Number of voxels of selected material.
$\rho_g$	Density of glass.
$\rho_{xl}$	Density of crystal.
$r_p$	Aspect ratio.
$t$	Time [s].
$t_i$	Initial time [s].
$\bar{t}$	Dimensionless time.
$T$	Temperature [°C or °K].
$\Gamma$	Surface tension [N.m <sup>-1</sup> ].

# Declaration

I declare that this thesis which is presented for the degree of Master of Science by Research at the University of Durham is the result of my own original research, except where acknowledgement is made in the text. This thesis has not been previously submitted to the University of Durham or any other institution.

*The copyright of this thesis rests with the author. No quotation from it should be published without the author's prior written consent and information derived from it should be acknowledged.*



## Acknowledgements

To my supervisors, Kate and Fabian, thank you for the support, for the opportunity, and for the patience throughout this project. Through your knowledge and enthusiasm, I have learned so much and I am a better scientist for it.

The friends I have made in the department over the last year, my time in Durham would not have been the same without you all. Thank you for all the laughs and for helpfully eating all of the cakes I baked. I am grateful to my friends from undergraduate and before, to those I have seen and those I have not, it has been a blast catching up over the year. And to Jack, thank you for your patience and support.

I am incredibly lucky to have such a loving and supporting family who have been there for me throughout this work and beyond. To all of the family, but especially Mom, Dad, and Kieran, thank you.



*Ohana*

# 1. Introduction

Silicic volcanoes are dangerous because they are far more likely to erupt in an explosive manner; the eruptions highest on the Volcanic Explosivity Index (VEI) scale are almost exclusively silica rich (Newhall and Self, 1982; Mason et al., 2004). Through explosive volcanic activity, the magma fragments into particles which can be followed by sintering, or welding, in volcanic conduits (e.g. Gonnerman and Manga, 2003), ignimbrites (e.g. Branney et al., 1992), vent-filling proximal deposits (e.g. Kolzenberg et al., 2012), tuffisite veins (e.g. Tuffen et al., 2003), or in aeroplane jet engine hot zones (Giehl et al., 2017; Figure 1.1).

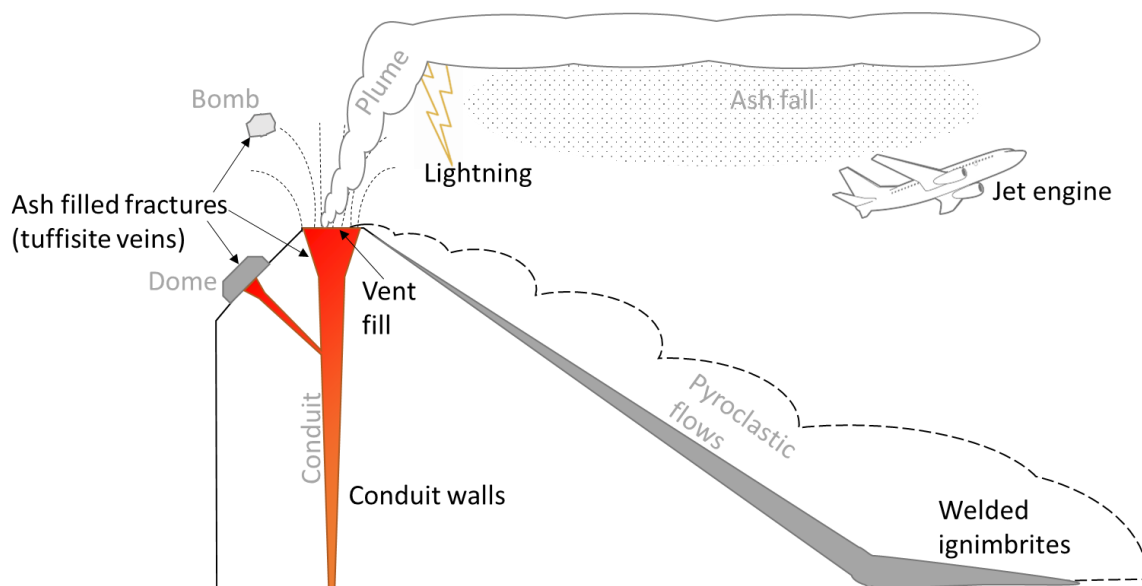


Figure 1.1: Graphic illustrating example locations of sintered volcanic material.

Sintering is the process by which particles soften and coalesce without turning into liquid (Figure 1.2).

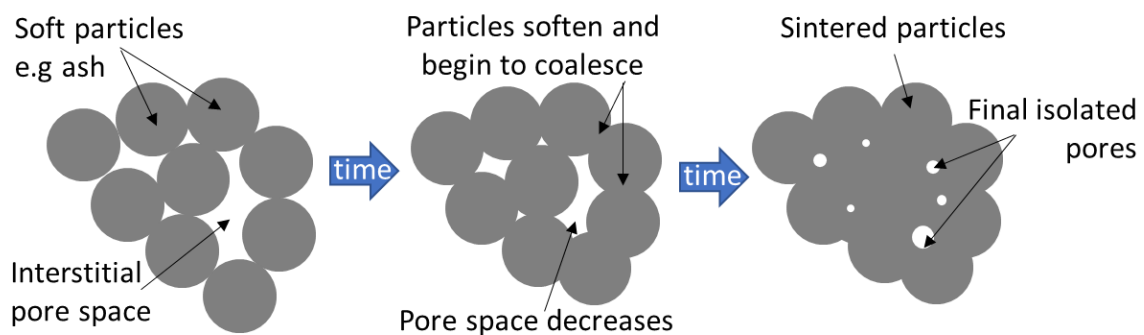
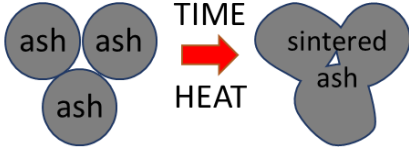
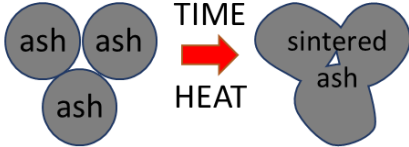
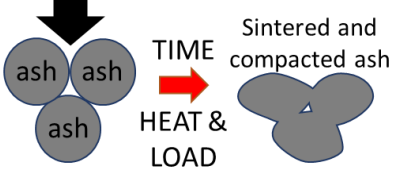
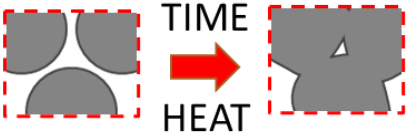
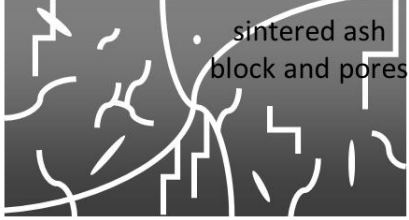
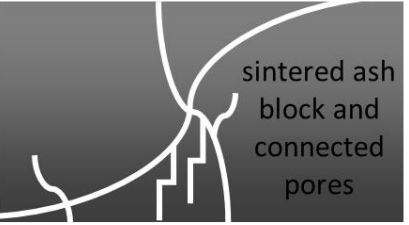

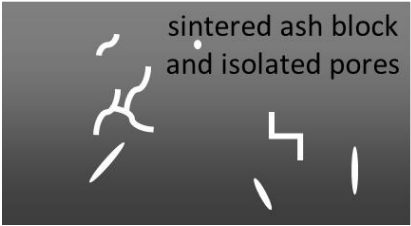
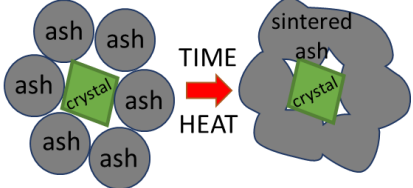


Figure 1.2 The evolution of sintering particles over time. Modified from Wadsworth (2016).

Key terms used throughout this work are defined and illustrated where possible in Table 1.1.

Term	Definition	Diagrams
Sintering*	The process by which particles soften and coalesce without turning into liquid e.g. ash welding together.	
Welding *	The process of joining together particles through softening of surfaces in contact. *Note: sintering and welding are used interchangeably in the literature and in this work.	
Compaction	The sintering or welding of particles by an external force or load e.g. ash flow deposit compacting under its own weight.	
Densification	The loss of void space through processes such as sintering and compaction.	
Porosity (total porosity)	A measure of all of the empty spaces in a material e.g. the pores in a sintered deposit. This is displayed as a fraction of the total volume.	
Connected porosity	A measure of pores where both ends are connected to the outside (outside of the sintered material) e.g. fractures that are connected between the top and bottom of a welded deposit. Displayed as a fraction of total volume.	
Disconnected porosity	A measure of pores that are connected to the outside but not connected fully across a sintered deposit e.g. pores that	

	do not connect the top and bottom of a sintered deposit.	
Isolated porosity	Pores that are not connected to the outside of a deposit at all.	
Pore network	The framework through which fluids can flow.	
Permeability	The ability of a material to allow liquids or gases to pass through.	
Rigid inclusions	Particles that take up physical space in a sintering area but do not sinter themselves e.g. olivine crystals are not affected at lower temperatures that affect ash.	
Table 1.1: The definitions of key terms and accompanying cartoons describing the key terms.		

Sintering in silicic volcanic conduits is a key process in limiting outgassing which in turn has a first order effect determining the explosivity of an eruption (Cassidy et al., 2018). The sintering of particles can reduce the permeability, porosity, and change permeable gas routes. Pore networks can densify and become isolated pores, allowing pressure to build in the volcanic conduit as gas is prevented from escaping (e.g. Kendrick et al., 2016; Saubin et al., 2016). The pressure would increase until an explosive event took place, resetting the system for another cycle of sintering. Sintering occurs in tuffisite veins that form in the upper section of a conduit, which may be particularly important for the transition from explosive to effusive behaviour, allowing volatiles to escape and slow or prevent the build-up of pressure (e.g. Stasiuk et al., 1996; Tuffen et al., 2003; Castro et al., 2012; Schipper et al., 2013; Kendrick et al., 2016; Gardner et al., 2018; Figure 1.3).

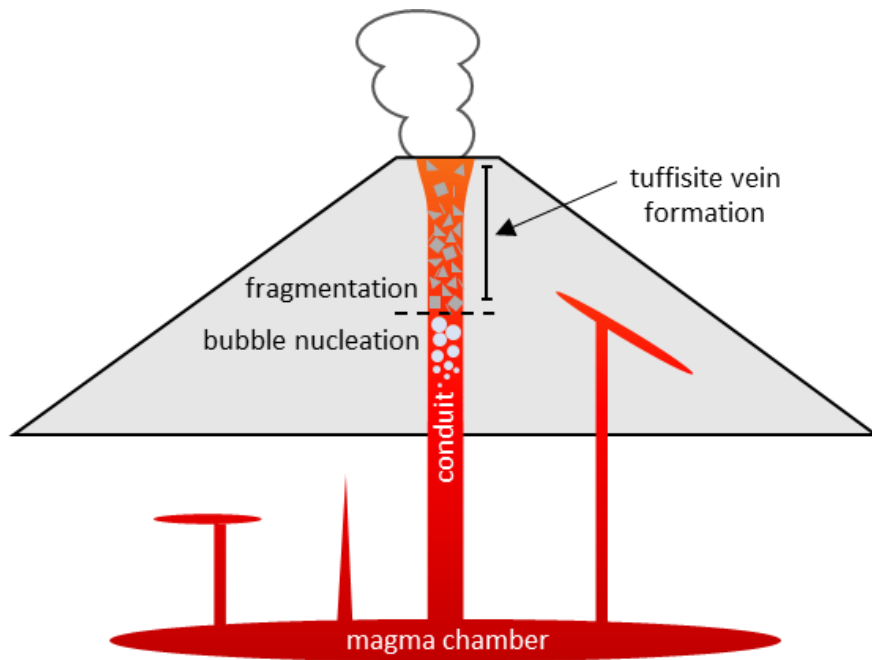


Figure 1.3: Volcanic conduit showing path from magma chamber to surface. Fragmentation and tuffisite vein formation occur in the upper part of the conduit and in domes. Modified from Saubin et al (2016) and Fagents et al (2012; pp 55-84).

Tuffisite veins form when fragmented melt is transported along fracture networks by a fluid phase and deposited within fractures. Glassy material can weld if temperature conditions remain above the glass transition temperature,  $T_g$  (Figure 1.4).

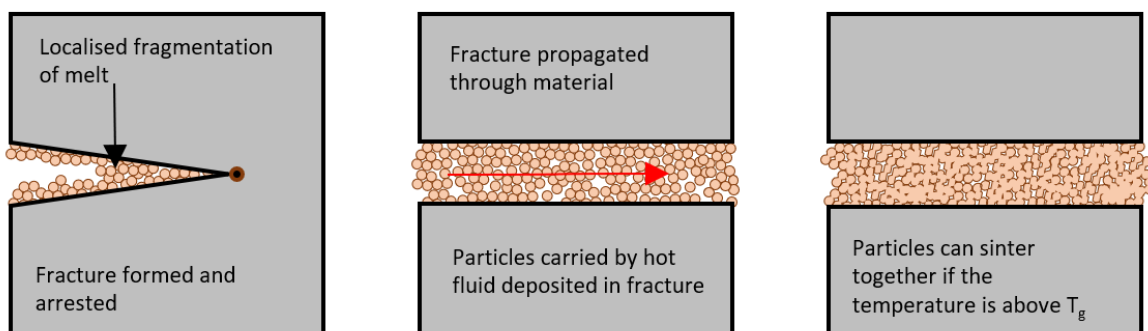


Figure 1.4. A closer view of tuffisite vein formation. Hot fluid carrying fragmented material travels through fractures or may even produce fractures. Particles are deposited into the vein and sinter if temperature is high enough. Modified from Kendrick 2016.

Crystals are near ubiquitous in volcanic systems. They shed light on the inner workings of volcanoes, capturing the conditions of magma formation and storage. The evolution of conditions such as temperature, pressure, time, and volatile content can be recorded in

zonations of crystals (e.g. Ubide and Kamber, 2018). They also have physical effects upon melt rheology, increasing the viscosity with increased crystal content (e.g. Costa, 2005) and forming frameworks that allows gas to escape (e.g. Lindoo et al., 2017). In sintering mixtures, if the temperature and pressure conditions are high enough, the crystals can undergo solid-state sintering under volcanic conditions (Ryan et al., 2018). At lower temperatures and pressures, and shorter timescales, they can act as rigid inclusions. The presence of rigid inclusions in a sintering mixture can have a dramatic effect on the porosity and permeability compared to a system free of rigid inclusions (e.g. Kolzenburg et al., 2012; Heap et al., 2014). This is important when considering sintering in silicic volcanic systems where crystals, either phenocrysts that are transported out of the magma chamber by magma or those crystallising out of the melt, can behave as these rigid inclusions.

The material sciences community dominate investigations into sintering. Research on sintering with rigid inclusions is limited, and only a few studies even then are relevant to volcanology. Two key papers come from Eberstein et al (2009) and Amoros et al (2019). Both use sintering experiments with crystals that act as rigid inclusions and glass matrices that have a silica composition similar to more evolved magmas. They find that the final porosity is affected by the crystals and that the sintering process is delayed when compared to a crystal-free mixture. Also, with a higher proportion of crystals, the above effects become more pronounced; the final equilibrium porosity increases and sintering rate decreases with increasing crystalline content.

Sintering in volcanology is a growing area of research (e.g. Grunder and Russell, 2005 and refs within; Vasseur et al., 2013; Heap et al., 2014; Ryan et al., 2018; Gardner et al., 2018; Wadsworth et al., 2019) and sintering with rigid inclusions, although a critical process in volcanology, has rarely been the focus of investigations (e.g. Heap et al., 2014; Colombier et al., 2020). As crystals are almost ubiquitous in volcanic systems, this subject needs further study.

With such abundant material that can potentially behave as rigid inclusions, it is likely they affect the sintering process and are not currently accounted for in numerical models. In addition, stress and temperature conditions that favour both magma fragmentation and sintering are not unusual in conduits (Gonnerman and Manga, 2003). This indicates that sintering with rigid inclusions is likely far more prevalent in the volcanic system than currently realised and needs to be investigated. Much has been learned from the sintering of crystal-free melts and it

is now we should shift the focus to multiphase melts and understanding the role of the rigid inclusion fraction.

A material sciences approach to studying volcanological phenomenon allows us to develop a quantitative understanding and allow testing of numerical models that can predict behaviour. To investigate the role of rigid inclusions, *in situ* sintering experiments are run with different glass-crystal mixtures to determine both how the presence of crystals affects the final equilibrium porosity, and the role crystal content has on reducing the sintering rate. Non-destructive X-ray computed tomography (XCT) was used to capture the evolution of sintering samples with different crystal contents. The data allow tracking of porosity, a proxy for the effect of crystals because the behaviour of crystal-free samples has already been determined (Wadsworth et al., 2016).

## **1.1 Thesis Structure**

This thesis presents an overview of the sintering literature (Chapter 2) focussing on areas relevant to volcanic application, and the limited work on sintering with rigid inclusions. It then presents the methodology used for the experiments and the processing of data (Chapter 3), before presenting the results and initial discussions of the study (Chapter 4), comprehensive discussions and their implications (Chapter 5), and the final conclusions (Chapter 6).

## 2. Literature Review

### 2.1 Overview

Sintering is important in volcanic regimes because it affects properties such as porosity and permeability which in turn have a direct impact on the efficiency of outgassing (e.g. Cassidy et al., 2018). Degassing of the magma through outgassing mechanisms is a key factor in determining eruption style and whether an eruption will be effusive or explosive (e.g. Cabrera et al., 2015).

Ignimbrites become denser if welding takes place, and emplacement conditions can be estimated from the grade of welding (e.g. Quane and Russell, 2005). Ash particles can sinter within jet engines and cause significant damage (e.g. Giehl et al., 2017). In the conduit, sintering can weld shut pore networks, stopping outgassing and allowing pressure to build (e.g. Castro et al., 2012). It can also restore strength to fractured material (e.g. Kolzenburg et al., 2012). The collective understanding of sintering is now well established and with interest growing, the role of crystals in sintering mixtures must now be further investigated.

The material sciences community dominate investigations into sintering because they can extensively tailor material properties by combining sintering processes and a wide selection of available starting materials. Much of the research is not applicable in a volcanological context when temperatures (much lower or higher than that expected in a volcanic setting), materials (e.g. metals; Jagota et al., 1992), and sintering method (e.g. microwave sintering; Minay et al., 2005) are considered. A large section of research into sintering, or welding, in volcanology focusses on welded ignimbrites (e.g. Smith, 1960; Riehle, 1973; Branney et al., 1992; Streck and Grunder, 1995, Sparks et al., 1999; Quane and Russell, 2005; Sumner and Branney, 2002; Grunder and Russell, 2005; Andrews and Branney, 2011). Other sintering locations include volcanic conduits (e.g. Gonnerman and Manga, 2003; Rust et al., 2004; Gardner et al., 2018), vent-filling proximal deposits (e.g. Kolzenberg et al., 2012; Ashwell et al., 2015; Hornby et al., 2015; Kendrick et al., 2016), tuffisite veins (e.g. Tuffen et al., 2003; Kendrick et al., 2016; Gardner et al., 2018), aeroplane jet engine hot zones (Giehl et al., 2017; Song et al., 2017) and lightning striking volcanic ash (Cimarelli et al., 2017; Mueller et al., 2018). Interest in the physics and kinetics behind sintering applicable to volcanology has increased in the last few years (Vasseur et al., 2013; Wadsworth et al., 2014; Wadsworth, 2016; Wadsworth et al., 2019).



Sintering with rigid inclusions is a limited topic within sintering research. Potential uses being investigated in material science include stabilising complex 3D printed geometries through sintering for bone and tissue replacement (Winkel et al., 2012), enabling integration of wiring and other components into low temperature co-fired ceramics (LTCC; Eberstein et al., 2009), and matching the sintering properties of a multi-layer product (Yan et al., 2013). Experiments and models that investigate glass matrix composites (GMC) are relevant and potentially applicable to volcanology. However, they must be assessed on a case by case basis as most studies are restricted to specific limitations of powder morphology and composition which makes this area of research quite empirical (Eberstein et al., 2009). In volcano science, sintering with rigid inclusions has rarely been the focus of sintering investigations, generally only present as a footnote to indicate that this is an area in need of further research (Wadsworth 2016; Colombier et al., 2020). This is despite numerous studies of sintered volcanic system products from across the world identifying a crystal fraction (Figure 2.1; Table 2.1).

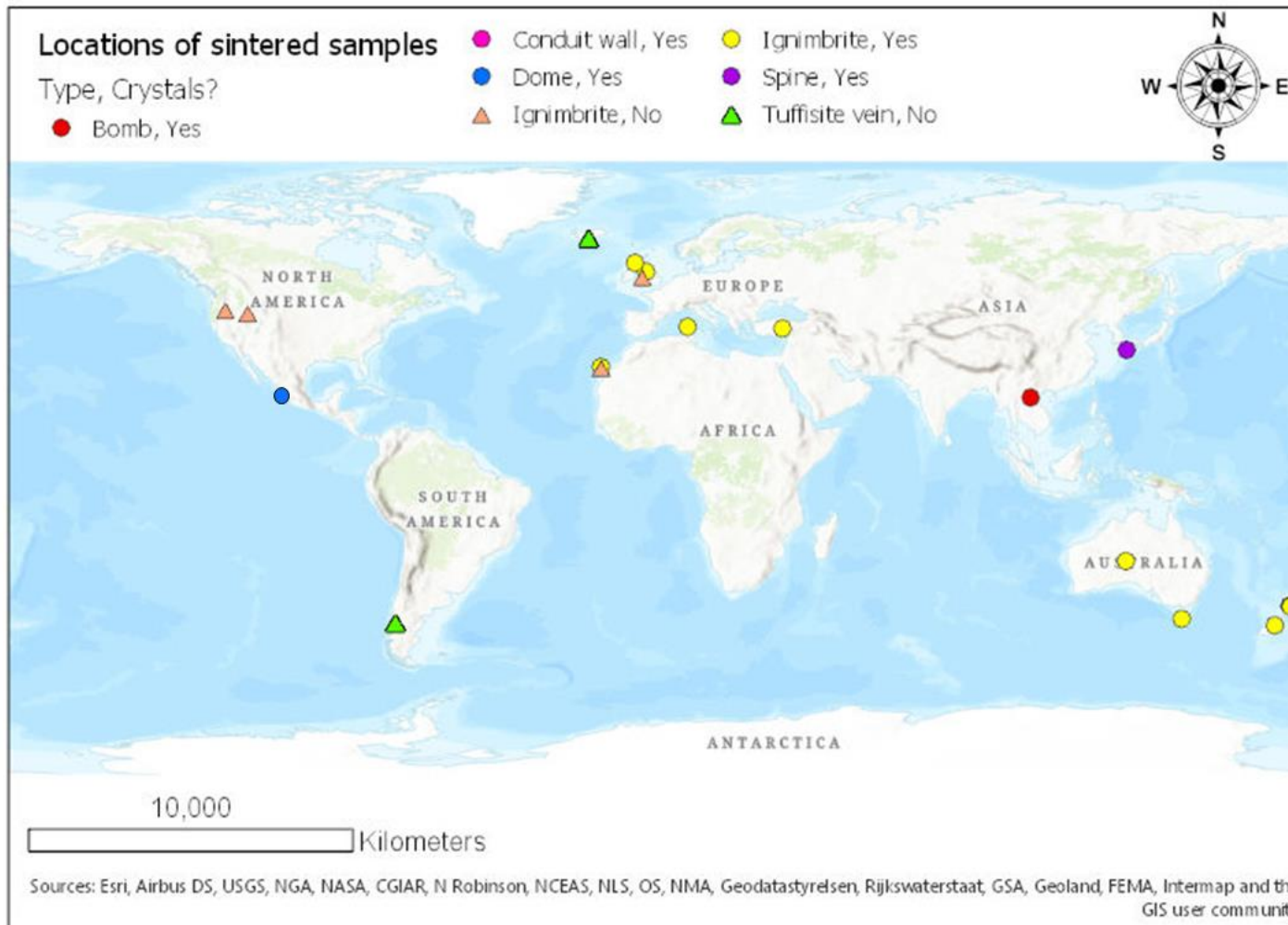


Figure 2.1: A map showing the locations of some selected welded deposits for which studies into the sintering dynamics exist. Red circle = volcanic bomb, with crystals. Pink circle = conduit wall, with crystals. Blue circle = volcanic dome, with crystals. Orange triangle = ignimbrites, no crystals. Yellow circle = ignimbrites, with crystals. Purple circle = spine, with crystals. Green triangle = tuffisite vein, no crystals.

<b>Name</b>	<b>Crystal content (%)</b>	<b>Composition</b>	<b>Type</b>	<b>Reference</b>
<b>Colima</b>	Contains crystals, n/a	Andesite	Bomb	Farquharson et al., 2016
<b>Colima</b>	~59	Andesite	Dome	Kendrick et al., 2016
<b>Ngongotaha</b>	4	-	Dome	Ashwell et al., 2015
<b>Ruawahia</b>	65	-	Dome	Ashwell et al., 2015
<b>Tarawera</b>	25	Rhyolitic	Conduit wall	Schauroth et al., 2016
<b>Whakamaru</b>	52	Rhyolitic	Ignimbrite	Briggs 1976
<b>Bad Step Tuff</b>	10	High-K calc-alkaline	Ignimbrite	Branney et al., 1992
<b>Ignimbrite E</b>	18	Peralkaline rhyolite	Ignimbrite	Leat and Schminke 1993
<b>Mount Somers</b>	24	Calc-alkaline	Ignimbrite	Smith and Cole 1997
<b>Zig Zag Hill</b>	20	Rhyolite	Ignimbrite	White and McPhie 1997
<b>Nuraxi</b>	20	Rhyolitic	Ignimbrite	Pioli and Rosi 2005
<b>Incesu</b>	31	Dacitic	Ignimbrite	Lepetit et al., 2009
<b>Sgurr of Eigg</b>	15	Trachydacitic	Ignimbrite	Brown and Bell 2013
<b>Kathleen</b>	25	A-type, metaluminous	Ignimbrite	Medlin et al., 2015
<b>Ignimbrite P1</b>	0	Basaltic	Ignimbrite	Freundt and Schminke 1995
<b>Rattlesnake Tuff</b>	1	High silica rhyolite to alkalic dacite	Ignimbrite	Streck and Grunder 1995
<b>Pitts Head Tuff</b>	5	Peralkaline rhyolitic	Ignimbrite	Kokelaar and Koniger 2000
<b>Ignimbrite TL</b>	5	Rhyolite to trachyte	Ignimbrite	Sumner and Branney 2002
<b>Grey's Landing Member</b>	1	Metaluminous	Ignimbrite	Andrews and Branney 2011
<b>Torfajokull</b>	0	Rhyolite	Tuffisite vein	Tuffen et al., 2003
<b>Chaiten</b>	0	Rhyolite	Tuffisite vein	Castro et al., 2012
<b>Unzen</b>	30	Dacitic	Spine	Hornby et al., 2015
<b>Ignimbrite D</b>	15	Pantelleritic rhyolite	Ignimbrite	Kobberger and Schminke 1999

Table 2.1: Crystal content, composition, and type of some selected welded deposits.

## 2.2 Experimental methods

The original method of investigating sintering was the loaded dilatometry technique where a sample was compacted by push rods or a piston, and shrinkage and temperature recorded throughout the experiment (e.g. De Jonghe and Rahaman, 1984). This was replaced by heating microscopy which enabled monitoring without applying an external load (Boccaccini et al., 1997). This produced improved measurements over that of previously used loaded dilatometer experiments, as the load applied by the dilatometer technique produces large errors due to contact with the sample (Jagota, 1990; Dutton, 1992). Therefore, any experiments using a loading dilatometer are unsuitable for this project as they describe sintering under loading conditions which is not being investigated here. More recent methods include optical dilatometry which tracks the changes in the silhouette of the sample as it sinters and shrinks. The shrinkage is calibrated against the initial and final porosity calculated from pycnometry and SEM images respectively (e.g. Vasseur et al., 2013; Wadsworth et al., 2016). Synchrotron XCT captures 4D data, imaging the interior and exterior of the sample at multiple points throughout the experiment which can then be visualised and manipulated in 3D using appropriate software (e.g. Wadsworth et al., 2019; Colombier et al., 2020; Dobson et al., in review).

Any of the methods described previously can be used to sinter samples that include rigid inclusions. However, synchrotron XCT is necessary to relate changes in sintering behaviour to the presence of rigid inclusions as it is the only method that captures data *in situ*, in 4D, and in a non-destructive manner.

## 2.3 Sintering with rigid inclusion experiments

From experiments with crystals as rigid inclusions included in the sintering mixture, the sintering rate decreases, the amount the sample shrinks by decreases, and increasing crystal content amplifies both of these effects (Bouvard, 2000; Muller et al., 2007; Eberstein et al., 2009; Winkel et al., 2012; Yan et al., 2013; Amoros et al., 2019). Equivalently, the density does not increase as much while sintering with rigid inclusions compared to inclusion free samples (Boccaccini et al., 1997). In the early stages of sintering, the crystals do not change sintering behaviour compared to glass alone (Eberstein et al., 2009) but this may change with crystal content  $\geq 20$  vol% (Winkel et al., 2012). Crystal contents  $>15$  vol% reduce the final attainable shrinkage and rigid inclusion content  $>53$  vol% changes the sintering behaviour

again, likely towards solid-state sintering behaviour (Eberstein et al., 2009; Amoros et al., 2019; Ryan et al., 2018).

Porosity loss can describe the degree of sintering, with crystal-free fully sintered samples reaching a final equilibrium porosity of  $\sim 0.03$  (Wadsworth et al., 2016). Because rigid inclusions reduce the final attainable shrinkage, the final equilibrium porosity should be greater with more rigid inclusions. Over the course of an experiment, isolated pores grow in size and small pores are eliminated. This changes the porosity character of the sample from many but small pores at the start to few but larger pores at the end which becomes more pronounced with more crystals, probably due to differences in sintering rates caused by these heterogeneities (Amoros et al., 2019). The connectivity of pores also diminishes as samples sinter and has been estimated previously using the difference between total and connected porosity (using a combination of density measurements and pycnometry), from SEM images of the sintered end product (Eberstein et al., 2009; Winkel et al., 2012; Vasseur et al., 2013; Amoros et al., 2019), and using XCT (Colombier et al., 2017). With rigid inclusions, isolated porosity appears to develop earlier in the sintering process for rigid inclusion content  $>53$  vol% (Amoros et al., 2019).

The size of the particles used in sintering samples potentially have an effect on sintering. Experiments in material science typically use small particle sizes, between 1 and 15  $\mu\text{m}$ . The sizes of the glass matrix particles and crystal particles can be the same (e.g. Eberstein et al., 2009; Winkel et al., 2012), the matrix particles larger than the inclusion particles (e.g. Winkel et al., 2012; Amoros et al., 2019), or the rigid inclusions larger than the matrix particles (e.g. Rahaman and Dejohnge, 1987). Larger rigid inclusions than glass particles result in a more densified sample and a greater effect on slowing sintering because the microstructure is more homogeneous as glass better packs around the crystals (Jean and Gupta, 1992; Yan et al., 2013). The shape of the particles also affects sintering rate. Jagged particles sinter faster than spherical particles of the same size (Cutler and Hendricksen, 1968; Giess et al., 1984; Giess et al., 1985).

Across the various experiments, there is not always agreement. Amoros et al (2019) found that experimentally determined diametral and axial shrinkage were very similar which agrees with findings in Ducamp and Raj (1989) but disagrees with findings from Boccaccini et al (1995). The most likely explanation for this difference is the  $\text{SiO}_2$  content of the material used in the experiments. The two in agreement used more silica rich glass, 68 wt% and 58 wt% respectively, compared to 48 wt% and therefore have higher viscosities than the lower silica

glass which may explain the difference in shrinkage. An alternative theory is the shape of the particles affected the sintering behaviour as non-spherical particles prefer radial shrinkage in early stages and axial shrinkage later (Muller et al., 2007). Another possibility is the mixing of the glass and rigid inclusions, with anisotropic sintering behaviour linked to anisotropic mixing of material (Boccaccini and Olevsky, 1999; Boccaccini and Conradt, 2001). Eberstein et al (2009) also found differences between the two shrinkages and suggested radial shrinkage starts earlier because of anisotropic features in the microstructure, but admitted that it is not yet understood why this happens and why crystal content changes the rates of axial versus diametral shrinkage.

#### **2.4 Sintering with rigid inclusion models**

Most of the models that are used to explain the behaviour of sintering with rigid inclusions fail to predict the behaviour with large inclusion fractions or were originally intended for sintering without inclusions.

Early theoretical work by Frenkel (1945) describing sintering in terms of the formation of necks between particles, and Mackenzie and Shuttleworth (1949) describing the sintering of isolated pores, underlies many subsequent studies. The model of Winkel et al (2012) used Frenkel for early stages of sintering and Mackenzie-Shuttleworth for later sintering stages for example.

Bordia and Raj (1986) predicted that sintering of glass with rigid inclusions should be similar to that of glass alone. They assume that the rigid inclusions are isolated within the glass matrix and so their model predicts behaviour until the rigid inclusion content is high enough that they come into contact with one another.

Scherer (1987) and Scherer (1988) describe sintering with rigid inclusions, predicting that sintering is retarded by the internal stresses the inclusions put on the matrix, but are only appropriate for up to ~10% inclusion content and where the inclusions are much larger than matrix particles. Higher rigid inclusion fraction experiments show large deviations from the models (Rahaman and Dejohnge, 1987). Bordia and Scherer (1988) indicate the deviations from the model can be attributed to the internal stresses caused by the rigid inclusions creating crack-like defects. Another issue with Scherer (1987) is the prediction of low internal stresses arising because of inclusions, but there is disagreement with the values by up to two orders of magnitude (Bordia and Scherer 1988; Raj and Bordia 1984; Hsueh et al., 1986; Boccaccini, 1998). The sintering with rigid inclusion model of Muller et al (2007) requires a constant

heating rate, identically sized glass and inclusion particles, and works up to 35% inclusion content.

The range of models available from material science provide a basic framework that allow application to volcanic regimes, but the complexities that arise from nature are not always accounted for. One such complexity is temperature; it is unlikely to stay constant in a volcanic setting, so non-isothermal models are required to describe this behaviour. Wadsworth et al (2014) produced a non-isothermal viscous sintering model for volcanic ash that described the experimental data accurately, and Amoros et al (2019) described a kinetic non-isothermal sintering model in which sintering develops via particle rearrangement by viscous flow. The experimental results fitted the model well up until 43 vol% inclusion content, but with  $\geq 53$  vol%, the results fitted well only at the start of the curve. The vented bubble model of Wadsworth et al (2016) describes viscous sintering of polydisperse particle distributions and Wadsworth et al (2019) produced a model for the welding of ash particles that combines sintering and water diffusion.

## **2.5 Sintering with and without rigid inclusions in volcanology**

Phenocrysts in magmas could behave as rigid inclusions in the sintering process. The crystal content also has a large effect on magma rheology in general, (e.g. Costa, 2005; Petford, 2009) with an increase of crystals increasing the bulk viscosity.

In volcanology, there have been experimental studies that investigated viscous sintering of glass particles under volcanic conduit conditions (Vasseur et al., 2013; Wadsworth et al., 2014; Wadsworth et al., 2019). Grunder and Russel (2005) summarised the understanding of welding processes in volcanology at the time, referencing a range of welding studies, but none that specifically looked at the effect of crystal content (see refs within Grunder and Russel 2005). Many welding studies focus on pyroclastic deposits and so sintering experiments incorporate compacting conditions (Heap et al., 2014 and example refs within). Gardner et al (2018) investigated viscous sintering of natural glassy material (ash) at shallow conduit conditions at 20-40MPa. At the other end of the spectrum is solid-state sintering of crystals under conduit conditions of 40-70MPa (Ryan et al., 2018). Both end members result in densification (the loss of pore space), but the glass through softening of particles, and the crystal through atomic diffusion between grain boundaries (Rahaman, 2003). Experiments were run at comparable

temperatures (700-900°C) with a full loss of permeability occurring over hours to days for the glass and over weeks to months for the crystals.

There are few experimental studies that span the gap between these two end members. Quane et al (2009) and Heap et al (2014) welded samples under comparable compacting conditions, the former with 1 vol% crystal content and the latter with 25 vol% crystal content. The presence of crystals did not impact the ability of samples to weld as long as the melt phase remained above  $T_g$  for a sufficient amount of time for viscous sintering. Colombier et al (2020) compared sintering between two samples with 0 and 40 vol% crystal content and found that the percolation threshold,  $\phi_c$ , increased with crystal content. These works provide a value for one discrete crystal content but there is a lack of volcanological studies where crystal content is systematically increased and the effect on sintering investigated. From material science, there are two studies that examine the effects of differing rigid inclusion content on sintering samples (Eberstein et al., 2009; Amoros et al., 2019). This denotes the importance of this study and is displayed in Figure 2.2 which details the current experimental investigations of sintering as a volcanological process and where this work fits in the sintering regime.



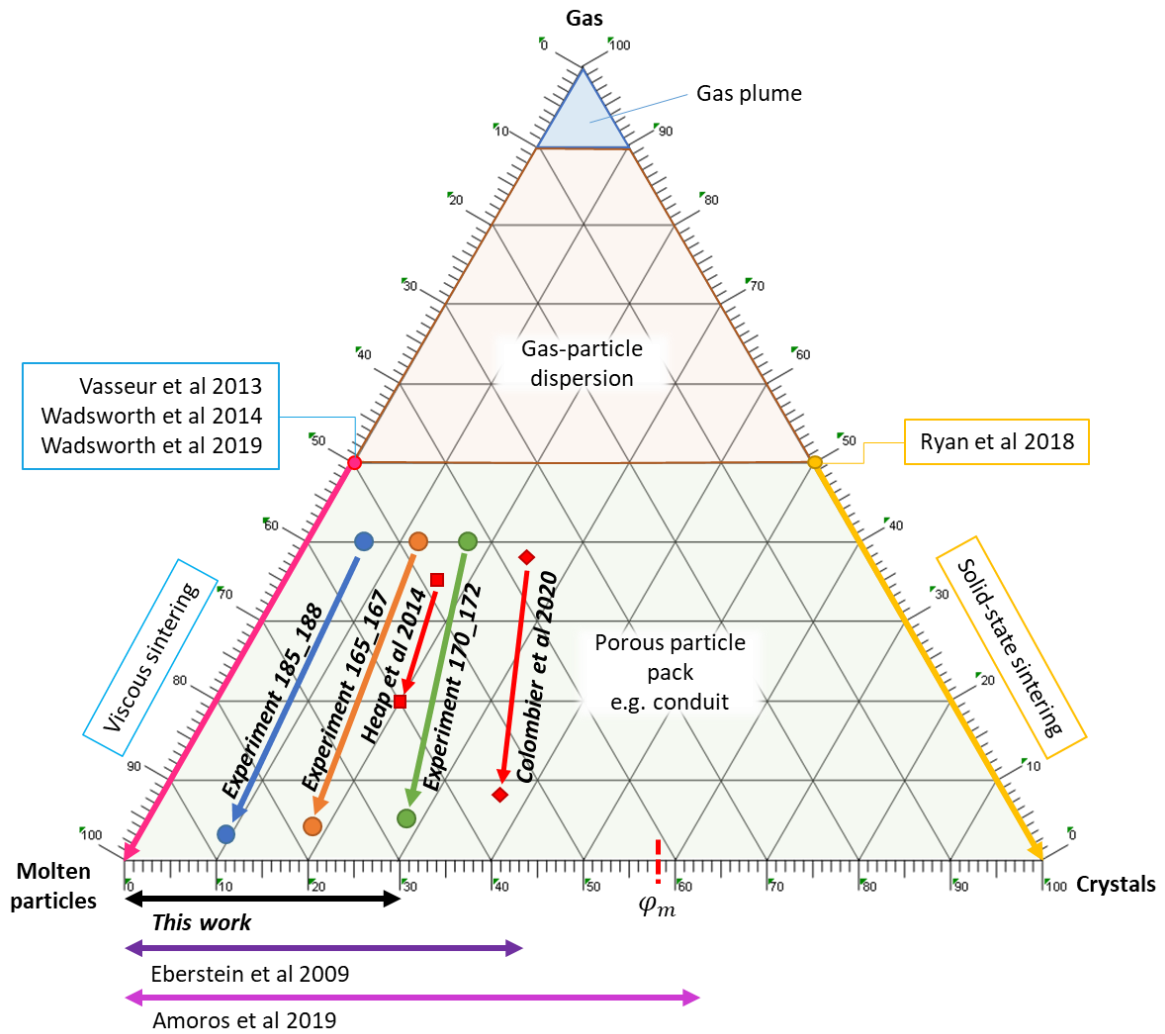


Figure 2.2: Summary of recent work on sintering. Viscous sintering is encapsulated by the pink line, solid-state sintering by the yellow line. This work (blue, orange, and green circles and respective lines) falls between viscous and solid-state sintering. Heap et al (2014; red square and line) and Colombier et al (2020; red diamond and line) are sintering experiments of one discrete crystal content. The two purple arrows represent the range of discrete crystal contents used in sintering experiments by Eberstein et al (2009) and Amoros et al (2019), two material science papers relevant to volcanology. Note: Heap et al (2014) sintering experiments were run under compacting conditions.  $\phi_m$  is the maximum packing density of spherical particles (Maron and Pierce, 1956).

## 2.6 Tuffisite veins

The experiments of this work were run under normal atmospheric conditions, with no load applied, and with temperatures held between 800-900°C on the timescale of ~30 minutes. The results would be most applicable to tuffisite veins forming in the upper tens of metres of a volcanic conduit or within a dome as this is where similar time, temperature, and pressure conditions may be found in a volcanic system. Pyroclastic flows may also produce similar

conditions; however, the generally lower temperatures of pyroclastic deposits and the faster cooling rate means sintering occurs over hours to days, much longer than the timescales of these experiments (Heap et al., 2015).

Tuffisite veins are clast-filled fractures that infiltrate the upper conduit, vent-filling deposits, and the surrounding country rock (reported to ~500m depth; Heiken et al., 1988) which may be records of processes operating in the subsurface conduit (e.g. Lavallée et al., 2012). They were first described by Cloos (1941) and are typically filled with mixtures of juvenile ash, clasts, and lithic fragments with sizes from microns up to centimetres (Tuffen and Dingwell, 2005). It is thought that fragmentation of non-Newtonian magma forms transient permeable pathways for volatiles to escape along (Gonnerman and Manga, 2003). Particles are deposited by the escaping gases and fill the fracture. The vein becomes less permeable over time as the particles (1) weld together if particles are composed mainly of fractured melt and temperature is above  $T_g$ , (e.g. Tuffen et al., 2003; Tuffen and Dingwell 2005; Figure 1.4) or (2) cemented together by precipitates from fluids flowing through the fracture network (e.g. Heiken et al., 1988). The sealing of veins is dependent on pressure, temperature, crystal content and grain size (e.g. Gardner et al., 2018).

The tuffisites may utilise both fractures that are already present (be they from fragmentation events or hydrofractures e.g. Heiken et al., 1988) or create the fracture themselves (Stasiuk et al., 1996; Kolzenburg et al., 2012). The fractures can span centimetres to hundreds of metres long but are generally only millimetres to centimetres in diameter (e.g. Tuffen and Dingwell, 2005; Castro et al., 2012; Berlo et al., 2013; Castro et al., 2014; Saubin et al., 2016). They have been described in compositions from basaltic (e.g. Cloos 1941) to andesitic (e.g. Holland et al., 2011; Kolzenburg et al., 2012; Kendrick et al., 2016) and most commonly, to rhyolitic (e.g. Heiken et al., 1988; Stasiuk et al., 1996; Gonnerman and Manga, 2003; Tuffen et al., 2003; Cabrera et al., 2011; Castro et al., 2012; Berlo et al., 2013; Castro et al., 2014).

Explosive eruptions often evolve towards more effusive behaviours as the magma is degassed. Lower than expected vesicularity in magma points to the escape of volatiles, with tuffisite veins suggested as escape pathways (e.g. Stasiuk et al., 1996; Noguchi et al., 2008). The fractures that reach the surface can allow the venting of gas and ash (e.g. Schipper et al., 2013). Kendrick et al (2016) found a network of tuffisite veins, infiltrating the Volcàn de Colima lava dome in 2011, that had reached the surface. The porosity of the veins was triple that of the host andesite (0.30-0.43 compared to 0.10-0.14) meaning permeability would be much greater through them,

and therefore, the amount of gas lost through these fractures would be much greater than the host rock. These fracture networks may then facilitate extensive degassing of the system and could shift the behaviour of events from explosive to effusive as time progresses (e.g. Stasiuk et al., 1996; Berlo et al., 2013; Schipper et al., 2013; Cabrera et al., 2015; Kendrick et al., 2016; Saubin et al., 2016; Paisley et al., 2019).

Tuffisite veins would only contribute significantly to degassing if they are pervasive, long-lived, and/or repeatedly appear. Evidence of repeated fracturing and healing has been found at multiple locations (e.g. Stasiuk et al., 1996; Tuffen et al., 2003; Rust et al., 2004; Tuffen and Dingwell, 2005; Cabrera et al., 2011; Castro et al., 2012; Schipper et al., 2013; Cabrera et al., 2015). Stasiuk et al (1996) described tuffisite veins at the Mule Creek vent in New Mexico, USA, generally following flow banding and suggested that the flow banding may be older, densely welded tuffisite veins. Tuffen et al (2003) and Rust et al (2004) both interpreted obsidian textures as evidence of repeated fracturing and healing of tuffisite veins within the conduit, at an exposed rhyolitic conduit in Iceland and Mono Craters, California respectively. Cabrera et al (2015) found evidence of healed fractures, in the Monte Pialto-Rocche Rosse eruptions in Italy, in the displacement of existing fractures along a fracture plane. Saubin et al (2016) suggested that diverse clast textures at Chaiten, Chile, indicated multiple fragmentation events, and therefore, healing of veins in between fragmentation events. Kendrick et al (2016) identified veins that crosscut one another, indicating they are present for longer than one explosive event. Additionally, the enrichment or depletion of elements can record multiple degassing events (e.g. Berlo et al., 2013; Paisley et al., 2019). Although tuffisite veins may only be open on the time scale of minutes to a day (e.g. Cabrera et al., 2011; Castro et al., 2012), or seconds to minutes under compacting conditions (Heap et al., 2019), tuffisites veins can open and close over multiple events and repeatedly provide transient gas escape routes (Saubin et al., 2016).

More efficient gas pathways may quicken the shift from explosive to effusive behaviour (e.g. Degruyter et al., 2012). The efficiency and longevity of degassing is dependent on the timescale of viscous sintering of material in the tuffisite veins, the spatial extent of veins, the number or veins, the permeability of veins, and fracture density of the conduit or dome (e.g. Castro et al., 2012; Berlo et al., 2013; Heap et al., 2015; Heap et al., 2019). Therefore, the role tuffisite veins play in degassing magma can be highly variable and depends on other properties of the individual volcano being investigated. Crystal content may also affect degassing through tuffisite veins. DeGraffenried et al (2019) suggested that crystal volumes >20 vol% reduce the

percolation threshold but Colombier et al (2020) found that percolation threshold increased with 40 vol% crystal compared to a crystal-free sample. The rate of degassing does not appear to be affected by phenocryst contents <50 vol% (Okumura et al., 2012).

Tuffisites are rarely recognised in crystal-bearing magmas (Kolzenburg et al., 2012) but this may be a case for lack of tuffisite preservation due to the explosive nature of some eruptions or evidence of the veins being erased as part of the repeated fracturing and healing cycle described by Tuffen et al (2003). With ~60 vol% crystal content, the sintering timescale at Volcàn de Colima lava dome was estimated to be a week to several weeks, although fully sealing the vein may require much longer or may not even happen without higher confining pressures (Kendrick et al., 2016). An earlier eruption in 2005 at the dome produced tuffisite-bearing blocks where veins contained  $\geq 80$  vol% crystal and lower than expected porosity and permeability results indicated that a degree of healing had been achieved (Kolzenburg et al., 2012). With very high crystal contents, healing may not occur. For example, the >90% crystal content spine at Montserrat failed to heal (Sparks et al., 2000). The presence of crystals may also encourage tuffisite vein formation. Crystal-rich magma have higher viscosities than an equivalent crystal-poor magma (e.g. Petford, 2009) which may promote fracturing and formation of tuffisite veins (e.g. Lavallée et al., 2013).

### 3. Methodology and Methods

The objective of this study is to look at the effects of rigid inclusions on sintering in silicic volcanic conduits. Crystals are almost ubiquitous in volcanic settings and can act as these rigid inclusions that prop open the pore network, slow the rate of sintering, and prolong outgassing. Yet, there is currently no research specifically investigating the effect of crystals on sintering in a volcanic regime by systematically increasing the crystal content.

To investigate the effect of crystals on a sintering mixture, I take samples of different crystal content and do *in situ* x-ray CT (computer tomography) and image processing to visualise and quantify the evolution of porosity during sintering. This is compared with current models and used to build new refined models for general behaviour of sintering with rigid inclusions. The *in situ* observations were performed using synchrotron XCT.

#### 3.1 Sample Preparation

Samples of different rigid inclusion fractions were prepared by mixing known amounts of spherical soda lime glass beads, which have been previously used as an analogue for silicic magmas (product 1922, Potters Industries, Appendix Table 1; Vasseur et al., 2015; Vasseur et al., 2016; Wadsworth, 2016; Wadsworth et al., 2017), with a sieved olivine mineral separate to produce samples of different volume crystal fraction (Table 3.1). The samples were mixed by weight % and the volume % olivine and glass calculated from the component densities (2.5g/cm<sup>3</sup> 1922 glass beads, 3.32 g/cm<sup>3</sup> olivine; Equation 3.1 and 3.2). The glass and crystals were weighed on a high precision balance and mixed by hand.

<b>Powder Mixtures</b>	<b>Units</b>	<b>1</b>	<b>2</b>	<b>3</b>
<b>Glass</b>	wt %	90	80	70
	vol %	92.28	84.16	75.60
<b>Crystal</b>	wt %	10	20	30
	vol %	7.72	15.84	24.40

Table 3.1: Mixing proportions of materials for powder mixtures.

$$\text{volume \% glass} = \frac{M_g \rho_g}{(M_g \rho_g) + (M_{xl} \rho_{xl})} \quad \text{Equation 3.1}$$

$$\text{volume \% crystal} = \frac{M_{xl} \rho_{xl}}{(M_g \rho_g) + (M_{xl} \rho_{xl})} \quad \text{Equation 3.2}$$

where  $M_g$  is the mass of glass,  $M_{xl}$  is the mass of crystal,  $\rho_g$  is the density of glass, and  $\rho_{xl}$  is the density of crystal.

The 90-180  $\mu\text{m}$  olivine size fraction was used in most experiments to give a near monodisperse particle size distribution. The olivine particles were of similar size to the glass beads (180  $\mu\text{m}$  mean diameter; Appendix Table 1). The olivine acts as a rigid inclusion and shows no interaction with the melt. Although the olivines have a greater density than the glass, they did not sink on the timescales of these experiments (see DVC, section 4.4). The aspect ratios and shape results (calculated in section 4.3) both show that the crystals are elongated in shape, generally two times longer than wide.

One experiment (Experiment 20\_860\_polydisperse) was run to examine the effect of polydispersivity and used equal masses of the <90  $\mu\text{m}$  and <250  $\mu\text{m}$  size fraction separates. The larger of these crystals are typically elongated, with the smaller size fraction of crystals more equant (section 4.3).

Each mixture was mixed with a small volume of distilled water to ensure adhesion of the particles in the sample geometry and pressed into a 3mm diameter cylinder form using 3N compression load (following the method of Wadsworth et al., 2014). The height of the samples was 3mm.

As discussed later (section 5.1.6), hand mixing did not distribute the crystals as uniformly through the sample as possible. Crystal clusters were present, particularly in the 30 wt% samples. However, areas of anisotropy can be identified and accounted for as necessary using synchrotron XCT.

### 3.2 Imaging

Quantifying the evolution of porosity during sintering requires *in situ* observation of the sintering processes and the evolving microstructure. This can only be achieved using the non-destructive *in situ* imaging capability of X-ray computed tomography (XCT).

The data presented were collected using the i12 JEEP beamline at Diamond Light Source under experiment access award EE15898-2 (prior to this project). Synchrotron XCT enables high speed data acquisition and captures the changes during sintering. Synchrotrons produce a higher X-ray flux than can be achieved in the lab, meaning higher acquisition speeds. Imaging was performed using a 53 kV monochromatic beam. The parallel beam of x-rays passes through the sample and are attenuated by the sample materials along the beam path, then hit a scintillator, converting them to visible light. Magnification of the image is then performed before the data was collected on a Vision Research Phantom MIRO™ 310 camera. 1000 projections were acquired over a 180 degree rotation for each 3D tomographic dataset, with the sample rotating continuously throughout the experiment (Drakopoulos et al., 2015).

The projection data are then reconstructed using the iterative algorithm incorporated in the standard i12 Diamond workflows. Changes in the sample morphology and internal structure can be tracked through time and the fast image acquisition rates also prevent motion blur (Dobson et al., 2016). This gives an unparalleled view into the sintering process as it evolves over time and allows the relation of the presence of crystals to the results.

A major advantage of this work over previous sintering with rigid inclusion experiments is the ability to capture changes high quality and resolution and without destruction of the sample. This overcomes limitations of differing radial and axial shrinkage and the effect that the crystals may have upon this as well as identifying areas of anisotropy that can then be disregarded or accounted for. It also overcomes the bias of using 2D data to be representative of a 3D object (e.g. van Dalen and Koster, 2012).

### 3.3 High temperature *in situ* experiment on i12

Each pressed powder cylinder was placed on a flat boron nitride ceramic sample holder, mounted on the spindle of the beam line rotation stage. Heating was performed at ~20°C/min using the Pele split furnace (Dobson et al., in review; Figure 3.1). All data were captured over the same 180 degree rotation and were of the same resolution, 7.3µm per pixel. The sample was not moved between images so that all data are perfectly aligned between scans.

An initial tomography was taken at the start of an experiment below the glass transition interval,  $T_g$  (547-552°C for the heating rate used, as established from Wadsworth et al., 2014) to determine the initial structure. Furnace heating was controlled by a k-type thermocouple built in control loop. When the target dwell temperature was almost reached, tomographies were collected at 30 second intervals using the gapped method (Dobson et al., 2016). 37 scans were collected in each gapped scan. The furnace was then switched off and the sample allowed to cool. A final image was taken, approximately 5 minutes after cooling had started (sample temperatures generally below 300°C). A typical thermal history is shown in Figure 3.2 and a summary of beam line runs and the conditions are displayed in Table 3.2.

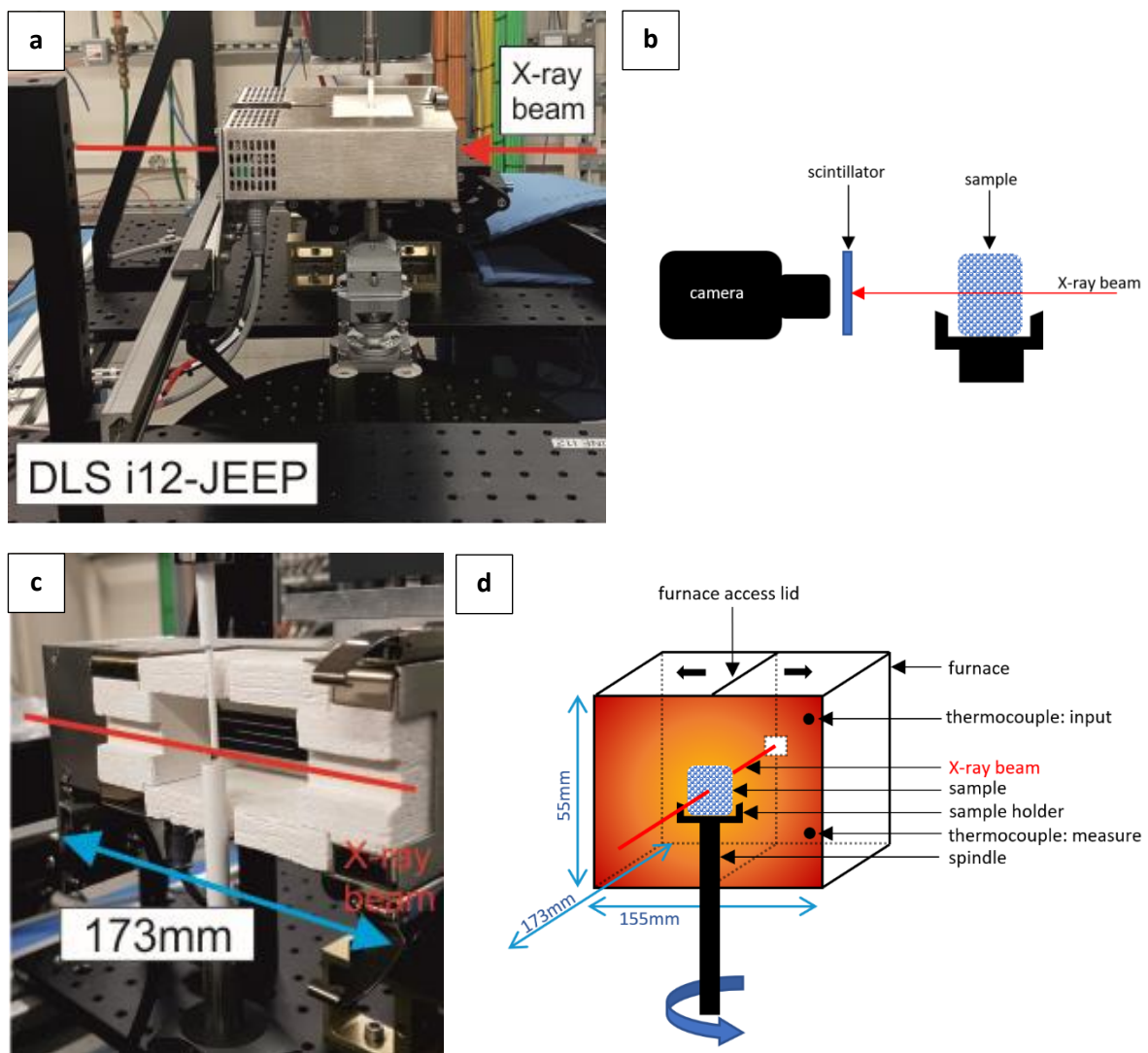


Figure 3.1: Pictures and schematic diagrams of the DLS i12 JEEP beamline set up with the furnace installation. (a) Furnace exterior. (b) Simplified diagram of equipment set up, not to scale. (c) Furnace interior in one half of the split furnace. (d) Schematic diagram of the elements within the furnace. Not to scale and viewed in a different orientation to (c).



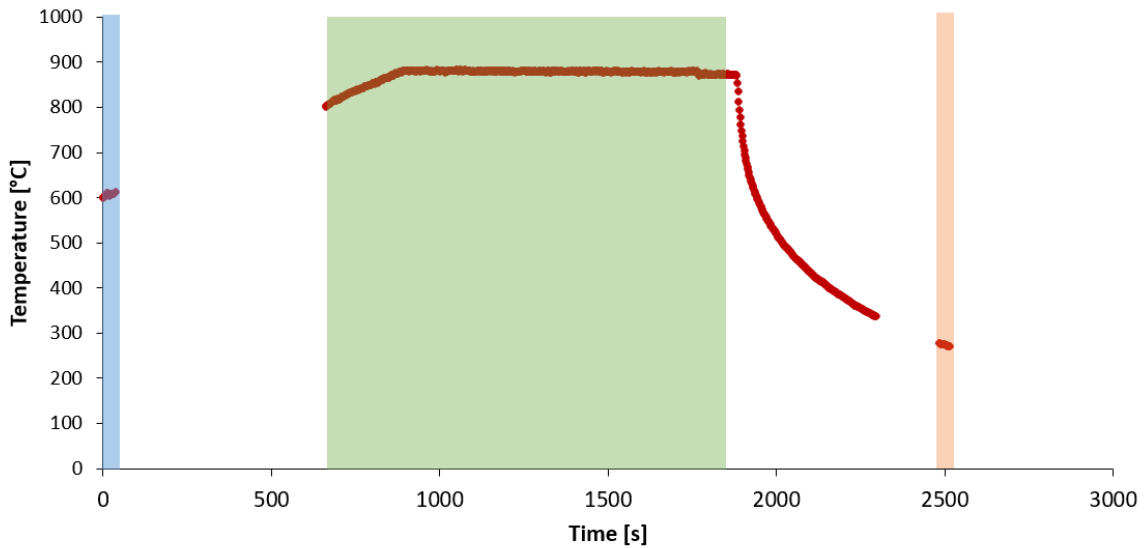


Figure 3.2: Typical thermal history for synchrotron experiments. Blue highlighted area is where the starting image is taken, green where the majority of images are taken during the main bulk of the experiment, and orange the final image.

Mixtures	Experiment	Initial temperature	Dwell temperature	Final temperature	Run time
-	-	°C	°C	°C	s
<b>1922 glass &amp; 10% 90-180 olivine</b>	10_860_longrun	535.4	860.0	857.0	7094
	10_860	566.3	860.0	855.2	2614
	10_880	600.1	880.0	277.3	2524
<b>1922 glass &amp; 20% 90-180 olivine</b>	20_880	613.9	880.0	336.3	2701
	20_860	619.5	860.0	312.3	2303
<b>1922 glass &amp; bimodal olivine</b>	20_860_polydisperse	636.9	860.0	222.1	2595
<b>1922 glass &amp; 30% 90-180 olivine</b>	30_880	623.3	880.0	331.8	2309
	30_860	676.8	860.0	857.9	2076

Table 3.2: Summary of beam line runs and conditions used. Initial temperature is the temperature when the first scan was taken. The final temperature is the temperature at the final scan.

This synchrotron XCT method introduced uncertainties. Temperature measurements are less accurate when compared to lab-based furnace experiments and thermocouples are not as accurate at higher temperatures such as those of sintering experiments. Both induce a greater degree of error for temperature. Sample temperatures are offset from control temperatures because of the heat sink of the sample. A maximum dwell input temperature of 880°C was recorded but the offset of the normalized results from the models indicated the temperature held in the furnace was not the temperature of the sample. The temperature within the furnace itself differs by as little as 10°C (Dobson, pers comms). Previous sintering work from Wadsworth et al (2019) also encountered the need for calibration and temperature correction against data where time-temperature dependence of sintering of a particular composition is known. A crystal-free sintering experiment is best for calibration, but the 10 wt% crystal experiments were used here.

The experiments fall into two groups when maximum dwell temperature is considered: the High Dwell Temperature Group (HDT Group) and Medium Dwell Temperature Group (MDT Group). The 20°C difference in dwell temperature between the HDT and MDT groups is enough to change the viscosity of the glass by an order of magnitude. The higher viscosity of the MDT Group reduces the sintering rate of the sample and does not allow complete sintering of these samples on the timescales of these experiments.

### **3.4 Post-processing**

The reconstructed 3D data were visualised and processed using the Avizo™ (version 2019.1, ThermoFisher™) software to extract the relevant results e.g. total porosity, disconnected porosity, connectivity, and the locations of crystals relative to pore space.

#### **3.4.1 Terminology**

For clarity, the following sections all use the terminology:

**Slice:** 2D plane cutting through the 3D data. Unless otherwise stated, this refers to xy orientation, a slice perpendicular to the cylinder axis.

**Stack:** A series of sequential slices.

**Module:** Pre-programmed standard algorithms within the software to perform computational operations and visualise data. These will be shown in italics e.g. *Histogram* or *Label Analysis*.

Flowcharts that describe the processing workflow modules used have been provided in the following discussion, along with any input values. Tables of the input values can also be found in the Appendix, as referred to by the figures.

### **3.4.2. Initial processing and noise reduction**

The pre-heating tomographic dataset (one single 3D image from the time series) was imported and cropped to remove the air surrounding the sample and reduce the image volume for subsequent processing using *Extract Subvolume*. The image was then processed using an edge preserving *Anisotropic Diffusion* filter to reduce image noise. The cropped and smoothed data were then segmented, or labelled, to determine if each 3D voxel volume was a glass or crystal particle, or the pore volume. Segmentation was performed using *Auto Thresholding*. This separated the image into two classes (glass and crystal, pore) based on the input range of greyscale values, derived from the image histogram. The histogram contains glass and crystal phase peaks; selecting values slightly either side identified all of the solid particles. If the input range was too low, noise was included in the segmentation mask along with particles. Vice versa, with an input range too high, not all particles were included in the mask (Figure 3.3).

To remove as much of the sample holder from the image as possible, the segmented image was cropped again using a cylindrical *Volume Edit* mask. A final manual refinement generated a custom mask for the sample that removed all of the sample holder material when used as an input for *Mask* (Figure 3.4).

Because of the gapped image acquisition protocol, the time series data are all pre-registered (aligned) and have the sample in the same orientation. All data from the experimental run can therefore be processed using the same workflow, cropping to the same image dimensions, and using the same *Volume Edit* mask and custom *Mask*. The magnitude of the changes seen meant initial processes focussed on every 6<sup>th</sup> image from the time series.

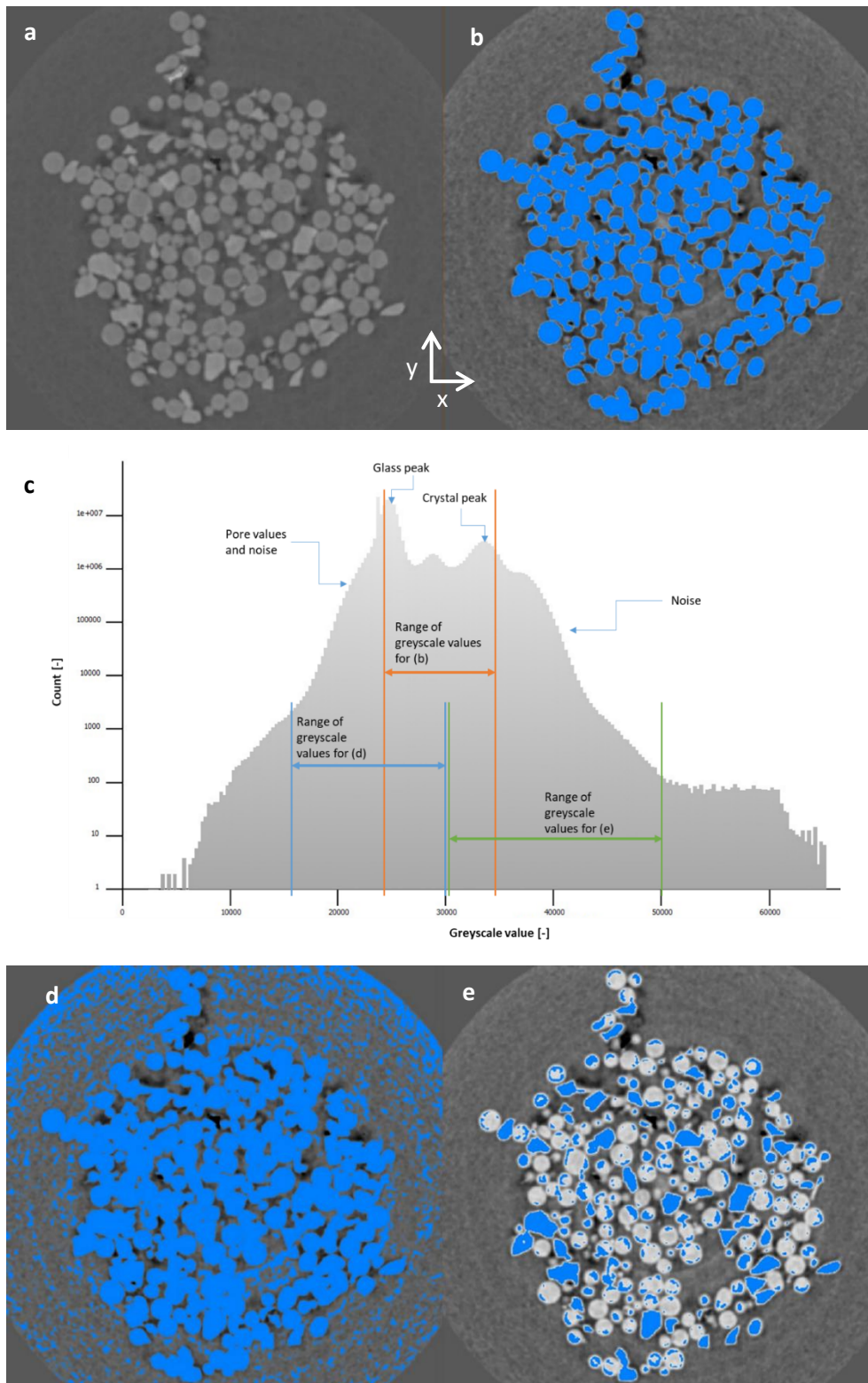


Figure 3.3: Images of the segmentation process. (a) Smoothed and cropped greyscale image, (b) segmentation mask overlying greyscale image, (c) histogram of greyscale values for voxels of (b) with input ranges for the various segmentation masks, (d) segmentation mask for too low an input range, and (e) segmentation mask for too high an input range. The sample is 3mm across.

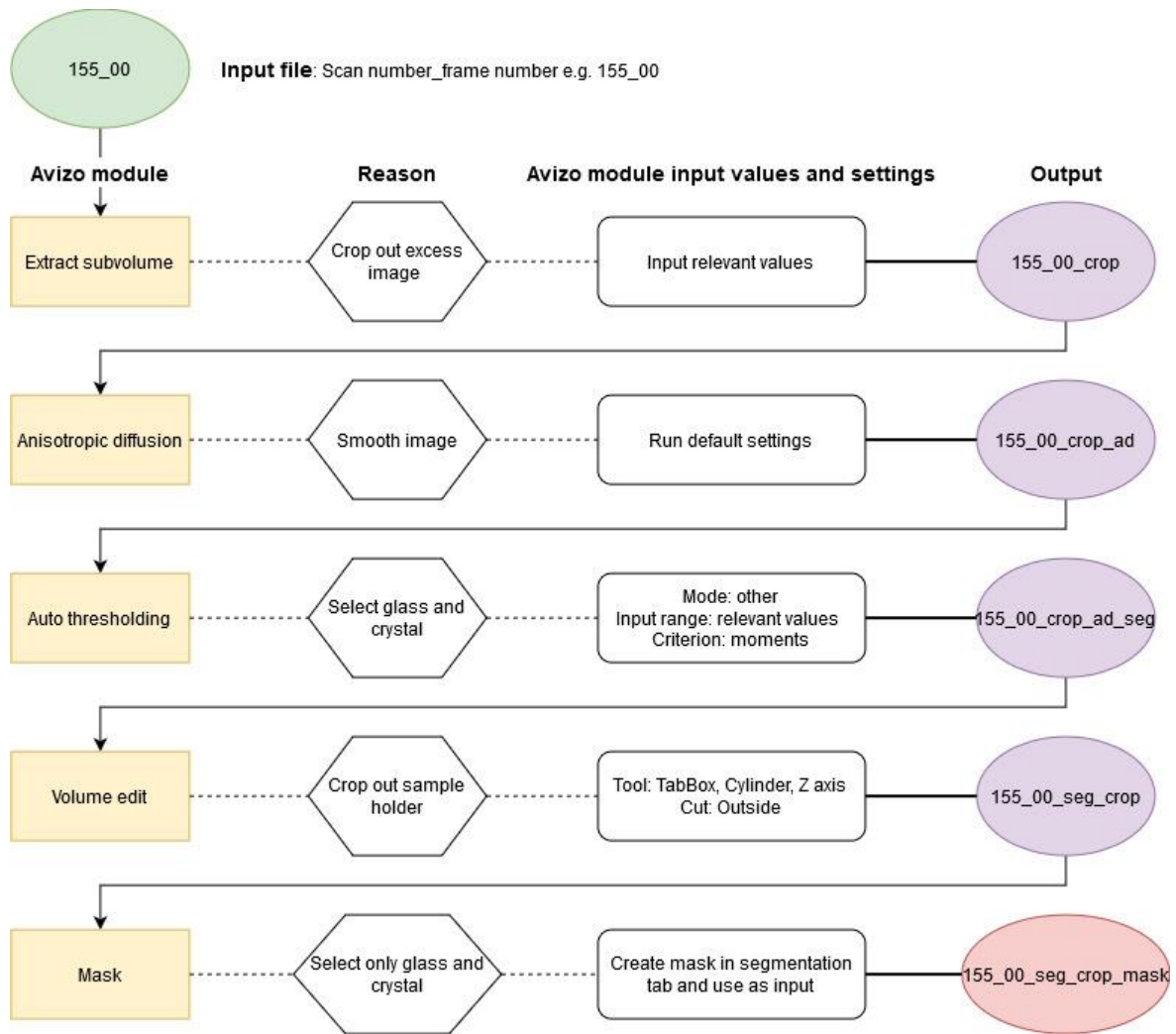


Figure 3.4: Flowchart describing initial processing of XCT data using Avizo. Green ellipse = initial imported data. Yellow rectangle = Avizo module applied. White hexagon = aim of processing step. White rectangle = module parameters, Appendix Table 2 for values used. Purple ellipse = intermediate data volume. Pink ellipse = final output data volume (saved for use in later processing steps).

### 3.4.3 Quantifying porosity

The data produced by the initial processing workflow are segmented into two classes: the solid fraction (glass and crystal), and pore. Porosity results were not obtained from the whole sample because the shape changed as the sample sintered. Smaller subvolumes were used to remove edge effects for porosity analysis and to provide a consistent area from which to obtain results across the experimental run. Two different sized subvolumes covering different areas of the sample were used to assess how representative of the whole sample the subvolumes were; both extracts should produce similar values if they are representative of the sample as whole.

A subvolume that encompassed as much of the sample as possible in the final image without including edges was extracted using *Extract Subvolume*. The same extraction values were used for all further images analysed in that particular experiment. A second smaller subvolume was also extracted (Figure 3.5; see Appendix Table 3 for the values used to extract subvolumes).

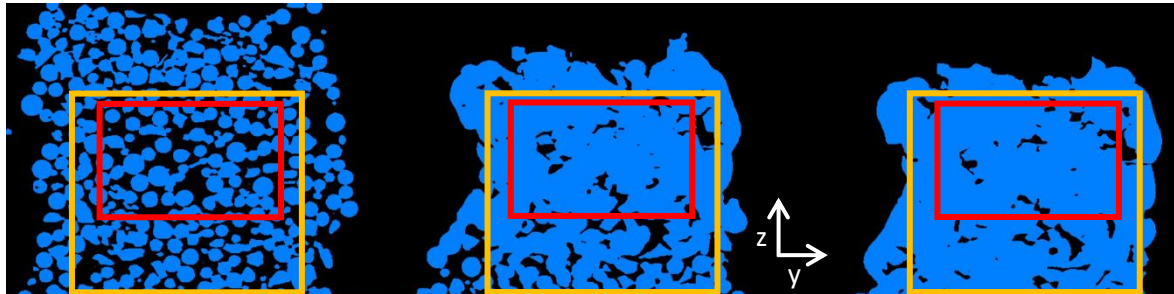


Figure 3.5: Slices in yz view of segmented data from the start, middle and end of an experiment with the solid particles in blue. The yellow box is an example area for subvolume extraction to remove edge effects and the red box an example of a smaller extraction area. The initial image is 3mm across in the y axis.

The pore volume of the cropped datum was visualised using *Invert*. Then the number of voxels assigned to each class were obtained using the *Material Statistics* module (Figure 3.6). From these values, the total porosity was calculated using Equation 3.3.

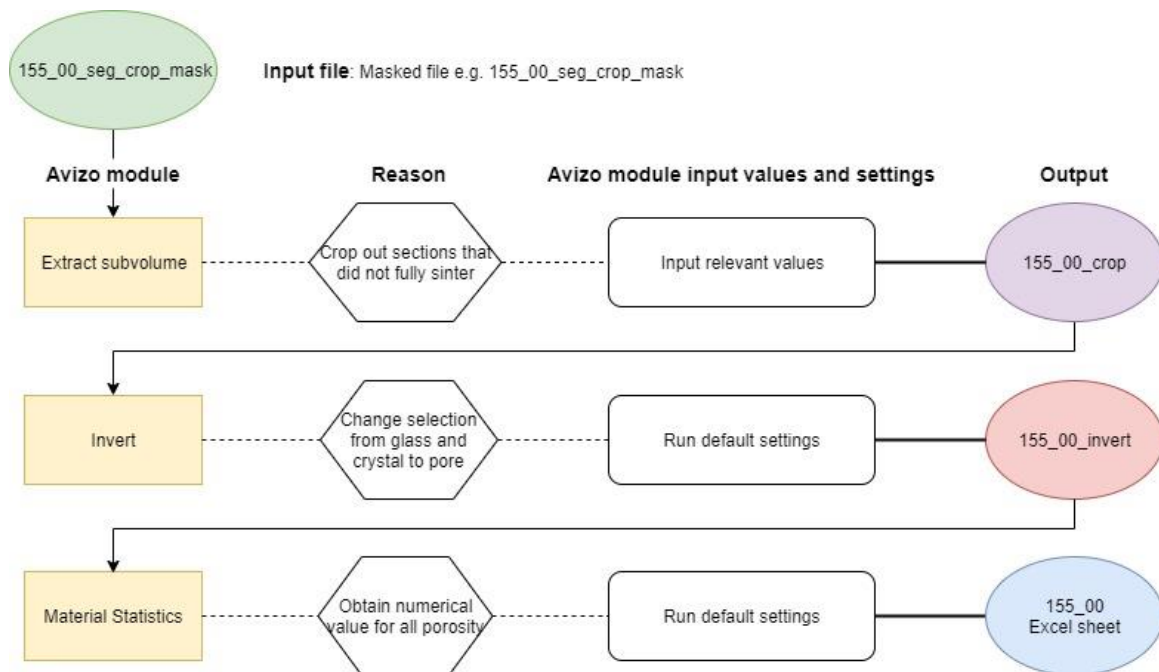


Figure 3.6: Flowchart for quantifying total porosity. Green ellipse = initial imported data. Yellow rectangle = Avizo module applied. White hexagon = aim of processing step. White rectangle = module parameters, Appendix Table 3 for values used. Purple ellipse = intermediate data volume. Pink ellipse = final output data volume (saved for use in later processing steps). Blue ellipse = final numerical data output.

$$\varphi = \frac{N_s}{N_s + N_e} \quad \text{Equation 3.3}$$

where  $\varphi$  is porosity,  $N_s$  is the number of voxels of the selected material, in this case the number of voxels the pore fraction consists of, and  $N_e$  is the number of voxels of material in the exterior, in this case the unselected solid fraction.

The connected porosity, e.g. pores that connect the top and bottom xy slice of the extracted subvolume, was identified from the inverted data using *Axis Connectivity*. Next, voxels that were in the inverted image but not in the axis connectivity image, the disconnected porosity, were retained by performing the logical operation *AND NOT Image* (visualised in blue; Figure 3.7). The number of voxels assigned to each class (disconnected pores, everything else) was computed with *Material Statistics*. Relevant values were used in Equation 3.3 to calculate disconnected porosity (Figure 3.8).

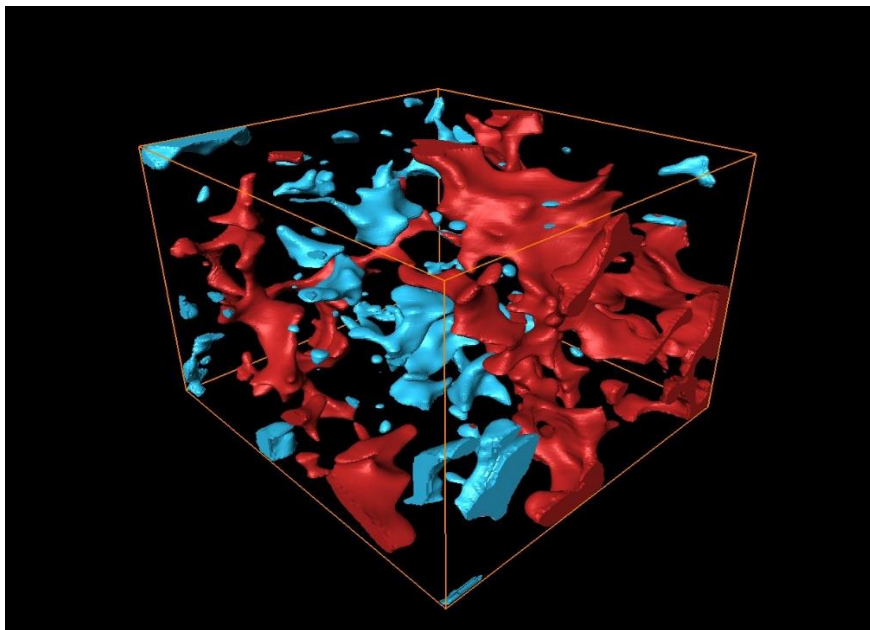


Figure 3.7: Example of pore distribution of a subvolume during the sintering process visualised using *Volume Rendering*. Red = connected through the z-axis. Blue = isolated, disconnected between two parallel faces.

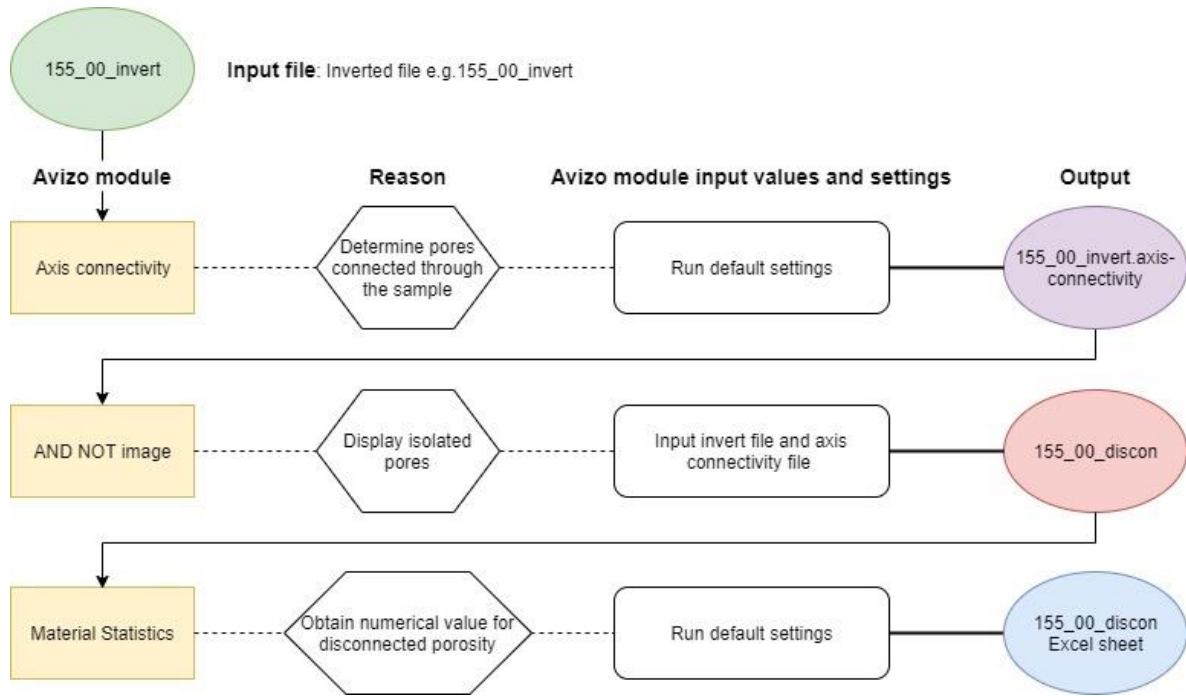


Figure 3.8: Flowchart for quantifying disconnected porosity. Green ellipse = initial imported data. Yellow rectangle = Avizo module applied. White hexagon = aim of processing step. White rectangle = module parameters, Appendix Table 3 for values used. Purple ellipse = intermediate data volume. Pink ellipse = final output data volume (saved for use in later processing steps). Blue ellipse = final numerical data output.

The use of subvolumes of data means that the values obtained for the disconnected porosity do not reflect the entire sample. However, the largest possible subvolume that stayed within the sample edges was used to ensure the disconnected porosity value is as close as possible to being representative of the whole sample. Values from a second, approximately half as small subvolume located at the centre of the unsintered sample (e.g. left image in Figure 3.5) were used to assess if the subvolumes were wholly representative of the sample.

### 3.4.3.1 Normalizing porosity

As the run conditions were not identical across all experiments and the samples were sintered under changing temperatures, the data is normalised to a common scale to account for the non-isothermal temperature-time histories. Porosity is normalized to its initial value via

$$\bar{\varphi} = \frac{\varphi}{\varphi_i} \quad \text{Equation 3.4}$$

where  $\bar{\varphi}$  is normalized porosity,  $\varphi$  is porosity, and  $\varphi_i$  is initial porosity. Time is normalized using



$$\bar{t} = \frac{\Gamma}{a_i} \int_{t_i}^t \frac{1}{\mu} dt \quad \text{Equation 3.5}$$

where  $\bar{t}$  is dimensionless time,  $\Gamma$  is surface tension,  $a_i$  is the initial pore size,  $t$  is time and  $t_i$  is the time at which welding starts, and the viscosity is  $\mu$  (Wadsworth et al., 2019). The value for surface tension is taken as  $0.3 \text{ N.m}^{-1}$  (Parikh, 1958) and although it is influenced by temperature, the variations are negligible and therefore considered a constant for this work.

A polydisperse solution for initial pore size,  $a_i$  was calculated by inputting the particle size distribution of the 1922 glass beads from Vasseur et al (2016) into the volcanic welding model resource of Vasseur and Wadsworth (2019; <https://vhub.org/resources/4568>) where the first moment gives the value  $6.69 \text{ }\mu\text{m}$ . This was multiplied by a correction factor to address the degree of monodispersivity as the equation is intended for a polydisperse population. The correction factor for this glass bead population is 65.21, which when multiplied by the first moment pore size gives an initial pore size of  $436.25 \text{ }\mu\text{m}$ .

Viscosity is calculated using the Vogel-Fulcher-Tammann (VFT) equation. The parameters valid at the range of temperatures used in these experiments for the glass particles are taken from Vasseur et al (2016).

$$\log(\mu) = \frac{-2.63 + 4303.36}{(T - 530.75)} \quad \text{Equation 3.6}$$

where  $\mu$  is glass viscosity in Pa.s and  $T$  is temperature in  $^{\circ}\text{K}$ . The presence of crystals in the mixture affects the rheology of the sintering mixture and this is accounted for by

$$\eta = \mu \left(1 - \frac{\varphi_x}{\varphi_m}\right)^{-2} \quad \text{Equation 3.7}$$

where  $\eta$  is the viscosity of glass with crystals,  $\varphi_x$  is the volume fraction of crystals, and  $\varphi_m$  is the maximum packing fraction of crystals (Maron and Pierce, 1956) which has a calculated value of 0.585 for this work from

$$\varphi_m = \frac{2}{0.321r_p + 3.02} \quad \text{Equation 3.8}$$

where  $r_p$  is the aspect ratio of the suspended crystal particles. Equation 3.5 can then be recast as

$$\bar{t} = \frac{\Gamma}{a_i} \int_{t_i}^t \frac{1}{\eta} dt \quad \text{Equation 3.9}$$

Equations 2-4 and equations 2-9 from Wadsworth et al (2017) provide the monodisperse and polydisperse models, respectively, and were compared to data from this work. As will be discussed later in Chapter 4, there is an offset present between the models and experimental data. As the models have been previously validated, the offset is likely caused by a difference between the furnace temperature and sample temperature. The sample is sat on a spindle that acts as a heat sink, directing it outside of the furnace. To correct for the temperature differential, previous high temperature *in situ* synchrotron experiments have calibrated the measured temperature in a continuous correction (Wadsworth et al., 2019) using the crystal-free experiment as the calibration tool. However, for this work, there were no crystal-free experiments run, and so the 10 wt% crystal experiments were used for calibration. A 10 vol% crystal content has a very small effect on final porosity and is similar to crystal-free experiments (Eberstein et al., 2009). To see if there was a consistent offset, the residual sum of squares (RSS) was calculated between the normalized results and the monodisperse model using the common definition

$$RSS = \sum_{i=1}^n (y_i - f(x_i))^2 \quad \text{Equation 3.10}$$

where for this work,  $y_i$  is the normalized porosity from the experiment at a given time and  $x_i$  is the model normalized porosity value at the same given time. The temperature correction that results in the lowest residual for each experiment and all 10 wt% crystal experiments combined are shown in Figure 3.9. The temperature offset is similar between all experiments, so all of the temperatures were calibrated by subtracting 106°C.

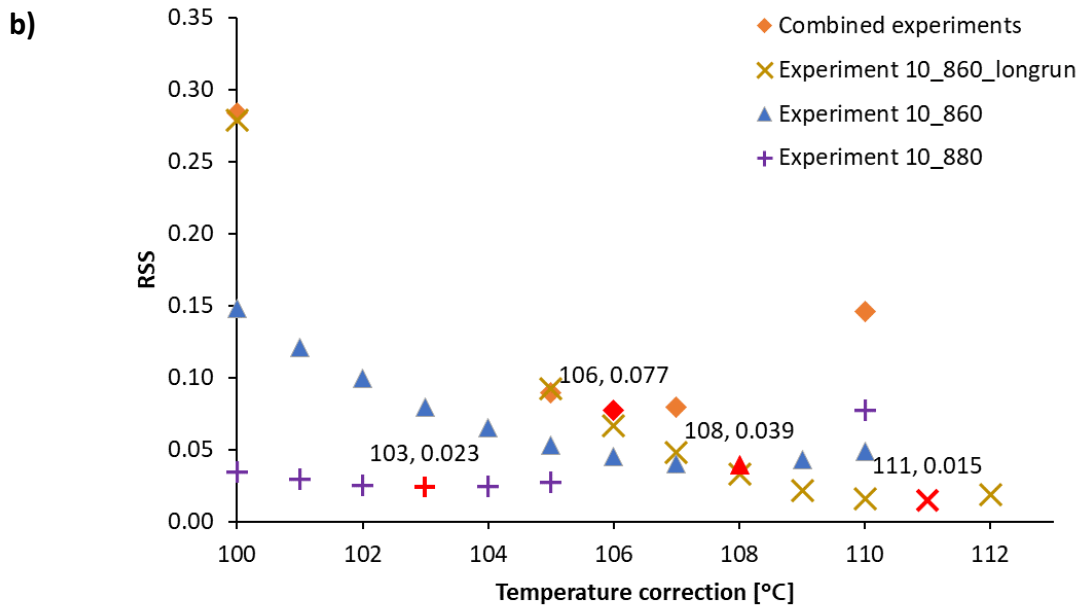
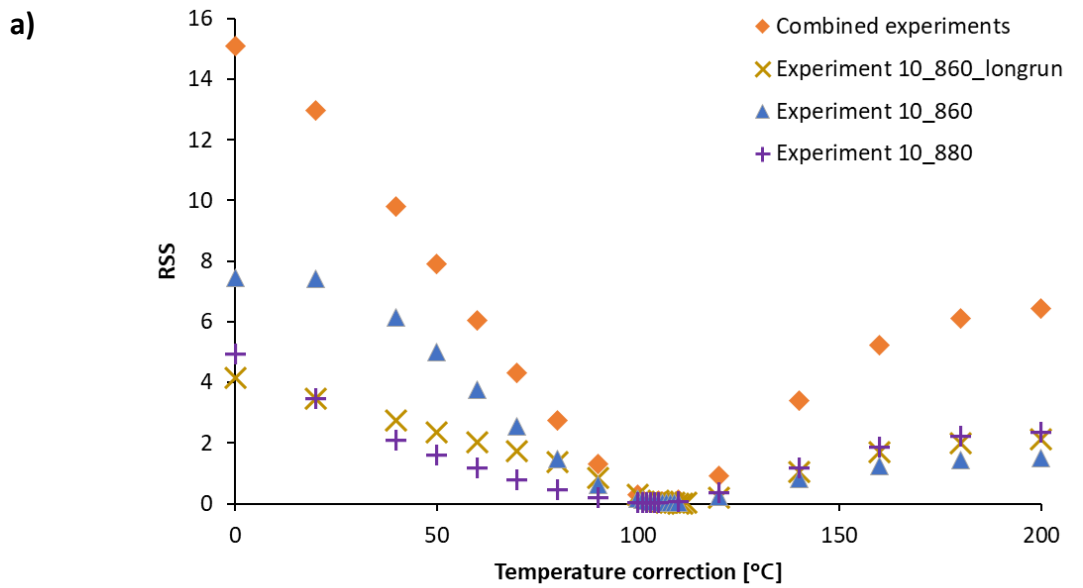


Figure 3.9: Scatter graphs showing the range of RSS values with different temperature corrections for the 10 wt% experiments and combined 10wt % experiment. (a) is a display of RSS values from 0-200°C and (b) is a closer view of the lowest RSS values between 100-112°C. Diamond = combined experiments. Cross = Experiment 10\_860\_longrun. Triangle = Experiment 10\_860. Plus = Experiment 10\_880. Red highlighted shapes in (b) are the lowest residual value and corresponding temperature for a series.

### 3.4.3.2 Connectivity

Connectivity of the pore volume fraction provides a measure of pore space that is interconnected through the sample. This is related to the permeability of a material. For these samples, a pore is considered connected if it is connected across the sample in any direction (Wadsworth et al., 2019). The values obtained from the various porosity data were used to calculate connectivity via

$$C = \frac{\varphi'}{\varphi} \quad \text{Equation 3.11}$$

where  $\varphi'$  is connected porosity and  $\varphi$  is total porosity.

### 3.4.3.3 Pore population analysis

The changes in the pore network as samples sinter were identified by computing the following measures on inverted data using *Label Analysis* (Figure 3.10).

**Equivalent diameter:** The diameter of a particle if it was spherical in shape.

**3D area:** The area of a 3D particle.

**3D volume:** The volume of a 3D particle.

**3D Shape:** The shape factor of a particle defined by

$$\text{Shape factor} = \frac{3D \text{ area}^3}{36 \cdot \pi \cdot 3D \text{ volume}^2} \quad \text{Equation 3.12}$$

where 1 is a perfect sphere and larger numbers are less spherical.

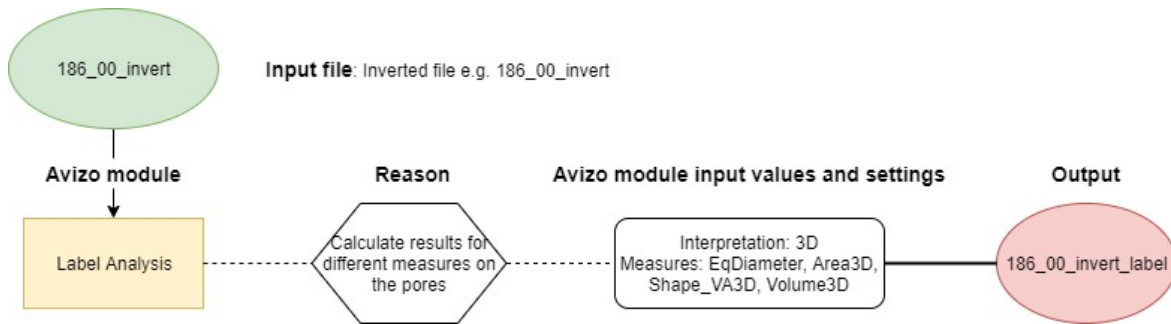


Figure 3.10: Flowchart for extracting properties of individual pores. Green ellipse = initial imported data. Yellow rectangle = Avizo module applied. White hexagon = aim of processing step. White rectangle = module parameters. Pink ellipse = final output data volume (saved for use in later processing steps).

### 3.4.4 FIJI ImageJ Weka classification

The initial processing of the synchrotron images isolates the glass and crystal phases from the pore phase. However, *Auto Thresholding* and other segmentation methods in Avizo did not work for the melt-crystal interface because the greyscale values of the two different phases overlap. The boundaries of the crystals are incorrectly classified as glass which means the whole particle is misidentified once the next processing step, *Fill*, is applied (Figure 3.11).

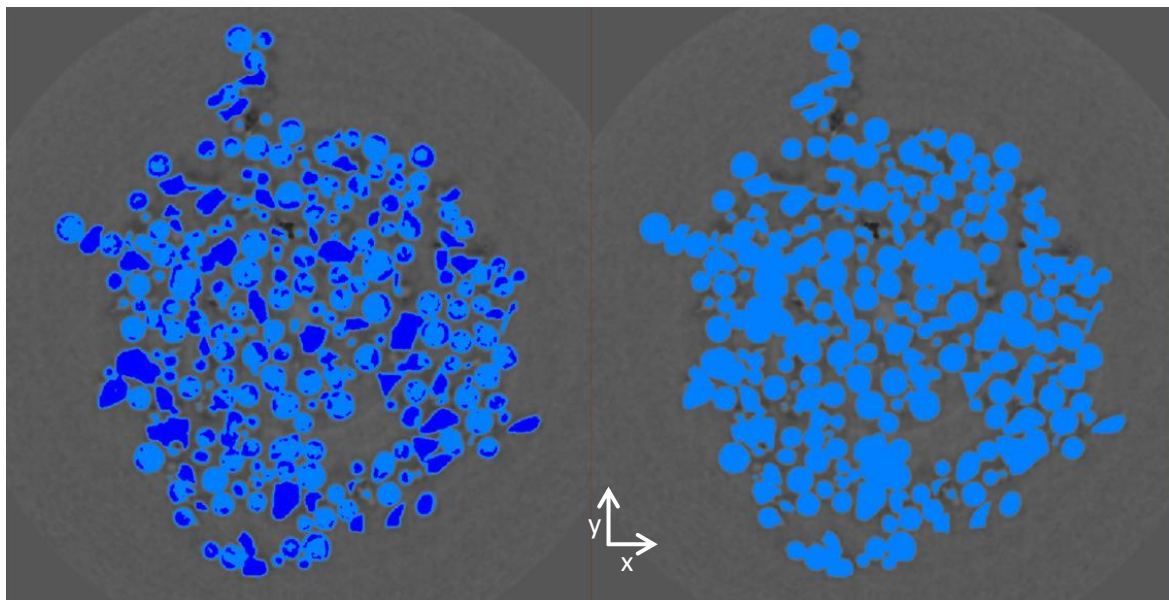
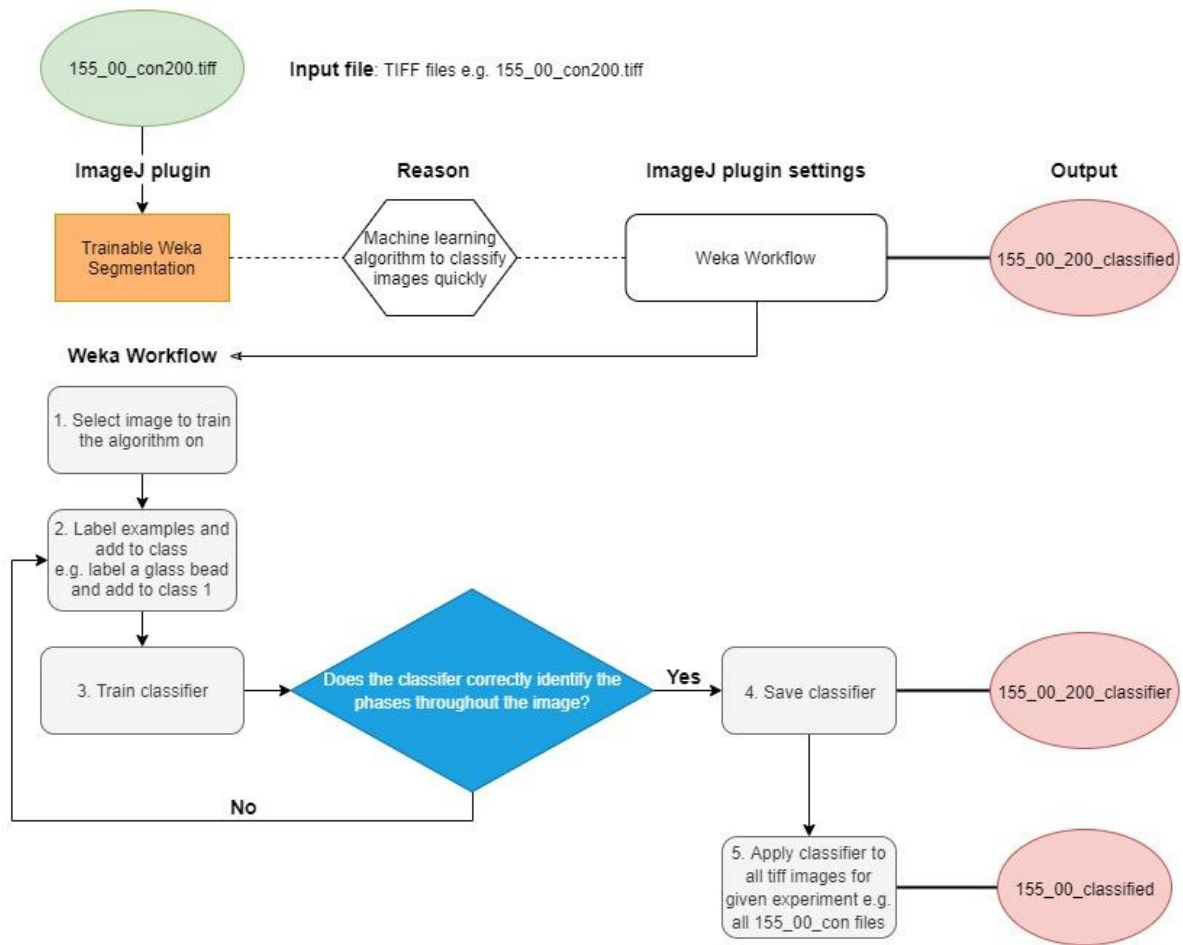


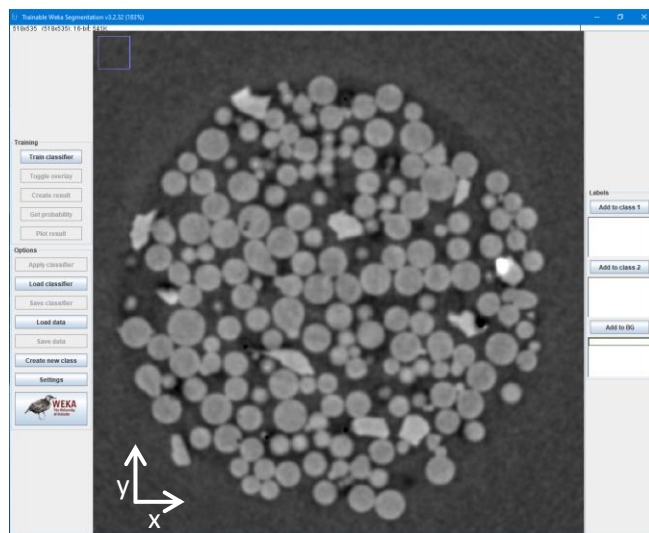
Figure 3.11: Slices in xy view of segmented data with solid particles in blue. Left: Poor identification of crystals and crystal boundaries (in dark blue) on the left. Right: Starting image for identifying crystals using Avizo. The sample is 3mm across.

To identify the glass and crystal phases, the WEKA machine learning algorithm plugin for ImageJ was applied (Trainable Weka Segmentation). A greyscale slice of the denoised data showing all three phases was imported into the plugin and examples from each phase added to each of the three label classes (pore, glass, olivine). The classifier was trained on the added examples and an overlay of the classified image appeared. If the boundaries of each particle were correctly identified, then the classifier was saved and applied to all of the image slices making up the sample. If the classification required further refinements, more examples of particles were labelled and added to respective classes until the boundaries in the classified image were correct (Figure 3.12). The best outcomes were usually achieved when the examples added to the classes were from either side of a phase boundary. The boundaries were deemed correct when they matched with what could be seen by eye. The crystals are obvious by eye because although overlapping in greyscale, they typically appear lighter in colour than the glass beads. Occasionally, crystal and glass particles were displayed as the same colour, but the crystals were then identified by their angular shape and the class of the crystal manually corrected.

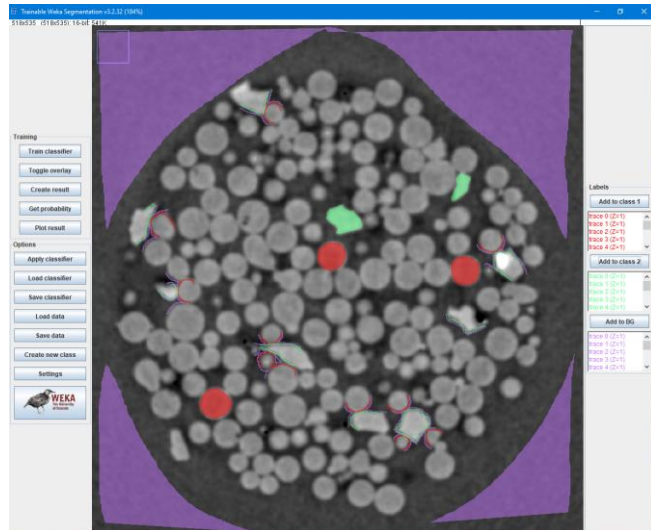
The image data for an experiment typically came from three separate scans: the starting image from the first scan, the bulk of images from the gapped scan, and the final image from the last scan. The *Auto Thresholding* input values (Appendix Table 2) and hence greyscale values differed between scans, so three classifiers were created. During the gapped scan, the *Auto Thresholding* input values sometimes shifted by 500-1000 as the properties of the glass changed during sintering. An extra classifier was created to accommodate the associated greyscale value change.



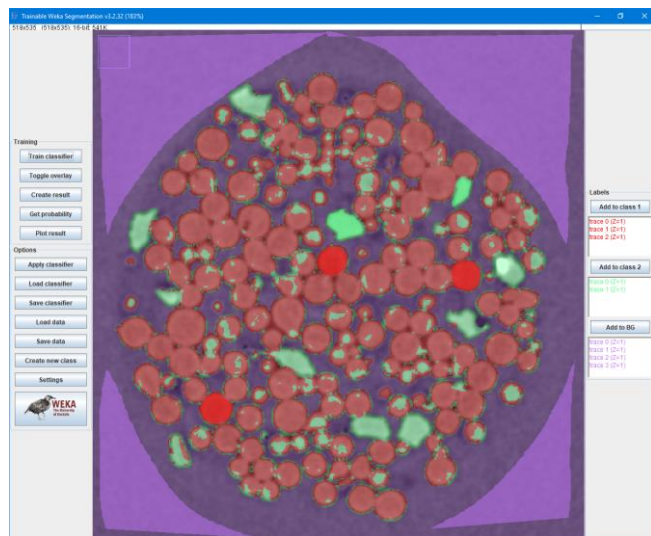
Step 1: Import a single greyscale image slice into the Trainable Weka Segmentation plugin.



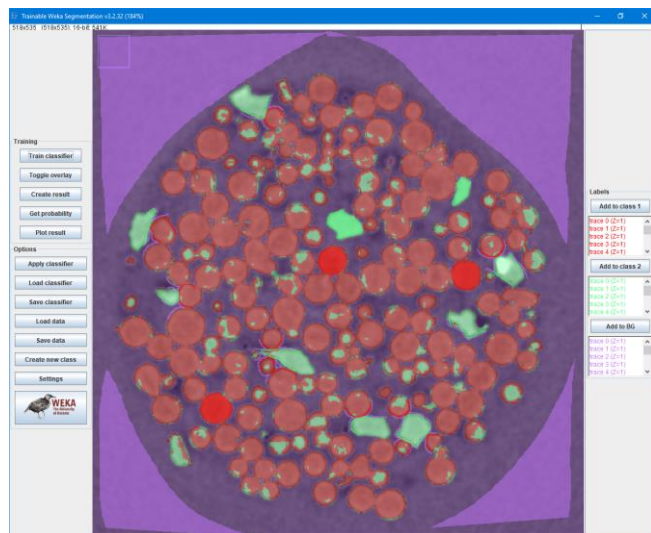
Step 2: Draw around a particle and add to the relevant class e.g. glass examples were added to class 1 and are shown in red, the crystals to class 2 in green, and pore space to class 3 in purple. Drawing borders where different phases were in contact produced better results.



Step 3: This is the classified image overlay produced by the trained classifier. The boundaries are not all correctly identified, further training required.



Step 4: Correctly identified boundaries. This classifier can be saved.





Step 5: Classified image produced by applying the classifier to the input image.

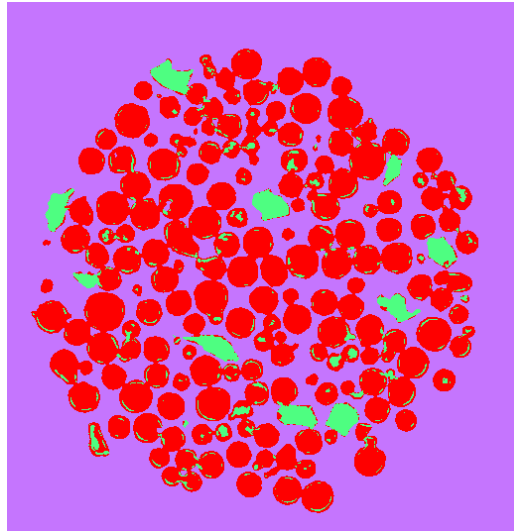


Figure 3.12: Flowchart for training a classifier and corresponding example images for the products of each step. Green ellipse = initial imported data. Orange rectangle = ImageJ plugin. White hexagon = purpose of plugin. White rectangle = plugin parameters. Pink ellipse = final output (saved for use in later steps). Grey rectangle = classifier training steps. Blue diamond = conditional statement.

### 3.4.5 Phases

The classified data were imported to Avizo and further processing undertaken in the segmentation tab to remove image artefacts (e.g. glass centres being identified as crystal due to overlapping greyscale values).

Three separate binary images were defined for each of the three phases (glass, crystal, pore) using *Threshold* to select the phase by its unique value; glass = 0, crystal = 1, pore = 2. Some pixels on olivine-glass and olivine-pore boundaries were misidentified as glass when they were actually olivine (see Figure 3.12, Step 5 image, for examples). This was easily corrected by selecting all voxels of olivine, applying a single voxel dilation followed by a single voxel erosion, and adding all remaining voxels to the olivine label field. Noise, small grains misidentified in the olivine label field, was removed using a volume threshold of 1000 voxels in *Remove Small Spots*. The average olivine crystal size was 10000 voxels so anything below 1000 voxels was noise and added to the glass label field. The final step was to correct the glass particle cores which were misidentified as olivine, the glass material was selected and *Fill All Slices* (xy orientation) was run (Figure 3.13). Note that this final step was only applied to images towards the beginning of the experiment, because as the experiment progresses, the structural changes mean olivine and pores become fully surrounded by glass.

For images towards the experiment end, the crystals are identified by eye and traced by hand in the segmentation tab from the cropped and smoothed greyscale data. The perimeter of a crystal is traced out by the user and filled using the *Fill* function. The user scrolls up a few slices and repeats the trace and fill. *Interpolate* is used to interpolate between the slices. This is repeated until the whole crystal is masked, after which it is added to a new material. The material is locked, and the user moves on to the next crystal. When all the crystals have been drawn, they are all selected and defined as a new binary image (Figure 3.14).

The difference between crystal identification by three different methods (Weka, the Phases workflow, and manual drawing) is illustrated in Figure 3.15.

Method 1: Weka. The olivines identified by Method 1 are what the image classification program classified as crystal. The number of crystals it is identifying is a magnitude larger than that of the other methods (Appendix Table 4). Higher greyscale noise and the beam hardening effect that lightens the centres of glass introduces contributes to this high number. Crystal numbers decrease between the start and end because the beam hardening effect shifts to fewer but larger patches of higher greyscale values as the attenuation properties of the glass change and the sample sinters. The effect cannot be removed by the filling process for the final image because the glass ‘ring’ encompasses the whole sample and so everything in the interior, including the crystals, would be identified as glass.

Method 2: Phases workflow. Crystals in the images have an average volume of 10000 pixels and the majority of the ‘crystals’ identified by Method 1 are noise and only a few pixels volume. Therefore, by running *Remove Small Spots* module at 1000px in Method 2, anything below 1000 pixels in volume, i.e. the noise, is eliminated. Beam hardening effects still affect the classification of end images however and they cannot be removed without removing all the actual crystals.

Method 3: Manual drawing. This is the best for accuracy because the human eye can distinguish the crystals from their lighter appearance or angular shape. However, it is a time-consuming method with the 10 wt% crystal sample (10\_880) taking a day per cropped image.

Therefore, although Method 3 is the most accurate, Method 2 is a good compromise when processing starting images as it takes far less time, is similar to what is drawn by eye, and the values are closest to Method 3. For end images, Method 3 is required to get accurate crystal numbers and shapes.

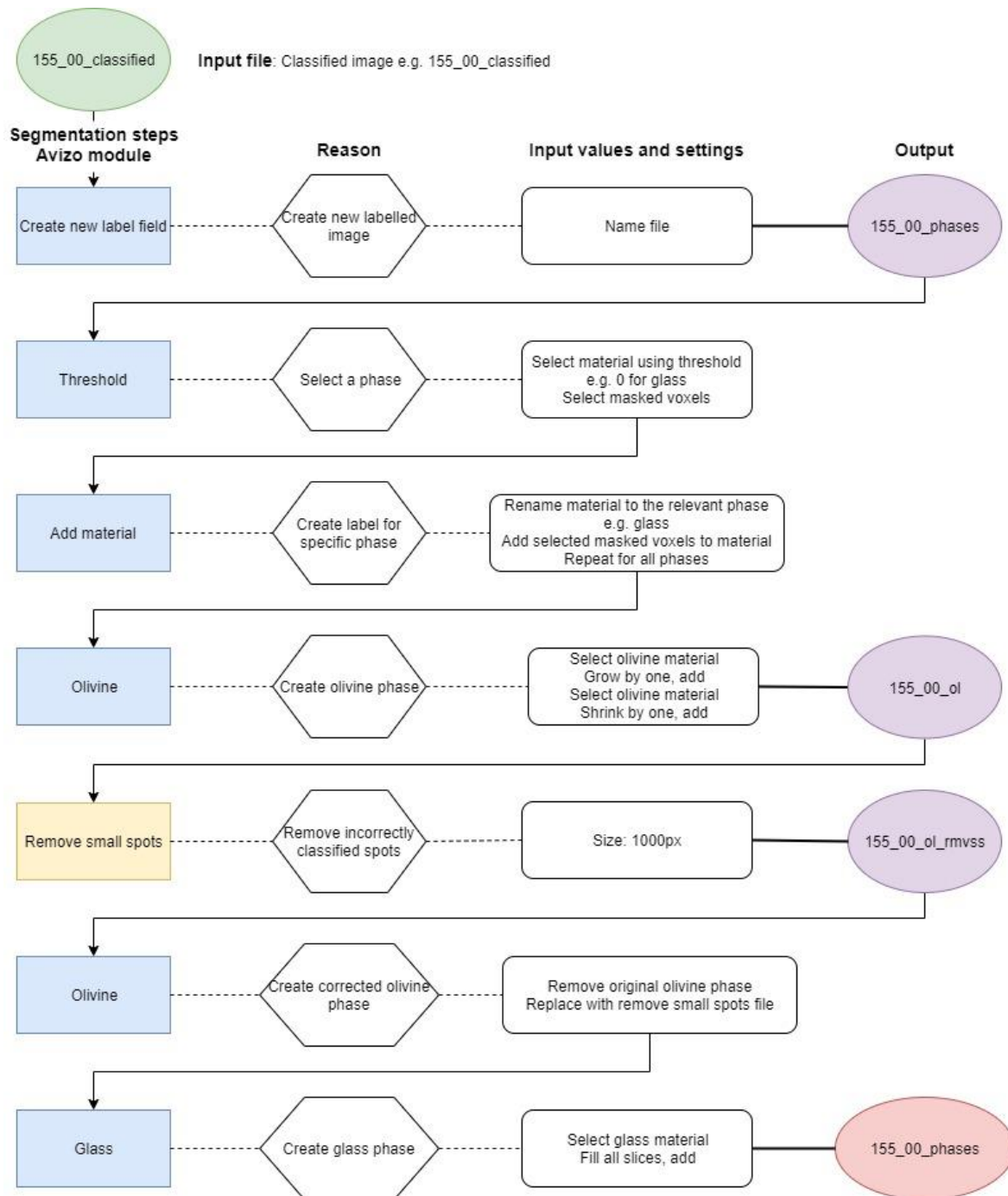


Figure 3.13: Flowchart for correcting image artefacts in classified datasets. Green ellipse = initial imported data. Blue rectangle = segmentation steps. Yellow rectangle = Avizo module applied. White hexagon = aim of segmentation step. White rectangle = module parameters. Purple ellipse = intermediate data volume. Pink ellipse = final output data volume (saved for use in later processing steps).

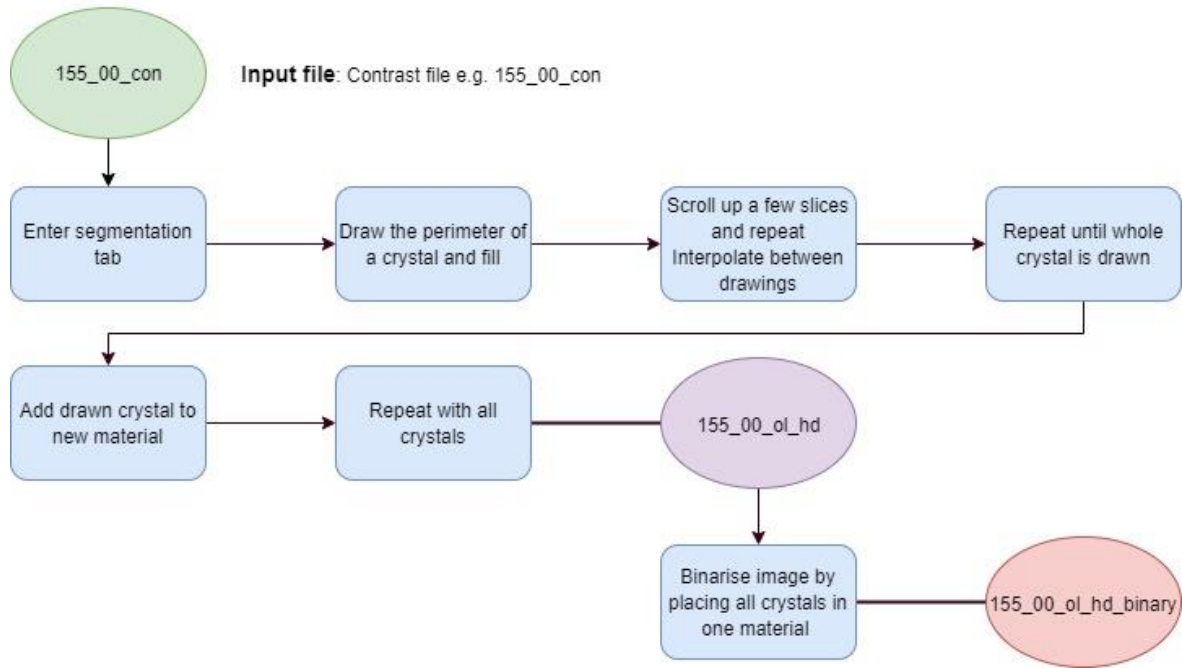


Figure 3.14: Flowchart for different methods to display crystals. Green ellipse = initial imported data. White rectangle = processing steps. Blue rectangle = processing steps in segmentation tab. Purple ellipse = intermediate data volume. Pink ellipse = final output data volume (saved for use in later processing steps).

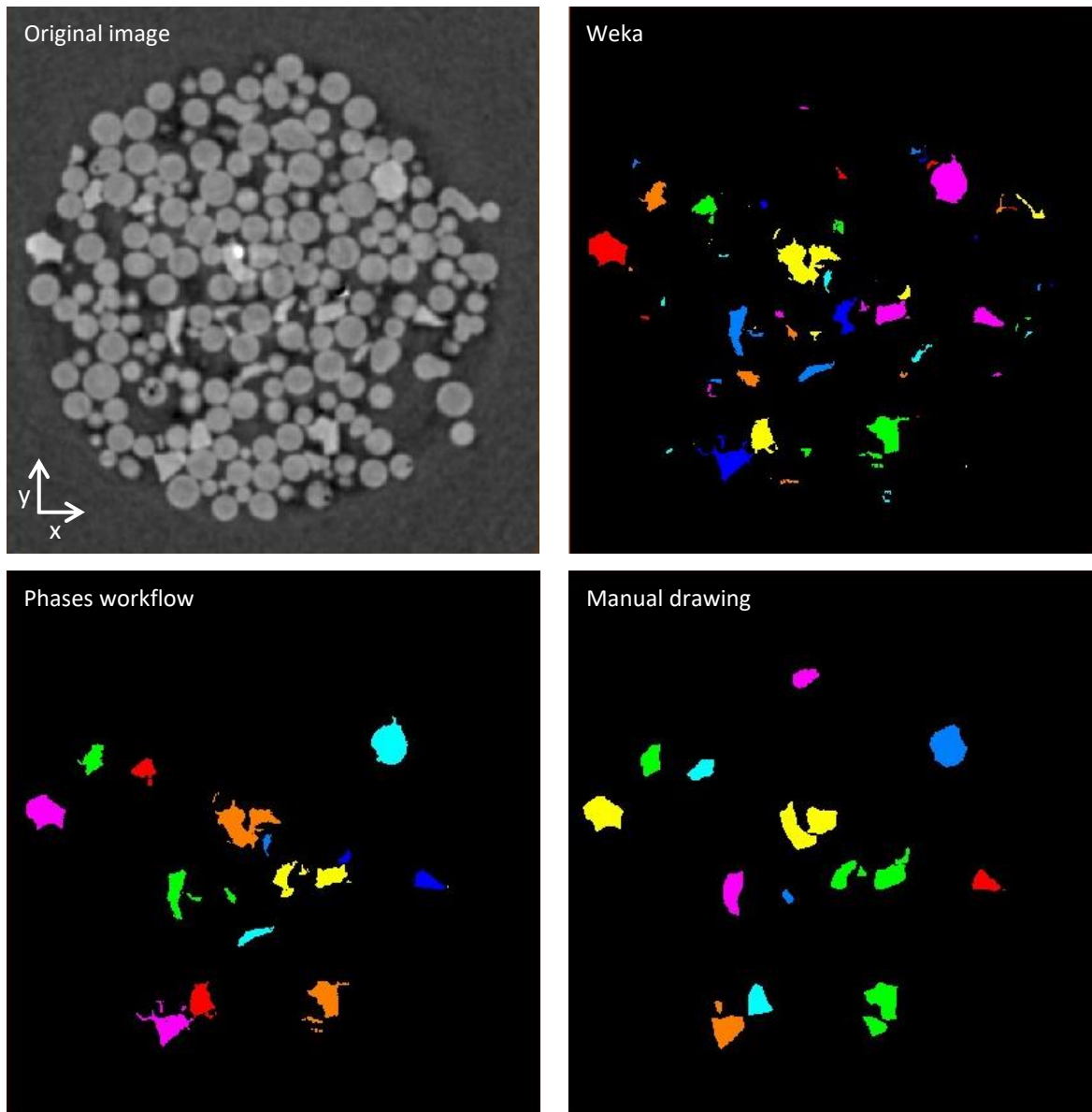


Figure 3.15: The same xy slice through a 10 wt% crystal content sample with the original greyscale in the top left and the crystals isolated by each method. The sample is 3mm across.

### 3.4.6 Calculating volume fractions

Volume fractions were used to identify sintering anisotropy and quantify the crystal content as a volume fraction, to see if there is agreement with the volume fraction calculated previously (Table 3.1). A cylindrical subvolume was extracted from the phases data to crop outside of the cylindrical sample using *Volume Edit*. Then, the number of voxels of each phase present in every slice of the cropped data was assessed with *Volume Fraction* (Figure 3.16). The values were presented in a table from which relative proportion of each phase were calculated slice by slice, or for the whole sample using Equation 3.13.

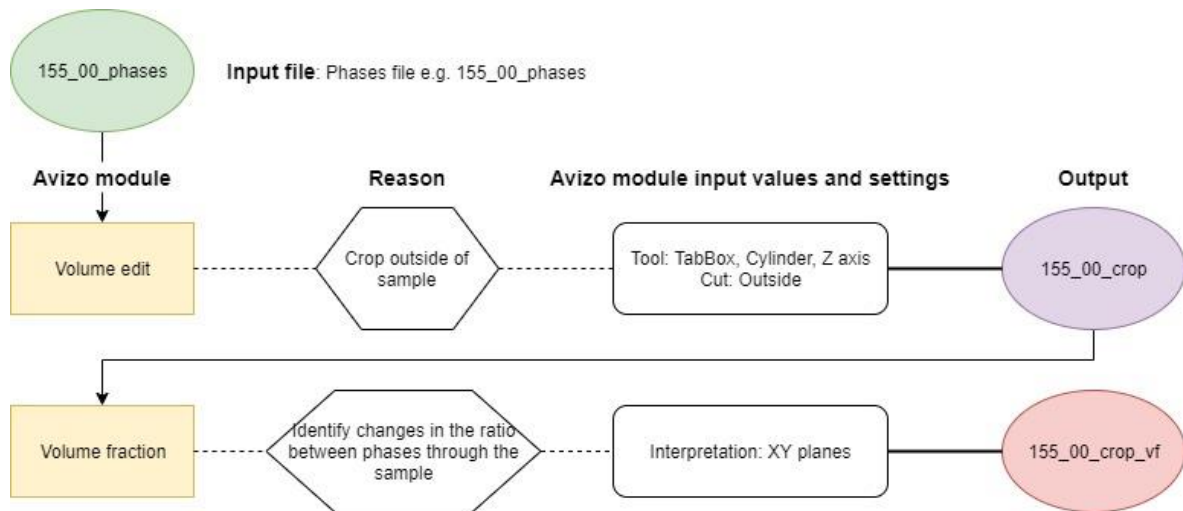


Figure 3.16: Flowchart for obtaining volume fractions. Green ellipse = initial imported data. Yellow rectangle = Avizo module applied. White hexagon = aim of processing step. White rectangle = module parameters. Purple ellipse = intermediate data volume. Pink ellipse = final output data volume (saved for use in later processing steps).

$$\varphi_x = \frac{\varphi_{xvol}}{\varphi_{pvol}} \quad \text{Equation 3.13}$$

where  $\varphi_x$  is crystal volume fraction,  $\varphi_{xvol}$  is the total crystal volume fraction and  $\varphi_{pvol}$  is the total volume fraction of all phases.

### 3.4.7 Crystal particle analysis

To compare the two populations of olivine crystals, values of different properties were computed using *Label Analysis* measures run on crystal data produced by manual drawing (Figure 3.17).

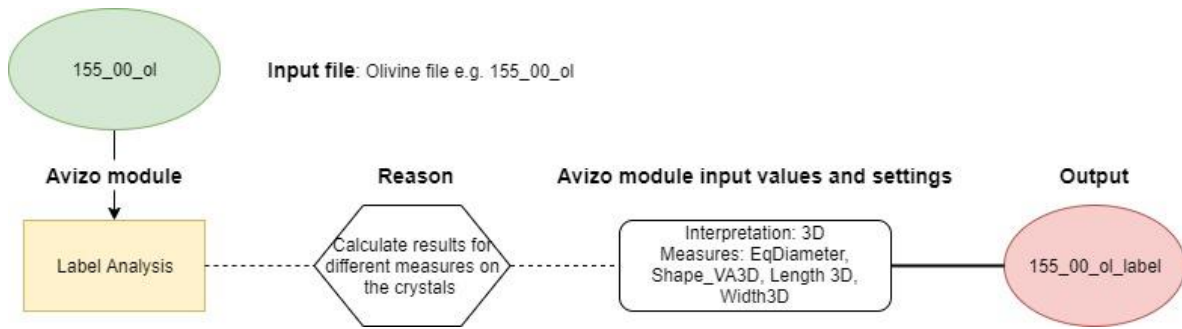


Figure 3.17: Flowchart for extracting properties of individual crystals. Green ellipse = initial imported data. Yellow rectangle = Avizo module applied. White hexagon = aim of processing step. White rectangle = module parameters. Pink ellipse = final output data volume (saved for use in later processing steps).

The measures used were:

**Equivalent diameter:** The diameter of a particle if it was spherical in shape.

**3D Shape:** The shape factor of a particle defined by Equation 3.12 where 1 is a perfect sphere and larger numbers are less spherical.

**Aspect ratio:** The ratio of the length and width calculated from label measures 3D length and 3D width

$$3D \text{ length} : 3D \text{ width} = \frac{3D \text{ length}}{3D \text{ width}} = r_p \quad \text{Equation 3.14}$$

where  $r_p$  is aspect ratio and numbers larger than 1 indicate a more elongate shape.

### 3.4.8 Crystal interfaces

To track the changes in the crystal-melt and crystal-pore contacts, dilation was used to select a 3 voxel thick shell surrounding each olivine crystal. The shell mask was created by subtracting the crystal map from the dilated crystal map using *AND NOT Image*. The area fraction of the olivine surface that was in contact with melt and pore was defined using *Arithmetic multiplications* with the shell mask (melt\*shell mask; pore\*shell mask) and measured using *Material Statistics* (Figure 3.18).

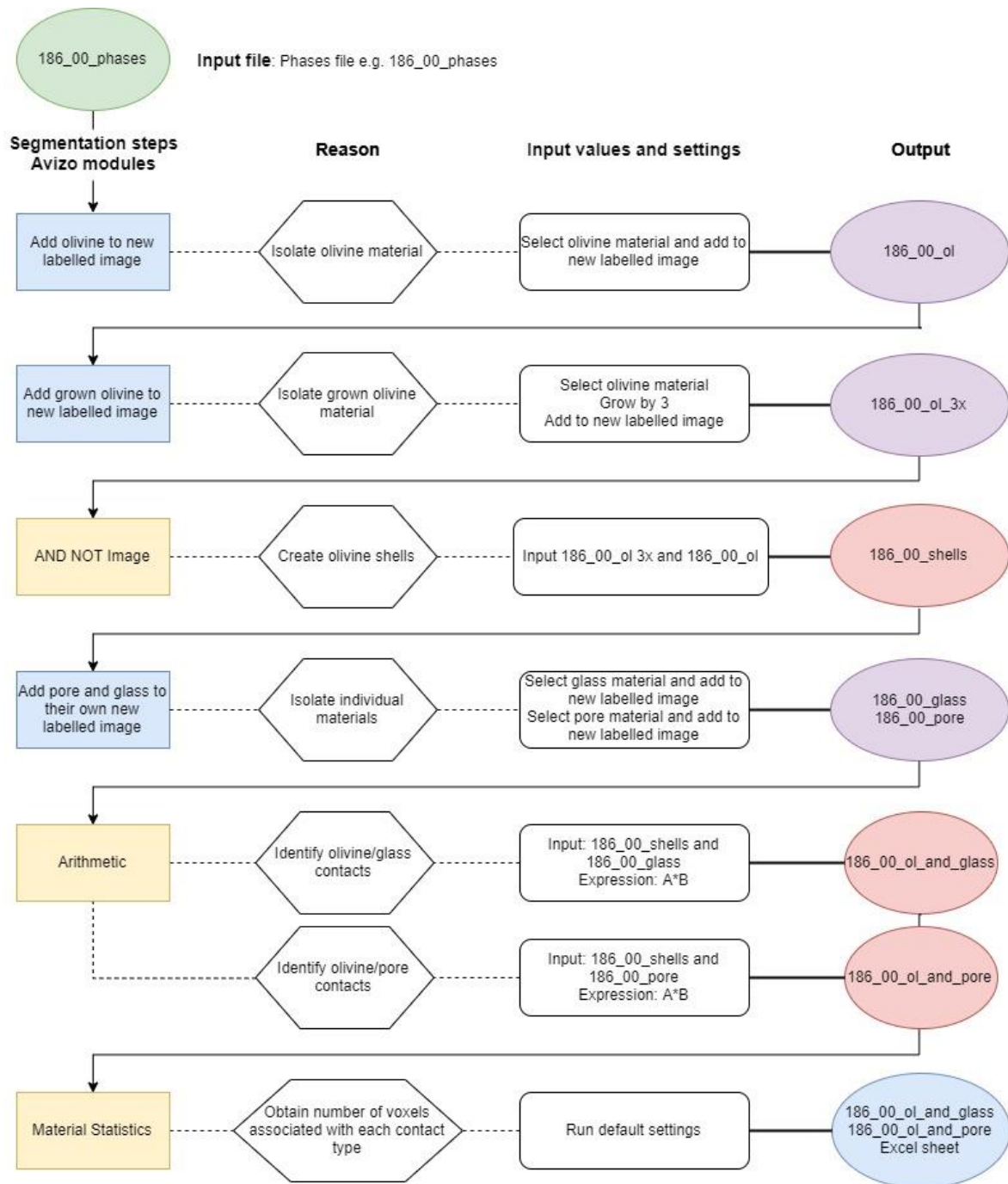


Figure 3.18: Flowchart for establishing types and amount of contacts between olivines and other materials. Green ellipse = initial imported data. Blue rectangle = segmentation steps. Yellow rectangle = Avizo module applied. White hexagon = aim of segmentation step. White rectangle = module parameters. Purple ellipse = intermediate data volume. Pink ellipse = final output data volume (saved for use in later processing steps).



### 3.4.9 Digital Volume Correlation (DVC) analysis

To visualise and quantify the magnitude and direction of deformation as the samples sintered, Digital Volume Correlation (DVC) was employed. DVC allows tracking of the image structure within a 3D mesh element during deformation.

A 3D mesh of the initial sample volume was defined using the *Volume Edit* module to generate a cylindrical subvolume that encompassed the whole sample. The built in Avizo meshing tool was then applied (fast meshing) to generate tetragonal meshes at two different mesh element sizes (Figure 3.19). The finer of the two meshes was used for all subsequent steps in the DVC as the sample undergoes sintering.

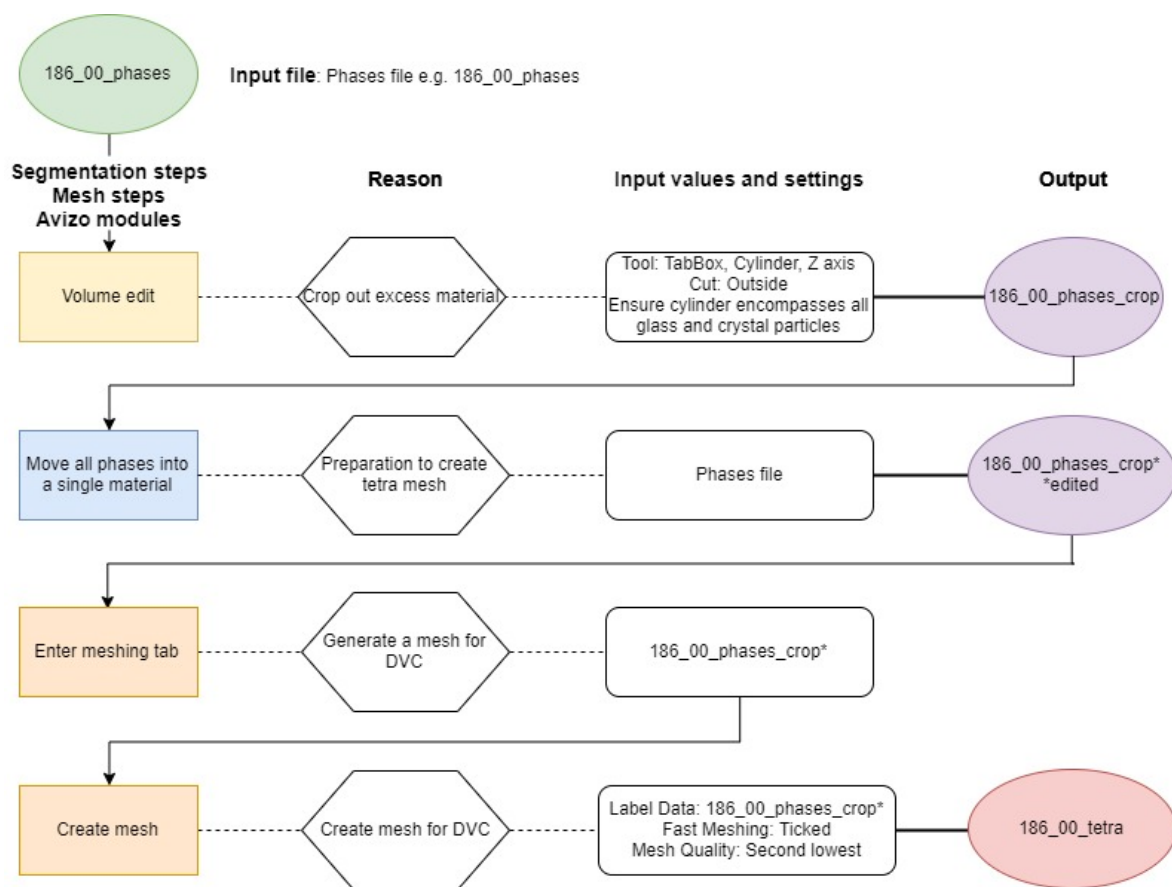


Figure 3.19: Flowchart for creating tetra mesh to be used in DVC. Green ellipse = initial imported data. Yellow rectangle = Avizo module applied. White hexagon = aim of segmentation step. White rectangle = module parameters. Purple ellipse = intermediate data volume. Blue rectangle = segmentation steps. Orange rectangle = meshing steps. Pink ellipse = final output data volume (saved for use in later processing steps).

After running the DVC module to define the motion of the coarser mesh (element size = 20), segments resulted in a displacement vector field that was too low in resolution to fully resolve

the displacements. The intermediate meshing (element size = 10) produced a clearer view of the displacements and the variation within the displacement field (Figure 3.20). A test run with a finer mesh (element size = 5) failed to produce results as the displacements are too large for the element size.

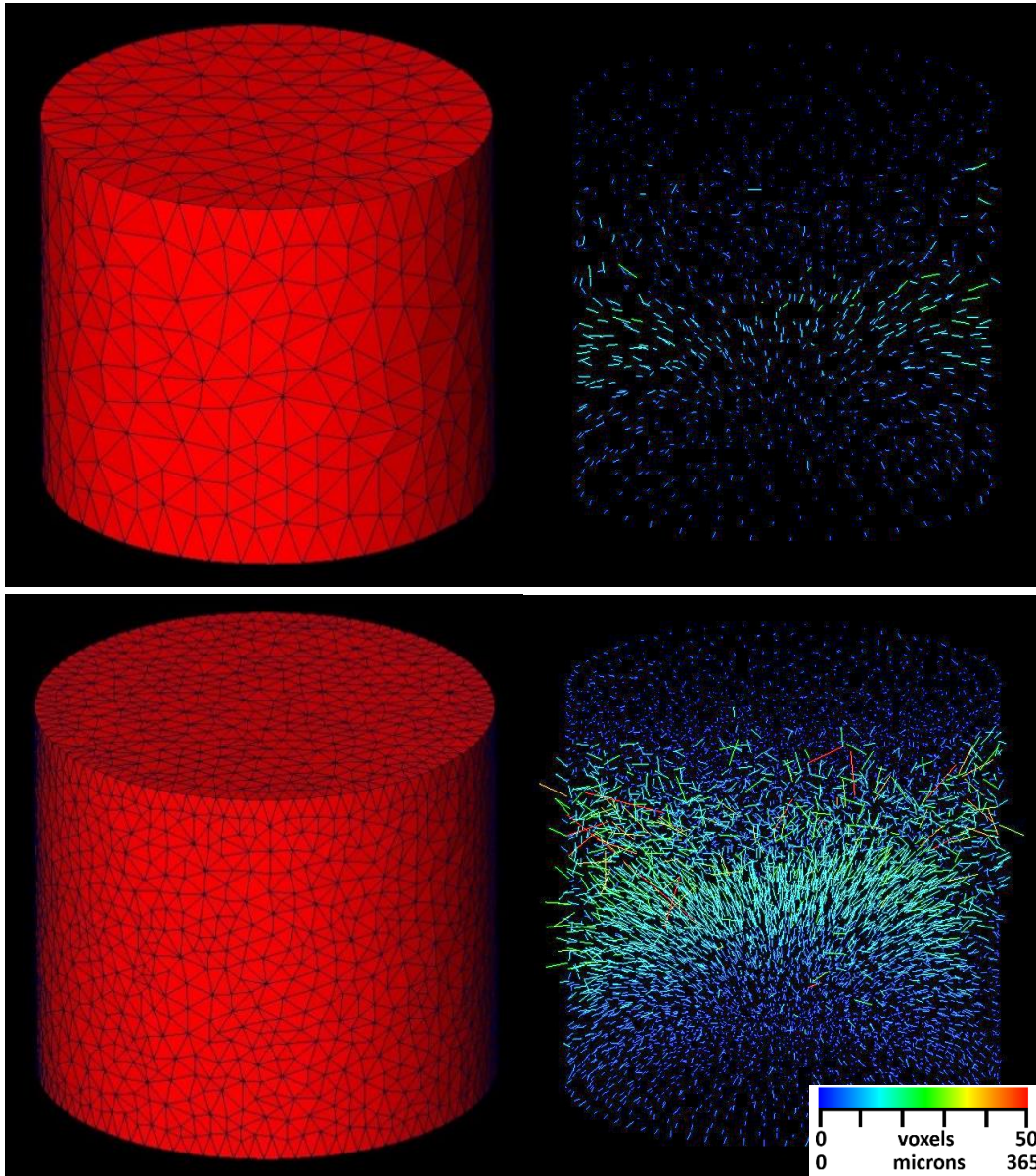


Figure 3.20: Meshes and corresponding example vector fields illustrating resolutions. Top left = coarse mesh. Top right = coarse mesh derived vector field for 186\_00 to 186\_12. Bottom left = medium mesh. Bottom right = medium mesh derived vector field for 186\_00 to 186\_12.

The *Digital Volume Correlation* module is applied to compare the initial greyscale datum with subsequent greyscale data in the sequence, with the method tracking the displacement of the image texture between mesh elements. The magnitude of the displacement, computed from the

resultant vector displacement output, can then be used to visualise the displacement vectors (*Vector Field*). In all data analyses, the same colour field and scaling has been applied (Figure 3.21).

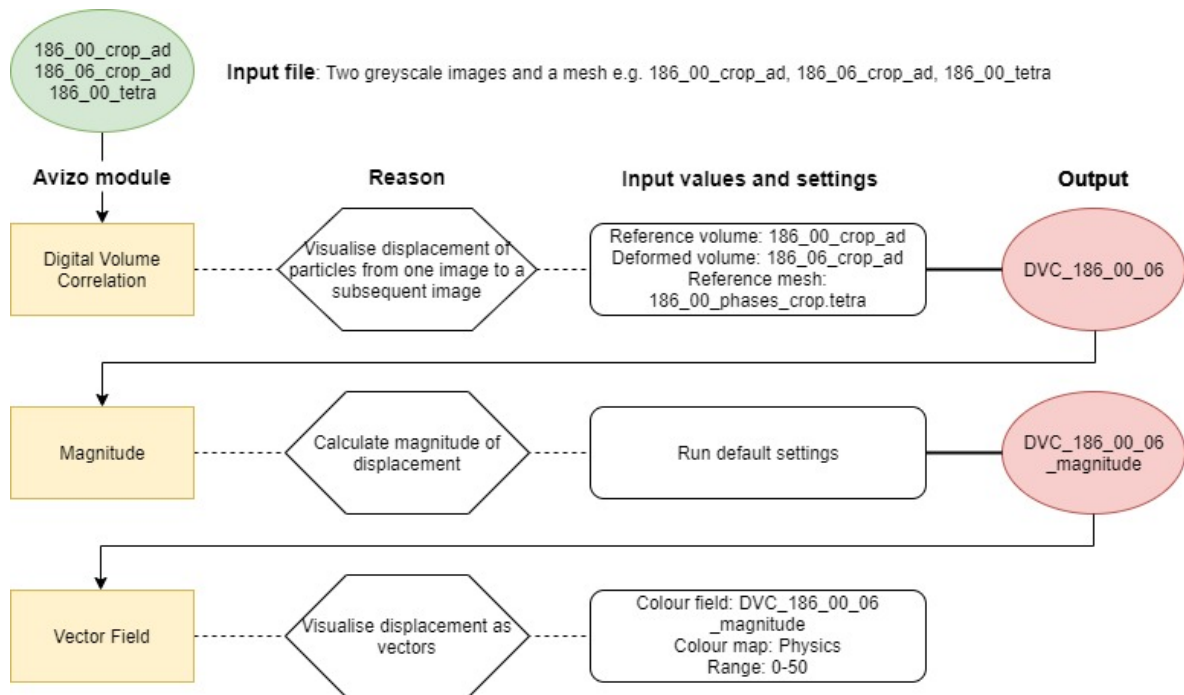


Figure 3.21: Flowchart for creating and visualising DVC analysis. Green ellipse = initial imported data. Yellow rectangle = Avizo module applied. White hexagon = aim of segmentation step. White rectangle = module parameters. Pink ellipse = final output data volume (saved for use in later processing steps).

## 4. Results

Details about experiment runs are displayed in Table 3.2, with the experiment nomenclature derived from the crystal content, maximum dwell temperature, and other defining features if necessary. For example, an experiment where the sample contained 10 wt% crystal and ran at a maximum dwell temperature of 880°C, the experiment is thus named 10\_880.

### 4.1 Quantified porosity

Porosity data is gathered from two subvolumes of different size. The large subvolume (LSV) includes as much of the sample as possible without encountering an edge and is more representative of the bulk. However, sintering anisotropy due to thermal gradients and the obscuring of mechanics pose a potential issue. The small subvolume (SSV) encompasses a region of highest sintering to check agreement between values from the large subvolume. The dimensions of both subvolumes for each experiment are listed in Appendix Table 3.

The data considers connections through all three axes whilst all renders display porosity connections through the z-axis only for illustrative purposes.

#### 4.1.1 Total and disconnected porosities

The 10 wt% experiment (10\_880) sintered at the highest temperatures (Table 3.2). The total porosity decreases, and the disconnected porosity increases over the course of the experiment as the dwell temperature is reached and held (Figure 4.1). The same trend is seen in both subvolumes. The LSV porosity network is fully connected through the z-axis initially, with a few isolated pores first appearing in the top half of the sample at  $t=1023$ . As the experiment progresses, more pores become disconnected until there are no longer any pores connected through the z-axis which occurs at an unknown point between 1743 and 2485 seconds (Figure 4.2)

While the initial total porosity of the two subvolumes is 0.442 and 0.435 (only 0.007 different), over the course of the experiment the values diverge, with the decrease in porosity faster and greater in the smaller subvolume. Likewise, the disconnected porosities agree for the first 1000 seconds. In the smaller subvolume, the disconnected porosity converges to the total porosity (i.e. no pores connect through the sample in any direction of the smaller subvolume). In the

larger subvolume, ~53% of the porosity remains connected through the x- and y-axes at experiment end.

The data suggest the smaller subvolume within the highly sintered region has reached a final equilibrium porosity. The larger subvolume includes a greater fraction of the sample, and the final porosity equilibrium has not yet been reached. There are some variations of values between subvolumes, but they are within standard error and relatively minor especially considering the crystal content of each subvolume is likely different.

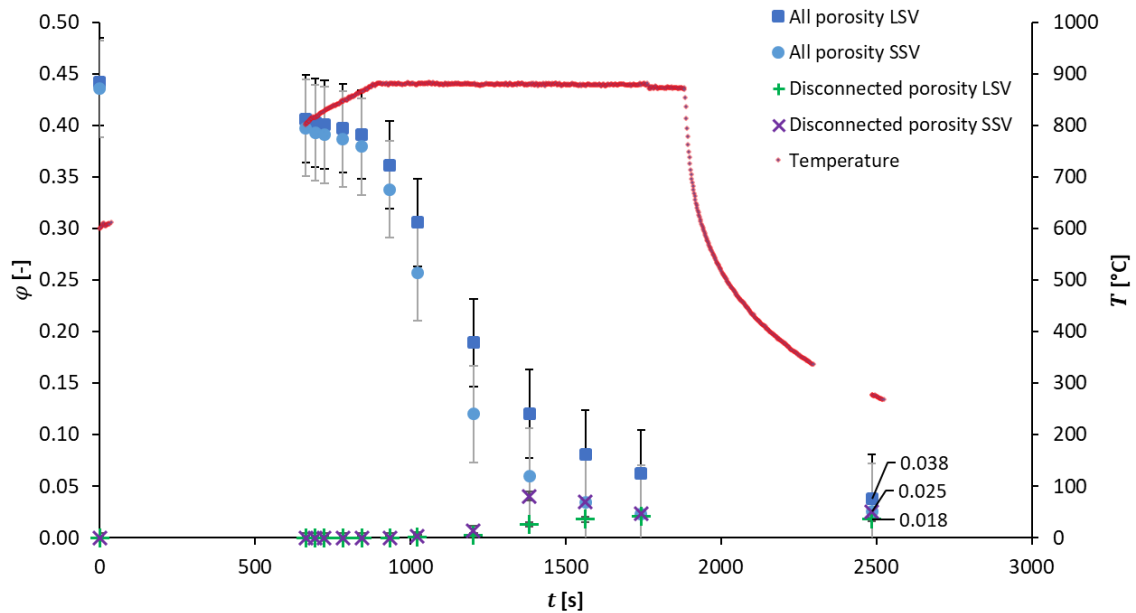


Figure 4.1: Evolution of overall and disconnected porosity (all axes) from a large and small subvolume for Experiment 10\_880, showing reduction in overall porosity and increase in disconnected porosity as the experiment progresses. Markers and standard error: Square = all porosity LSV ( $\pm 0.043$ ). Circle = all porosity SSV ( $\pm 0.047$ ). Plus = disconnected porosity LSV ( $\pm 0.002$ ; smaller than marker size). Cross = disconnected porosity SSV ( $\pm 0.002$ ; smaller than marker size). Red point = furnace temperature.

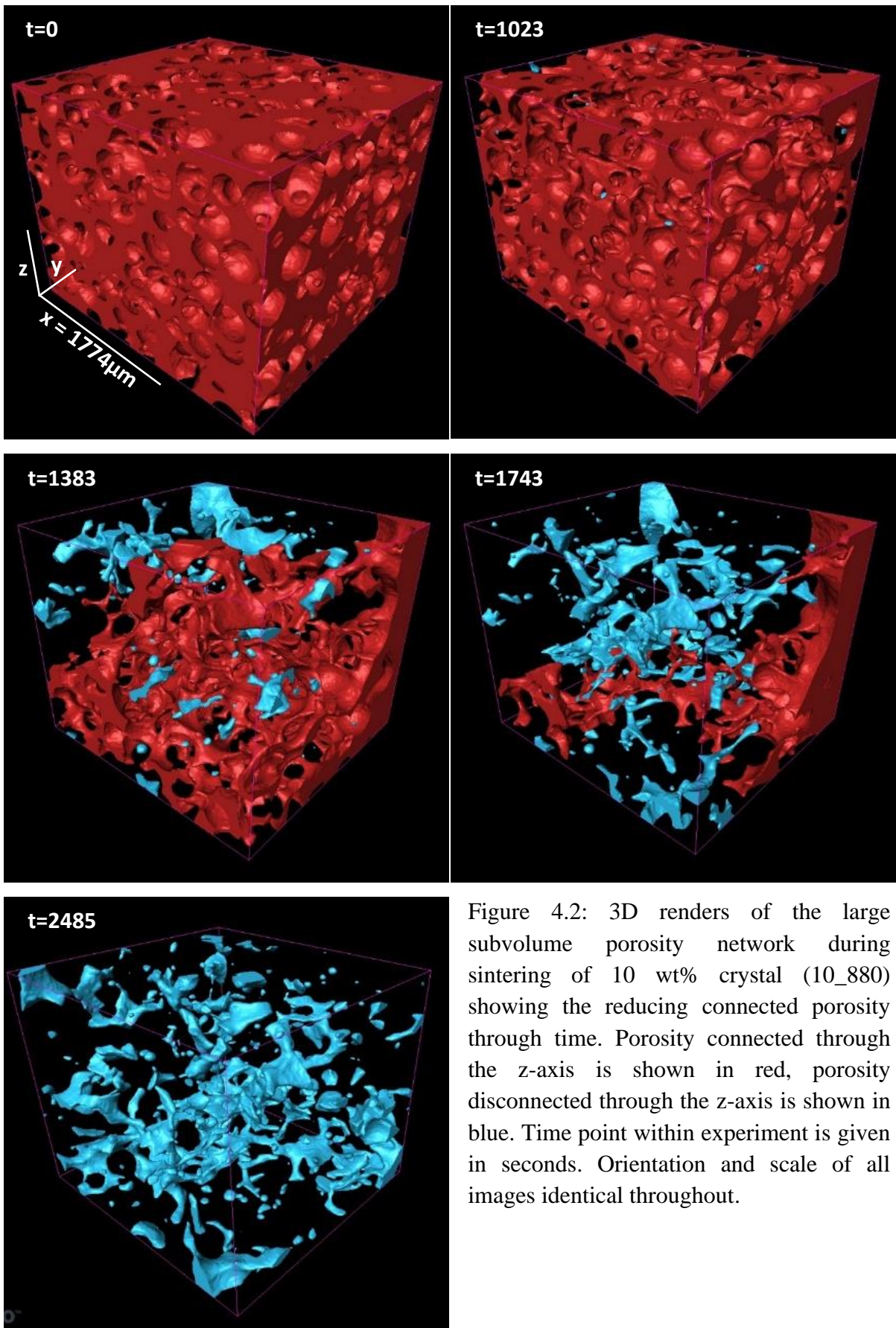


Figure 4.2: 3D renders of the large subvolume porosity network during sintering of 10 wt% crystal (10\_880) showing the reducing connected porosity through time. Porosity connected through the z-axis is shown in red, porosity disconnected through the z-axis is shown in blue. Time point within experiment is given in seconds. Orientation and scale of all images identical throughout.

A second experiment with 10 wt% crystal (10\_860\_longrun) was run with multiple dwell temperatures (Figure 4.3). Again, the total porosity for both subvolumes decrease, but only once the third dwell temperature is reached. The disconnected porosity increases from the same initial value. The LSV porosity network is fully connected through the z-axis, with most disconnected pores appearing in the top half of the sample as the experiment progresses. There is still connected porosity through all three axes at the end of the experiment (Figure 4.4)

The initial total porosities of the LSV and SSV are very similar, 0.401 and 0.412 respectively. The porosity decreases faster and greater in the smaller subvolume which results in a divergence of values between the two subvolumes. Similarly, the disconnected porosities agree until a divergence in values at ~5400 seconds. In both subvolumes, the overall and disconnected porosity do not converge meaning ~88% of the pores are connected through any given axes at the end of the experiment in the LSV, and ~32% in the SSV.

The data suggest that neither subvolume has reached a final equilibrium porosity and that sintering is incomplete. The smaller subvolume has a lower final porosity and so, as before, sintering has progressed further in this volume. The reduction in porosity occurs more slowly than in the previous experiment, the first two dwell temperatures were too low for sintering.

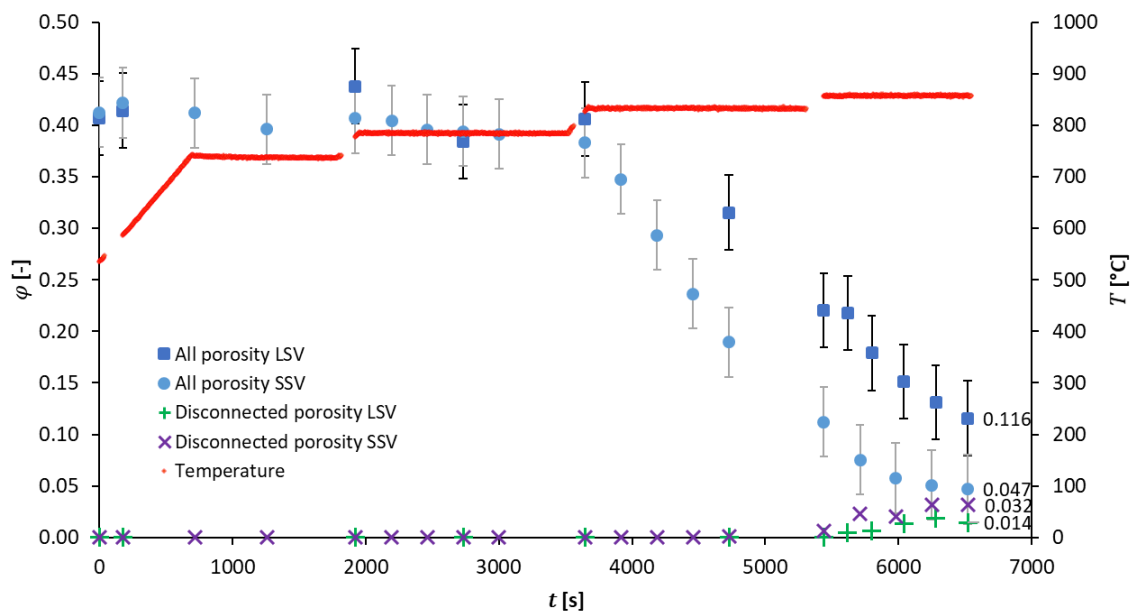
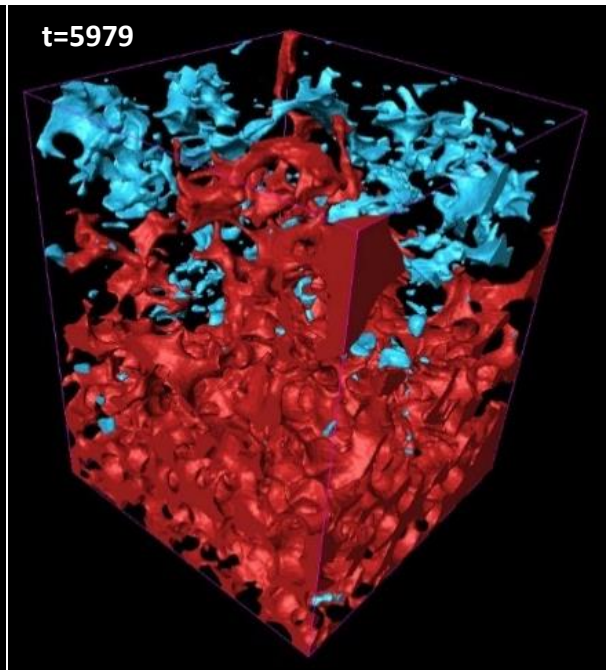
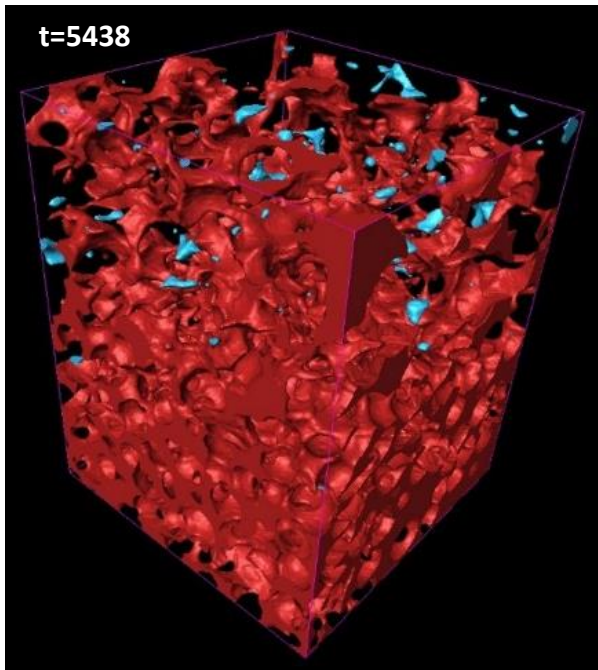
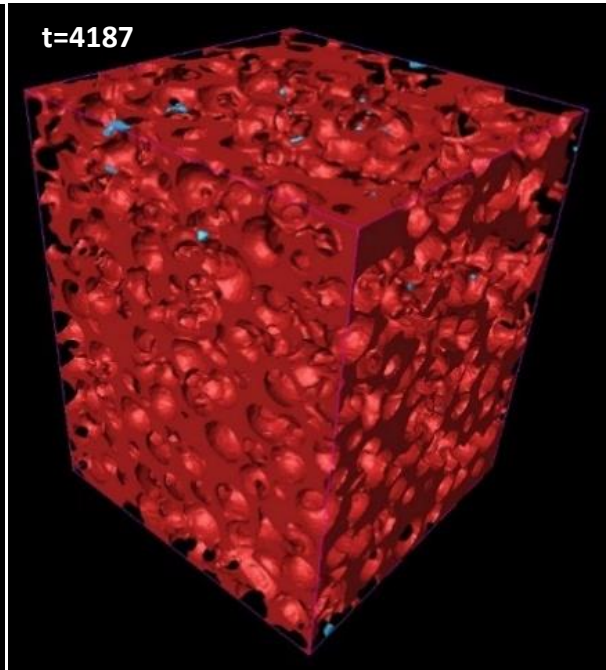
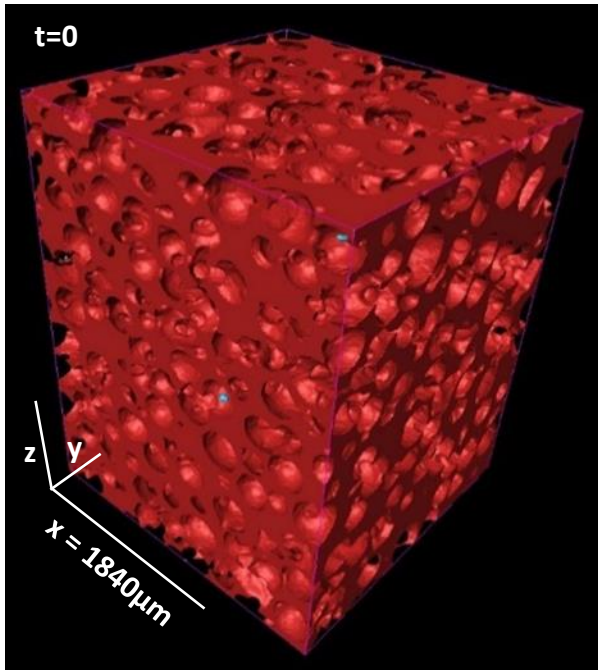


Figure 4.3: Evolution of overall and disconnected porosity (all axes) from a large and small subvolume for Experiment 10\_860\_longrun, showing reduction in overall porosity and increase in disconnected porosity as the experiment progresses. Markers and standard error: Square = all porosity LSV ( $\pm 0.036$ ). Circle = all porosity SSV ( $\pm 0.034$ ). Plus = disconnected porosity LSV ( $\pm 0.001$ ; smaller than marker size). Cross = disconnected porosity SSV ( $\pm 0.003$ ; smaller than marker size). Red point = furnace temperature.





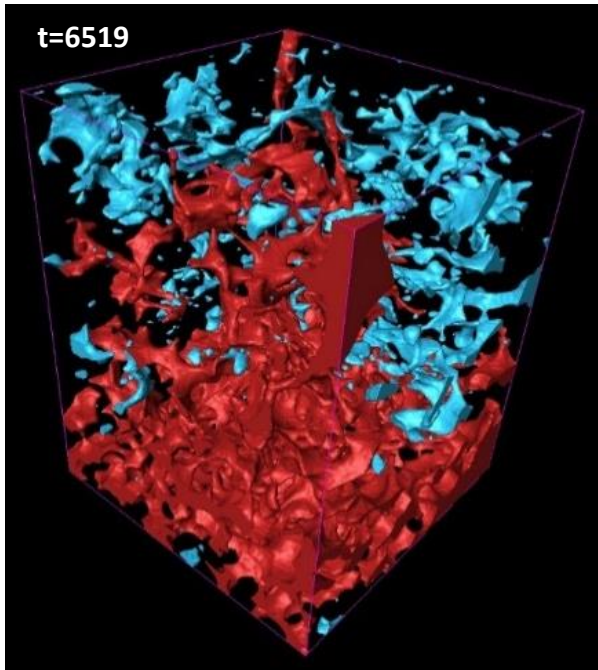


Figure 4.4: 3D renders of the large subvolume porosity network during sintering of 10 wt% crystal (10\_860\_longrun) showing the reducing connected porosity through time. Porosity connected through the z-axis is shown in red, porosity disconnected through the z-axis is shown in blue. Time point within experiment is given in seconds. Orientation and scale of all images identical throughout.

A third experiment with 10 wt% crystal (10\_860) was performed at a lower single dwell temperature. Here the data show a decrease in total porosity and increase in total porosity over the course of the experiment (Figure 4.5). The same trend is seen in both subvolumes. Initially, the LSV porosity network is fully connected through the z-axis. Focussed in the top quarter of the subvolume, more pores become disconnected as the experiment progresses. The whole network is disconnected through the z-axis by the end of the experiment, but the majority of the pores are still connected through the x-axis and y-axis (Figure 4.6, Figure 4.7).

The total porosity values of the big and small subvolume start out identical (0.419) but begin to diverge around 1000 seconds. The largest difference is 0.06 at 1940 seconds as the smaller subvolume porosity decreases faster and greater. Likewise, the disconnected values are initially identical and remain so until 2600 seconds. The porosity values do not converge in either subvolume with approximately 90% of the LSV porosity network connected through the x- and y-axes at the end of the experiment, and ~18% of the SSV porosity network connected.

The data suggest that neither subvolume reached a final equilibrium porosity and sintering is incomplete.

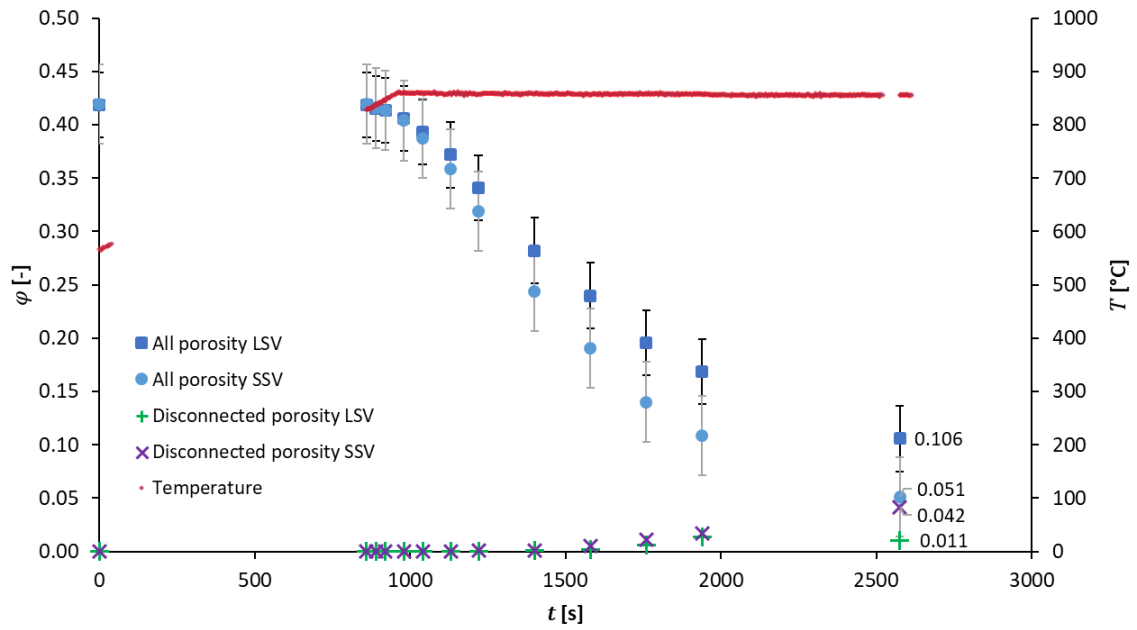
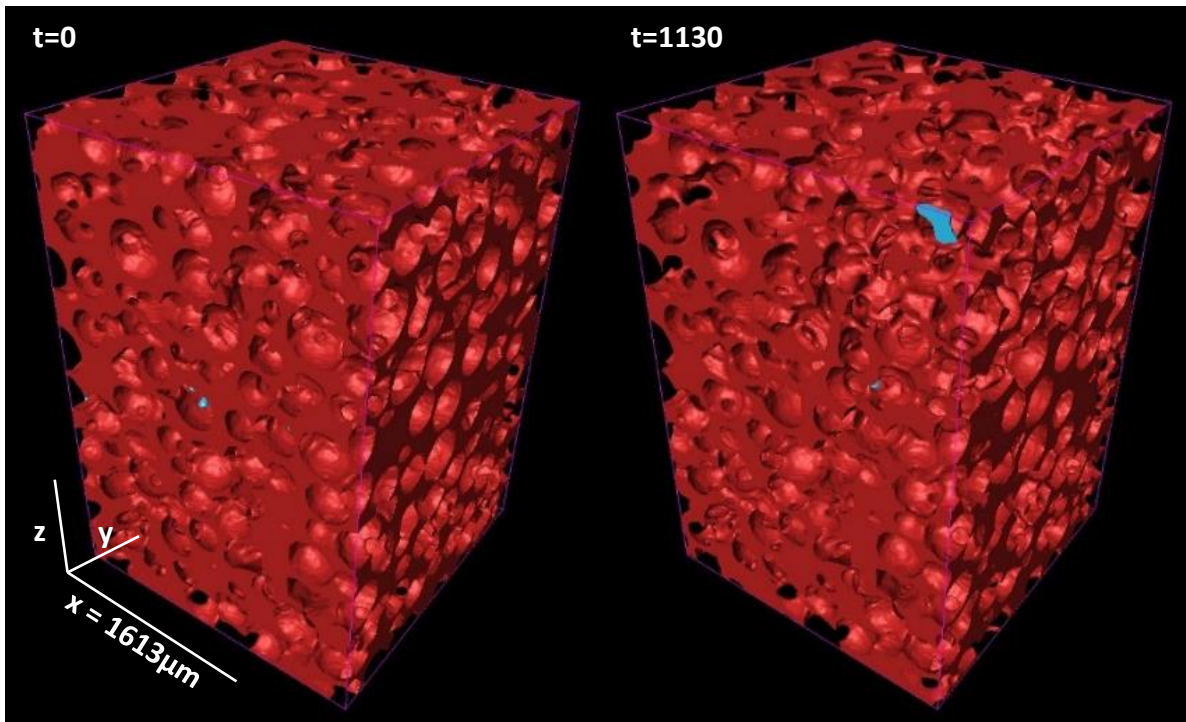


Figure 4.5: Evolution of overall and disconnected porosity (all axes) from a large and small subvolume for Experiment 10\_860, showing reduction in overall porosity and increase in disconnected porosity as the experiment progresses. Markers and standard error: Square = all porosity LSV ( $\pm 0.031$ ). Circle = all porosity SSV ( $\pm 0.037$ ). Plus = disconnected porosity LSV ( $\pm 0.001$ ; smaller than marker size). Cross = disconnected porosity SSV ( $\pm 0.003$ ; smaller than marker size). Red point = furnace temperature.



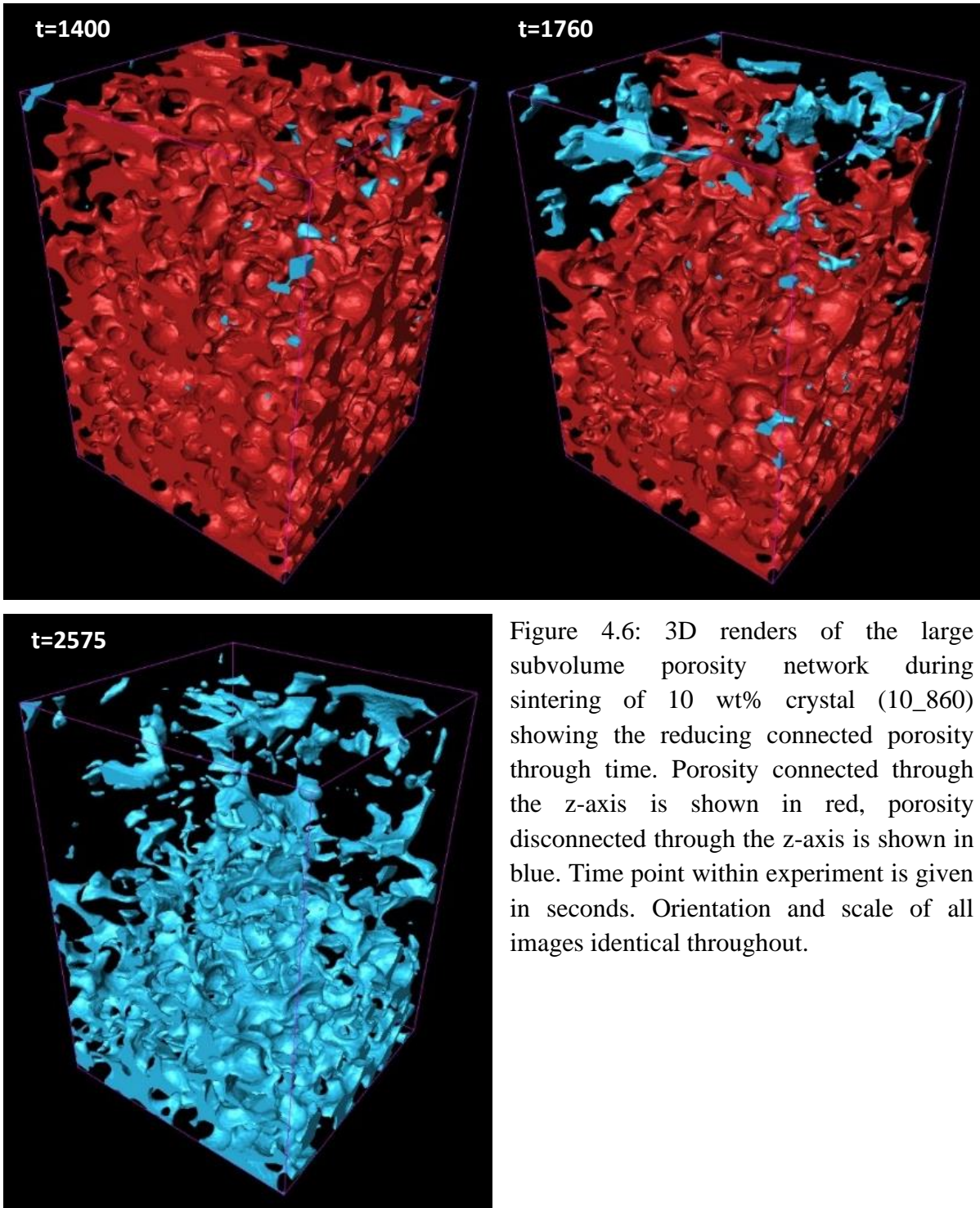


Figure 4.6: 3D renders of the large subvolume porosity network during sintering of 10 wt% crystal (10\_860) showing the reducing connected porosity through time. Porosity connected through the z-axis is shown in red, porosity disconnected through the z-axis is shown in blue. Time point within experiment is given in seconds. Orientation and scale of all images identical throughout.

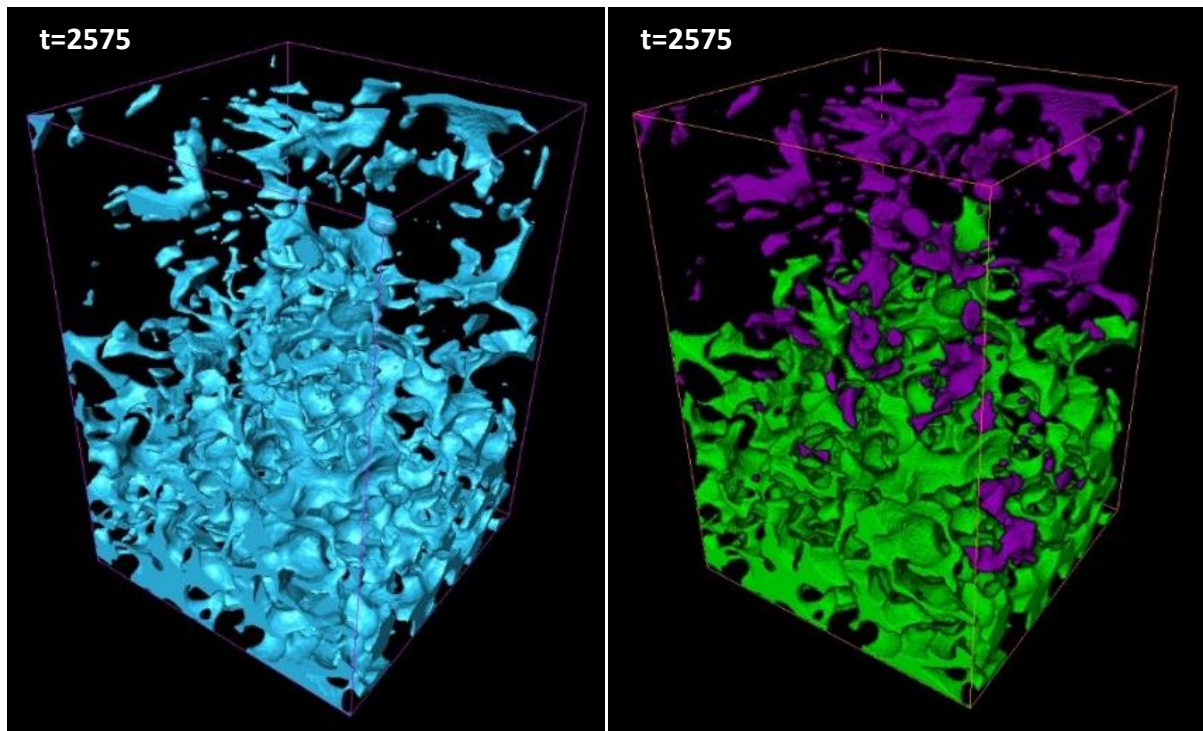


Figure 4.7: 3D renders of the LSV porosity network during sintering of 10% crystal (10\_860) at  $t=2575$ . The porosity disconnected through the z-axis is shown in blue (left). The truly isolated pores (pores not connected through any axis) are shown in purple and the porosity still connected through an axis (x or y) is displayed in green. Time point within experiment is given in seconds. The orientation and scale of images is identical.

The 20 wt% crystal experiment (20\_880) sintered at the highest single dwell temperature. In both subvolumes, the total porosity decreases, and the disconnected porosity increases over the course of the experiment (Figure 4.8). The LSV porosity network is initially fully connected through the z-axis. Few disconnected pores appear in the top half of the sample before the entire network is disconnected through the z-axis from 1234 seconds onwards (Figure 4.9). Pores continue to disconnect from the main network and at 1774 seconds, there are no longer any pores that completely connect through the sample in any axis (Figure 4.10)

While the total porosity values are initially similar between the two subvolumes (0.413 and 0.410), the values diverge over the course of the experiment, up to  $\sim 0.07$ , before converging towards similar values once more (LSV 0.043, SSV 0.046). Likewise, the disconnected porosities of both subvolumes start with the same value, begin to diverge at 1000 seconds and converge to their respective total porosities by 1774 seconds. By the end of the experiment, none of the porosity remaining in either subvolume is connected through any axis. The data

suggest that both the LSV and SSV have reached a final equilibrium porosity and that sintering is complete in both regions.

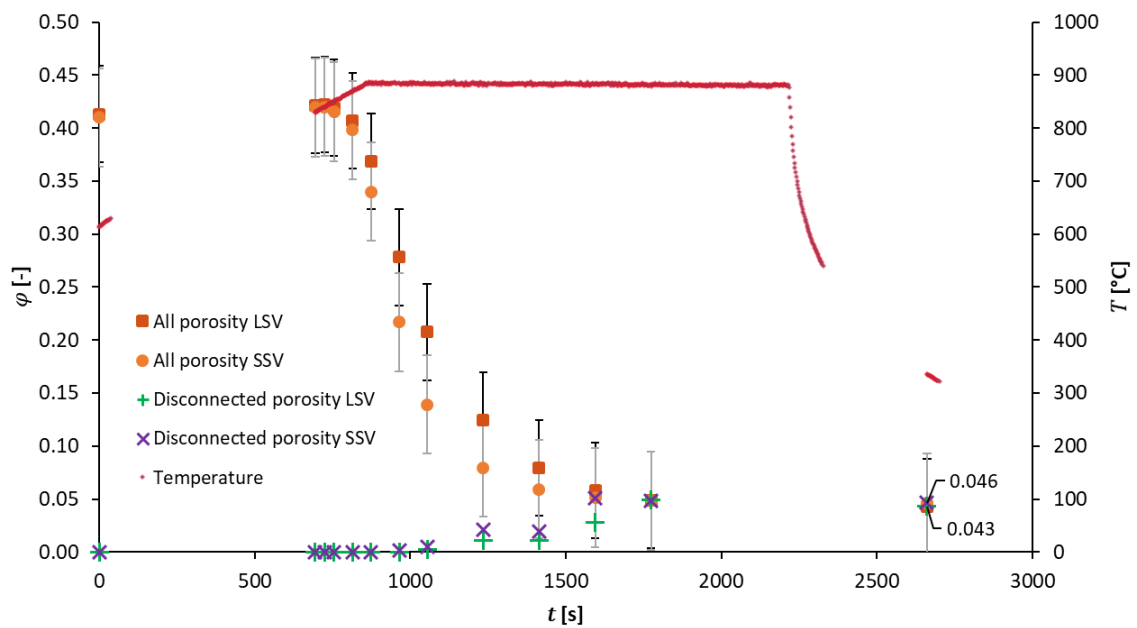
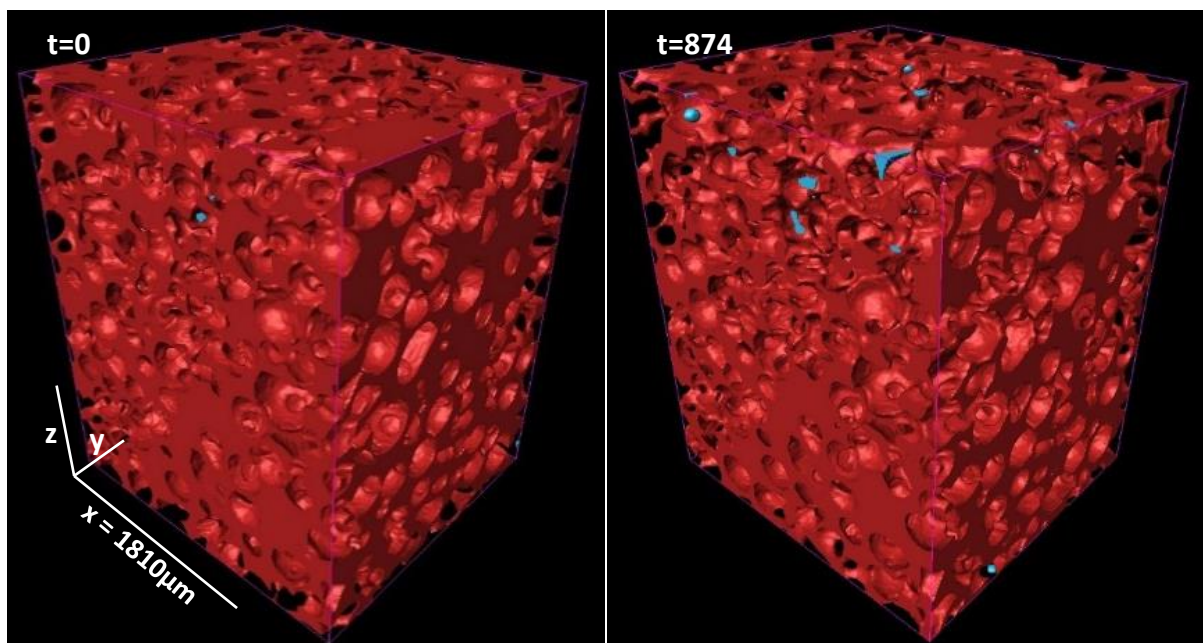


Figure 4.8: Evolution of overall and disconnected porosity (all axes) from a large and small subvolume for Experiment 20\_880, showing reduction in overall porosity and increase in disconnected porosity as the experiment progresses. The final values are displayed. Markers and standard error: Square = all porosity LSV ( $\pm 0.045$ ). Circle = all porosity SSV ( $\pm 0.047$ ). Plus = disconnected porosity LSV ( $\pm 0.005$ ; smaller than marker size). Cross = disconnected porosity SSV ( $\pm 0.006$ ; smaller than marker size). Red point = furnace temperature.



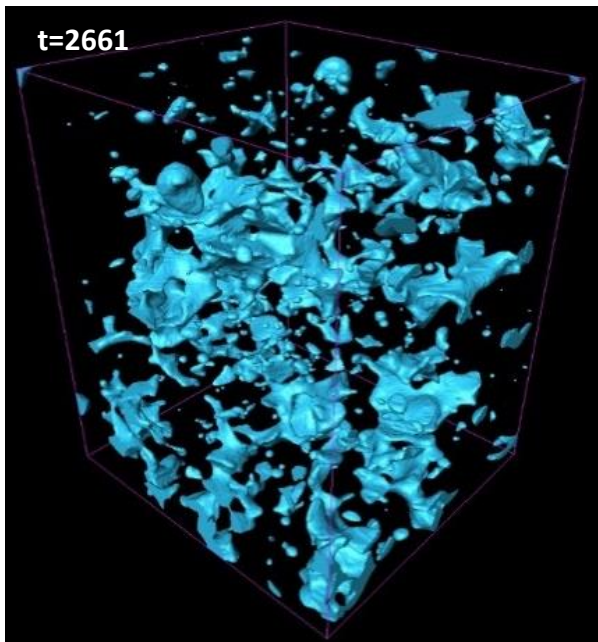
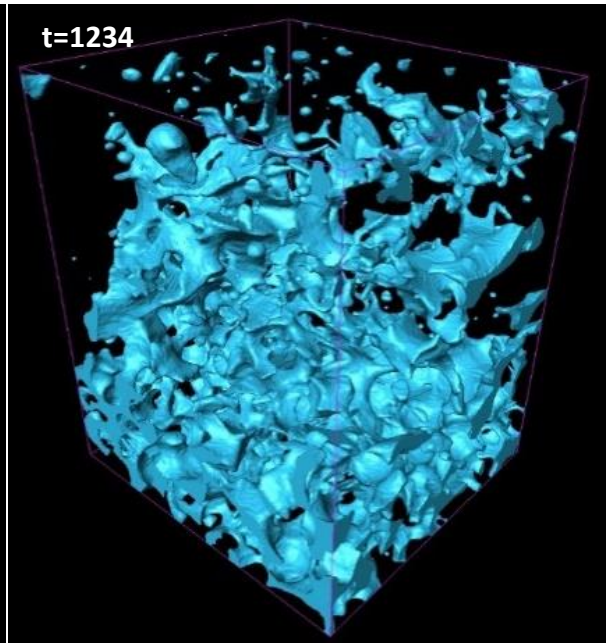
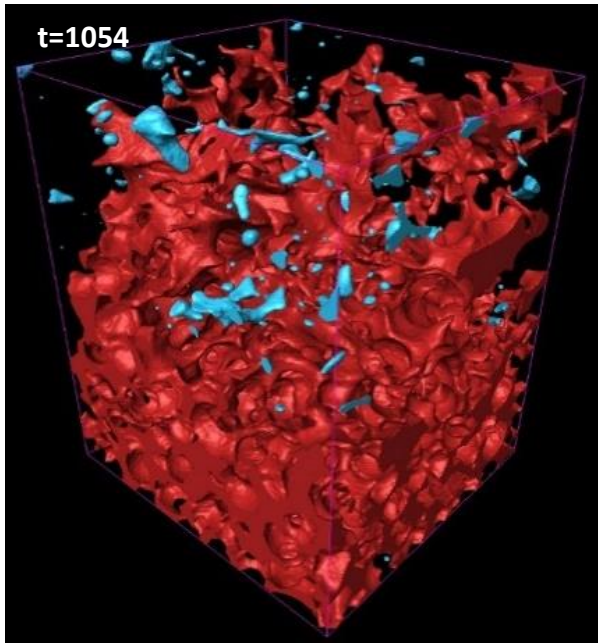


Figure 4.9: 3D renders of the large subvolume porosity network during sintering of 20 wt% crystal (20\_880) showing the reducing connected porosity through time. Porosity connected through the z-axis is shown in red, porosity disconnected through the z-axis is shown in blue. Time point within experiment is given in seconds. Orientation and scale of all images identical throughout.

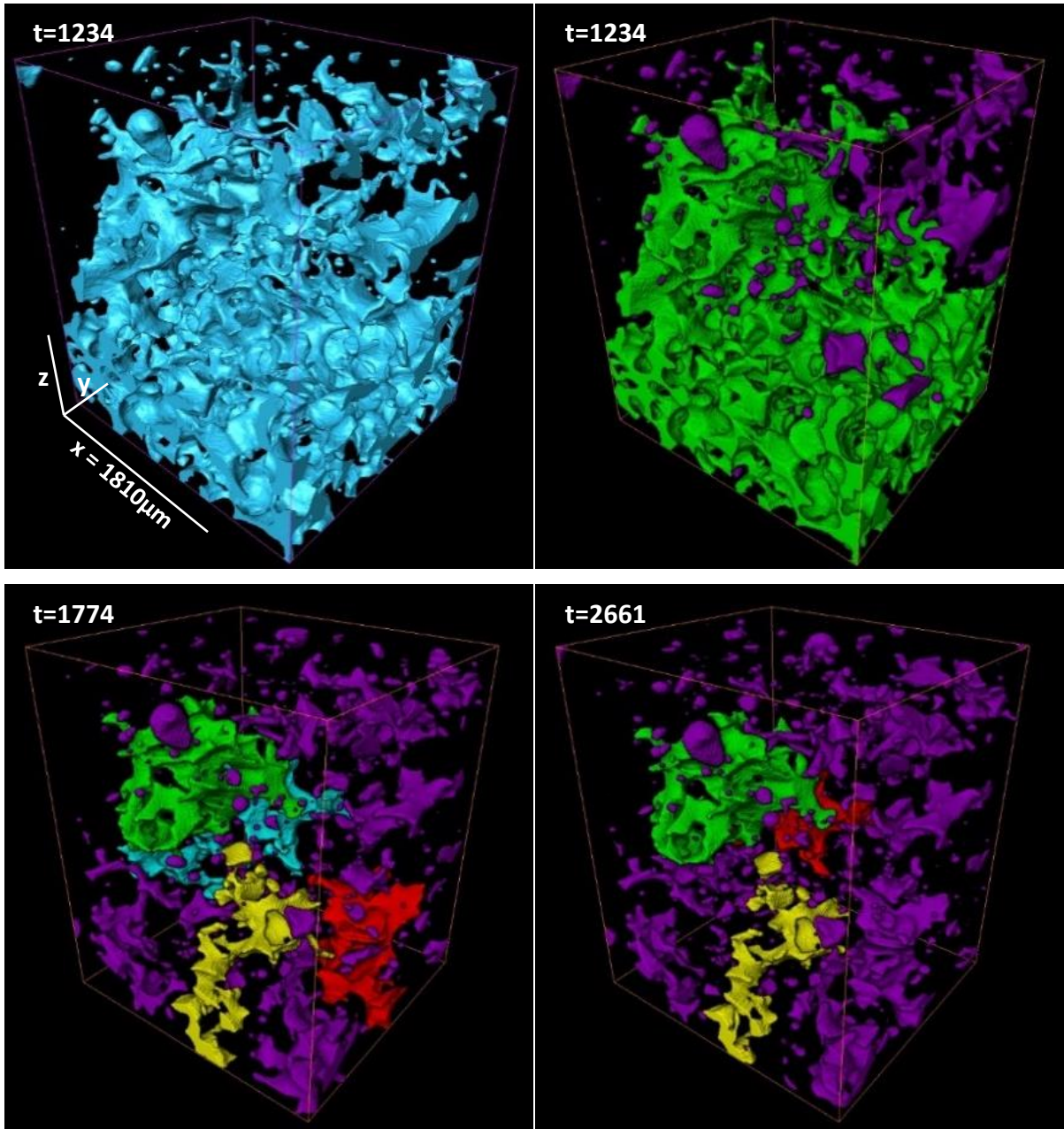


Figure 4.10: 3D renders of the LSV porosity network during sintering of 20 wt% crystal (20\_880) from  $t=1234$ . The porosity disconnected through the z-axis is shown in blue (top left). The truly isolated pores (pores not connected through any axis) are shown in purple and the porosity still connected through an axis (x or y) is displayed in green (top right). Smaller convoluted pores shown in green, blue, yellow, and red, become disconnected from the main network as sintering continues (bottom left and right). Time point within experiment is given in seconds. Orientation and scale of all images identical throughout.

A second 20 wt% crystal experiment (20\_860) sintered at the lower single dwell temperature. In both subvolumes, the total and disconnected porosity decrease and increase respectively over the course of the experiment (Figure 4.11). The LSV porosity network is fully connected through the z-axis initially, with most disconnected pores appearing in the top half of the sample as time goes on. Most of the network is still connected in all directions by the end of the experiment (Figure 4.12).

The initial total porosity of the LSV and SSV are 0.467 and 0.475 respectively. The divergence of values begins at ~1100 seconds as the porosity decreases faster and greater in the small subvolume. The disconnected porosities are identical for both subvolumes, only differing by 0.007 at the end of the experiment, and neither converge with the total porosity resulting in ~99% of the pores connected in any direction in the LSV, and ~94% in the SSV. The data suggests neither region reached final equilibrium porosity, and that sintering is incomplete.

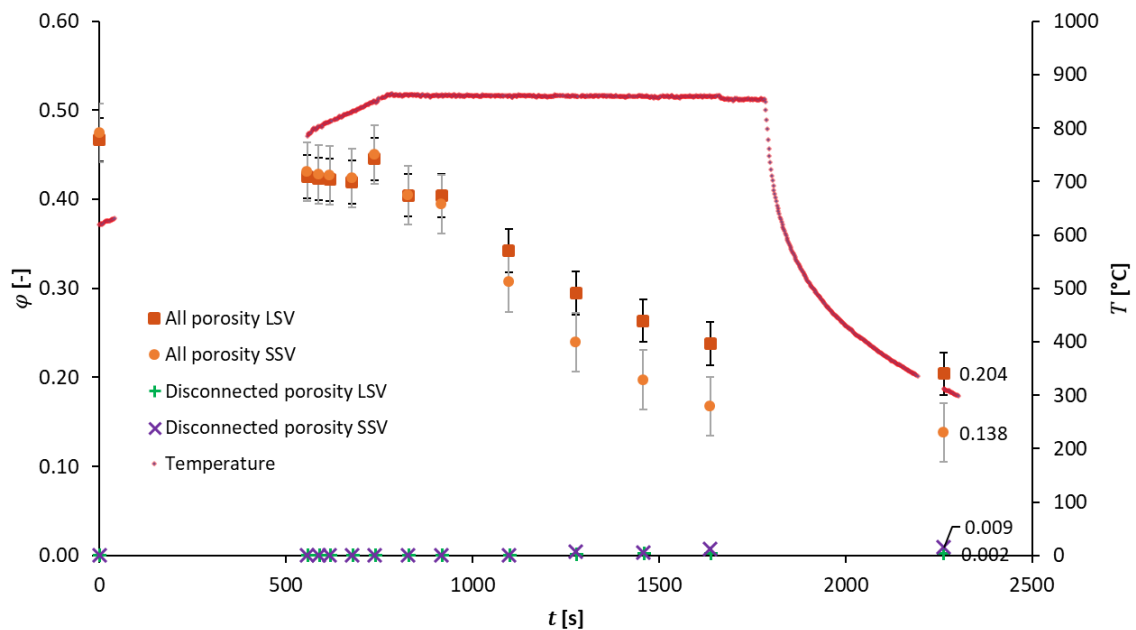


Figure 4.11: Evolution of overall and disconnected porosity (all axes) from a large and small subvolume for Experiment 20\_860, showing reduction in overall porosity and increase in disconnected porosity as the experiment progresses. Markers and standard error: Square = all porosity LSV ( $\pm 0.024$ ). Circle = all porosity SSV ( $\pm 0.033$ ). Plus = disconnected porosity LSV ( $\pm 0.0003$ ; smaller than marker size). Cross = disconnected porosity SSV ( $\pm 0.001$ ; smaller than marker size). Red point = furnace temperature.



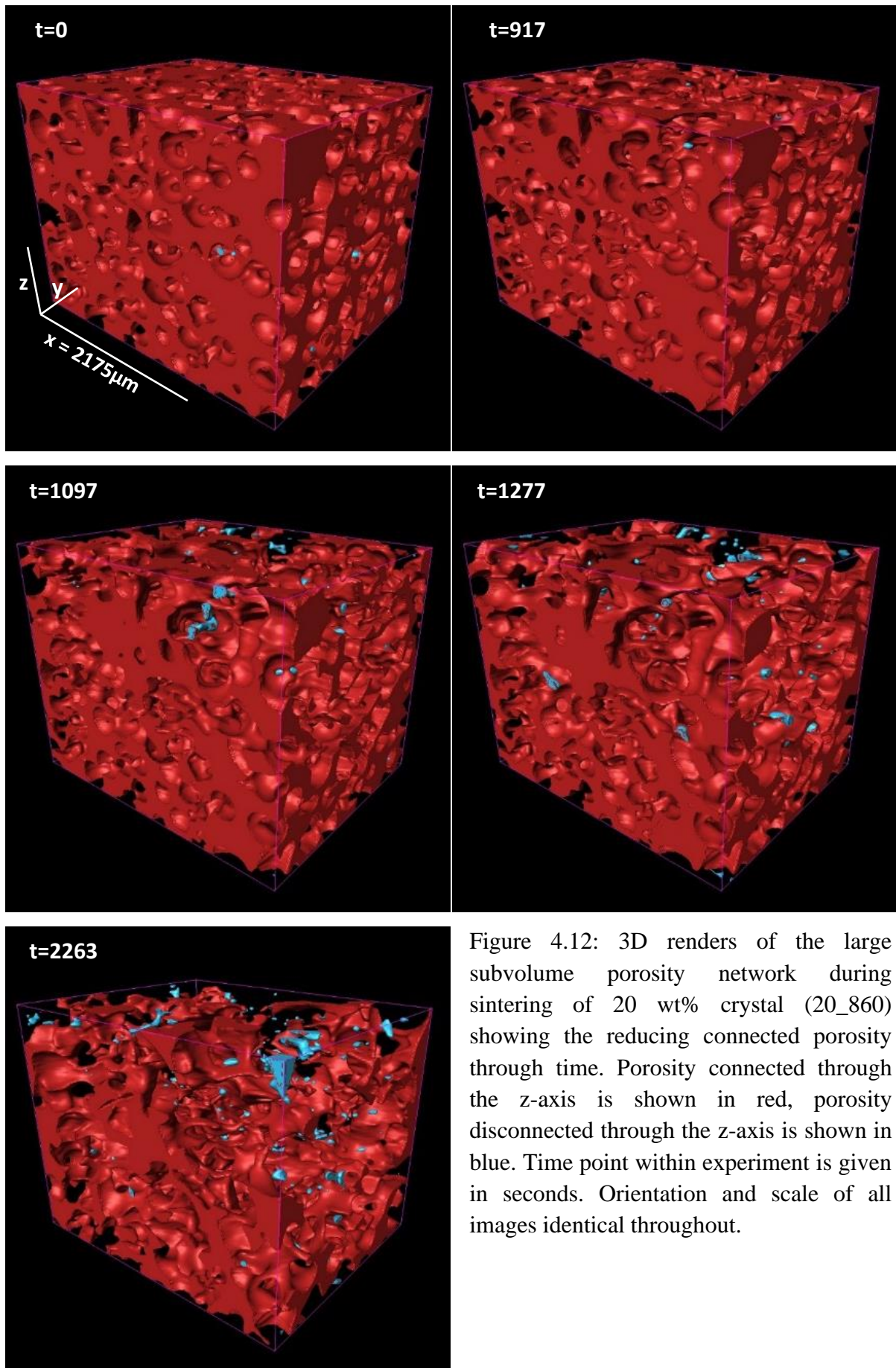


Figure 4.12: 3D renders of the large subvolume porosity network during sintering of 20 wt% crystal (20\_860) showing the reducing connected porosity through time. Porosity connected through the z-axis is shown in red, porosity disconnected through the z-axis is shown in blue. Time point within experiment is given in seconds. Orientation and scale of all images identical throughout.

A third 20 wt% crystal experiment (20\_860\_polydisperse) ran at the lower single dwell temperature but with two crystal size populations,  $<90\ \mu\text{m}$  and  $<250\ \mu\text{m}$ . The total porosity decreases, and the disconnected porosity increases as the experiment progresses (Figure 4.13). This is true of both subvolumes. The LSV porosity network is fully connected through the z-axis and remains mostly connected as the experiment progresses and some small pores disconnect (Figure 4.14).

The initial total porosity of the LSV is 0.403 and of the SSV, 0.407. These values diverge as the experiment progresses by up to 0.016 as the smaller subvolume total porosity decreases marginally faster and by a greater amount. The disconnected porosity values are virtually identical for both subvolumes throughout with the largest divergence of 0.004 at the end of the experiment. The total and disconnected porosity values do not converge for either subvolume resulting in  $\sim 99\%$  and  $\sim 96\%$  of the LSV and SSV porosity networks, respectively, connected through any axis. The data suggest that final equilibrium porosity has not been reached and that sintering is incomplete in both regions of the sample.

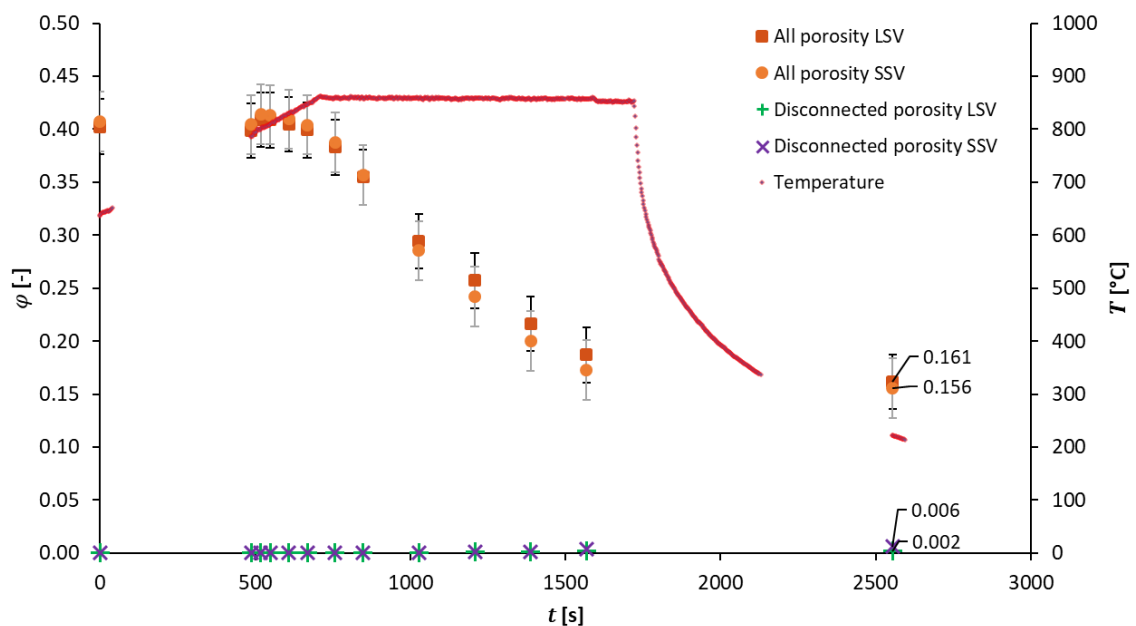


Figure 4.13: Evolution of overall and disconnected porosity (all axes) from a large and small subvolume for Experiment 20\_860\_polydisperse, showing reduction in overall porosity and increase in disconnected porosity as the experiment progresses. The final values are displayed. Markers and standard error: Square = all porosity LSV ( $\pm 0.026$ ). Circle = all porosity SSV ( $\pm 0.028$ ). Plus = disconnected porosity LSV ( $\pm 0.0002$ ; smaller than marker size). Cross = disconnected porosity SSV ( $\pm 0.001$ ; smaller than marker size). Red point = furnace temperature.

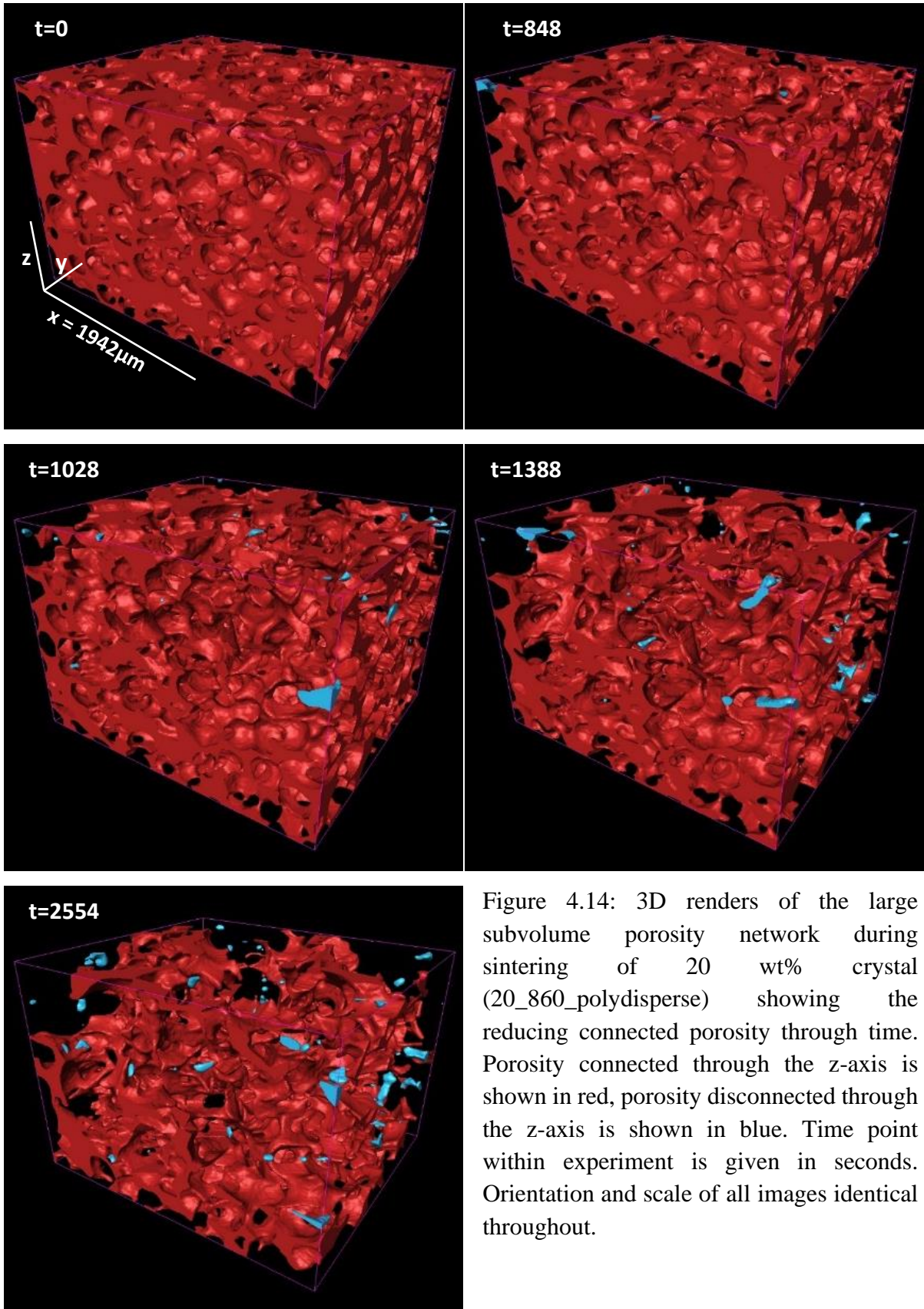


Figure 4.14: 3D renders of the large subvolume porosity network during sintering of 20 wt% crystal (20\_860\_polydisperse) showing the reducing connected porosity through time. Porosity connected through the z-axis is shown in red, porosity disconnected through the z-axis is shown in blue. Time point within experiment is given in seconds. Orientation and scale of all images identical throughout.

The 30 wt% crystal experiment (30\_880) sintered at the highest single dwell temperature. The total porosity decreases, and the disconnected porosity increases in both subvolumes (Figure 4.15). The LSV porosity network is fully connected through the z-axis initially, with a few isolated pores first appearing in the top quarter of the sample at  $t=910$ . As the experiment progresses, more pores become disconnected throughout the sample with a mix of z-axis connected and z-axis disconnected porosity remaining at the experiment end (Figure 4.16).

The total porosity values of the subvolumes diverge from the initial 0.404 and 0.395 as the experiment progresses. The decrease in total porosity is greater and faster in the smaller subvolume. Likewise, the disconnected porosities agree for the first 800 seconds. The disconnected porosity of the SSV converges with the total porosity at  $\sim 1250$  seconds meaning no porosity connects through the sample in any direction. The LSV, in comparison, has  $\sim 55\%$  of the pore network still connected at the end of the experiment. The data suggest that the smaller subvolume has reached a final equilibrium porosity within the highly sintered region, the larger subvolume has not reached a final equilibrium porosity, and sintering is complete in some regions but not throughout the whole sample.

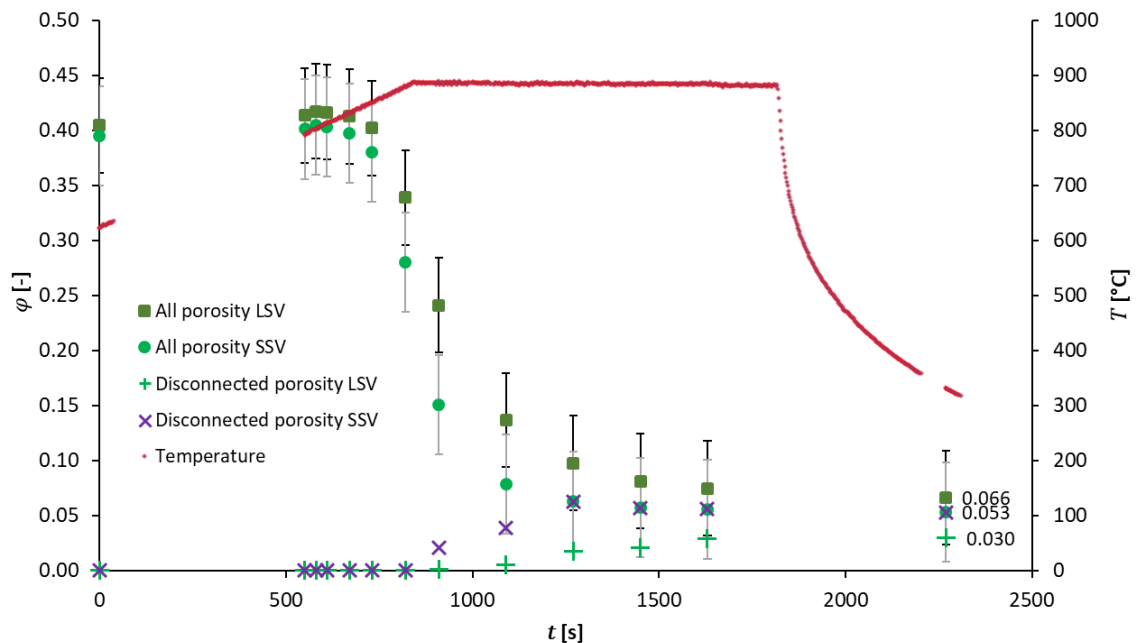
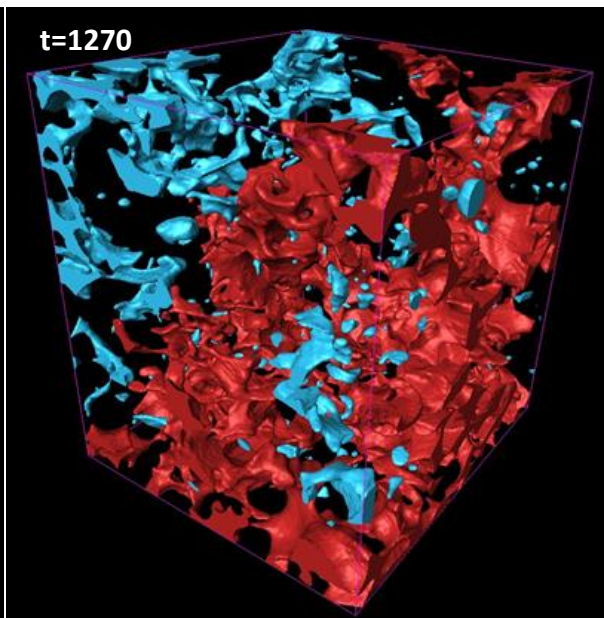
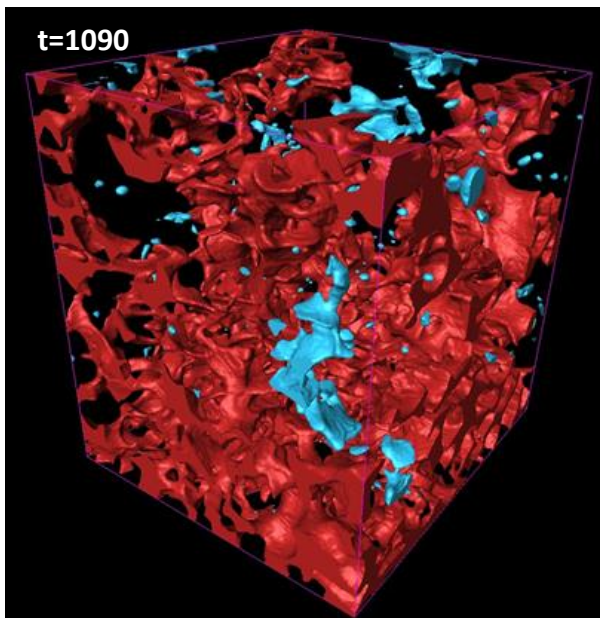
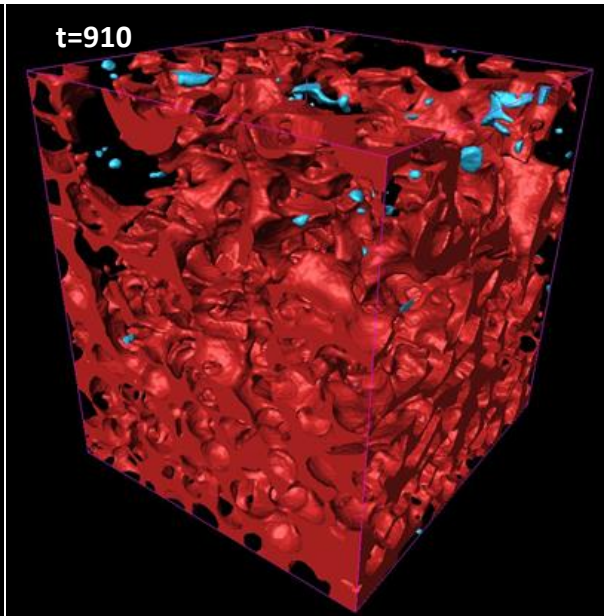
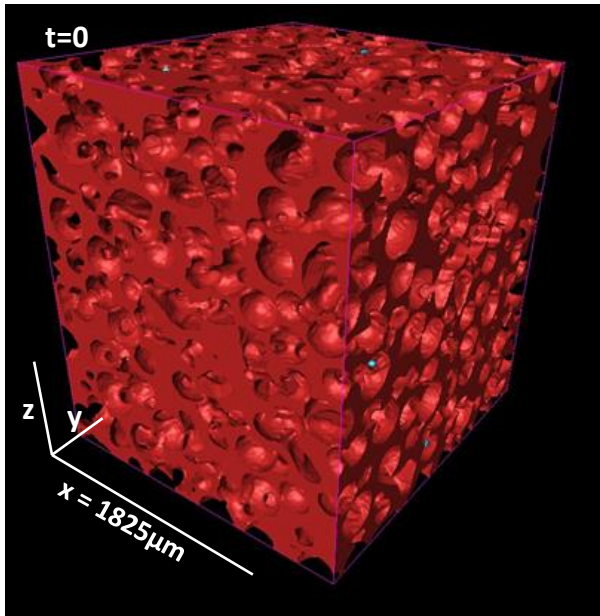


Figure 4.15: Evolution of overall and disconnected porosity (all axes) from a large and small subvolume for Experiment 30\_880, showing reduction in overall porosity and increase in disconnected porosity as the experiment progresses. The final values are displayed. Markers and standard error: Square = all porosity LSV ( $\pm 0.043$ ). Circle = all porosity SSV ( $\pm 0.045$ ). Plus = disconnected porosity LSV ( $\pm 0.003$ ; smaller than marker size). Cross = disconnected porosity SSV ( $\pm 0.007$ ; smaller than marker size). Red point = furnace temperature.



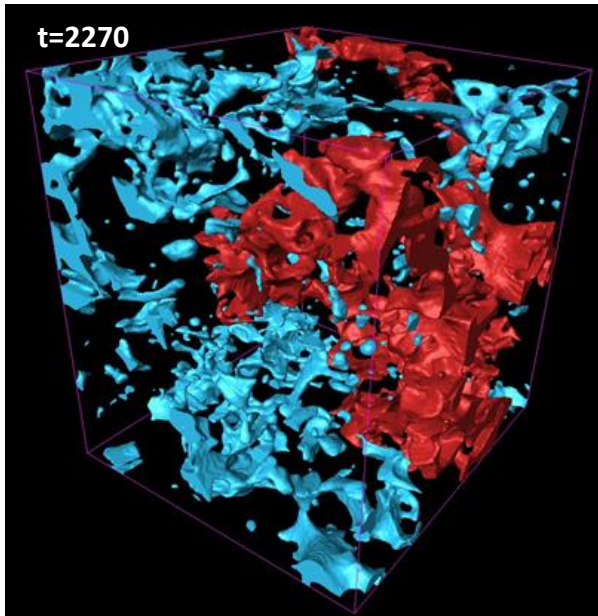


Figure 4.16: 3D renders of the large subvolume porosity network during sintering of 30 wt% crystal (30\_880) showing the reducing connected porosity through time. Porosity connected through the z-axis is shown in red, porosity disconnected through the z-axis is shown in blue. Time point within experiment is given in seconds. Orientation and scale of all images identical throughout.

The second 30 wt% crystal experiment (30\_860) ran at the lower single dwell temperature. Again, the total porosity and disconnected porosity decrease and increase respectively as the experiment progresses and is true for both subvolumes (Figure 4.17). The LSV porosity network is fully connected through the z-axis initially. The appearance of disconnected porosity throughout the experiment is focussed towards the central band of the subvolume (Figure 4.18).

The initial total porosity of the LSV and SSV are 0.394 and 0.389 respectively. The values diverge further over the course of the experiment, with the decrease in total porosity marginally faster and greater in the smaller subvolume. The disconnected porosities are in agreement throughout the experiment and reach a maximum value of 0.003. The remaining porosity connected in any direction of both the LSV and SSV is ~99%.

The data suggest that final equilibrium porosity has not been reached and that sintering is incomplete in both regions encompassed by the subvolumes. The large changes in total porosity in the first 500 seconds may be due to a crack running through the sample.

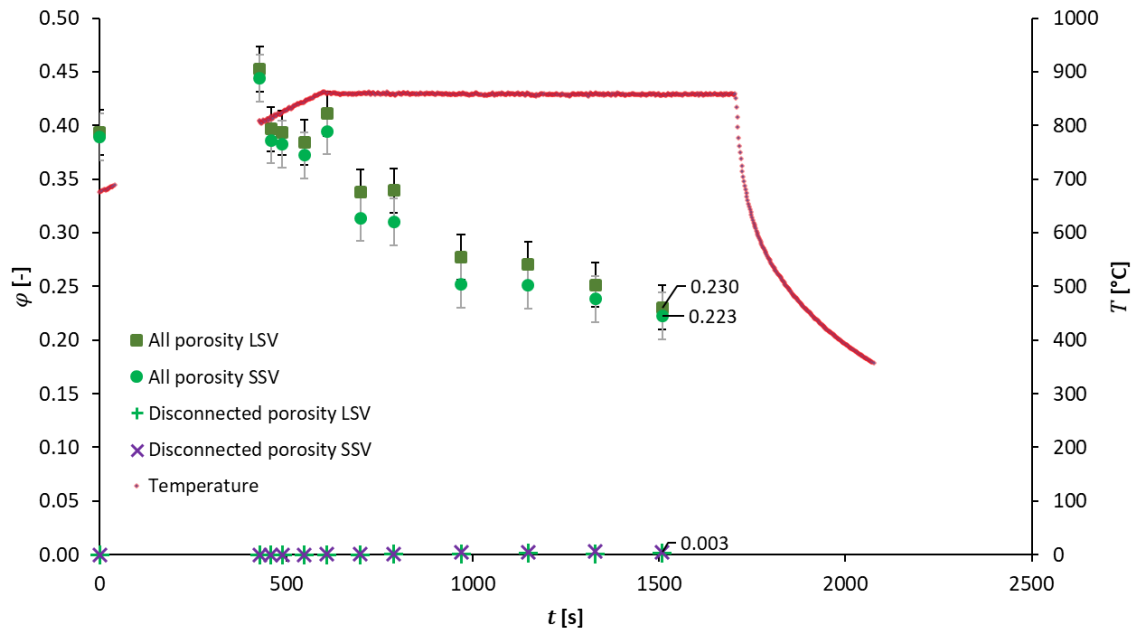
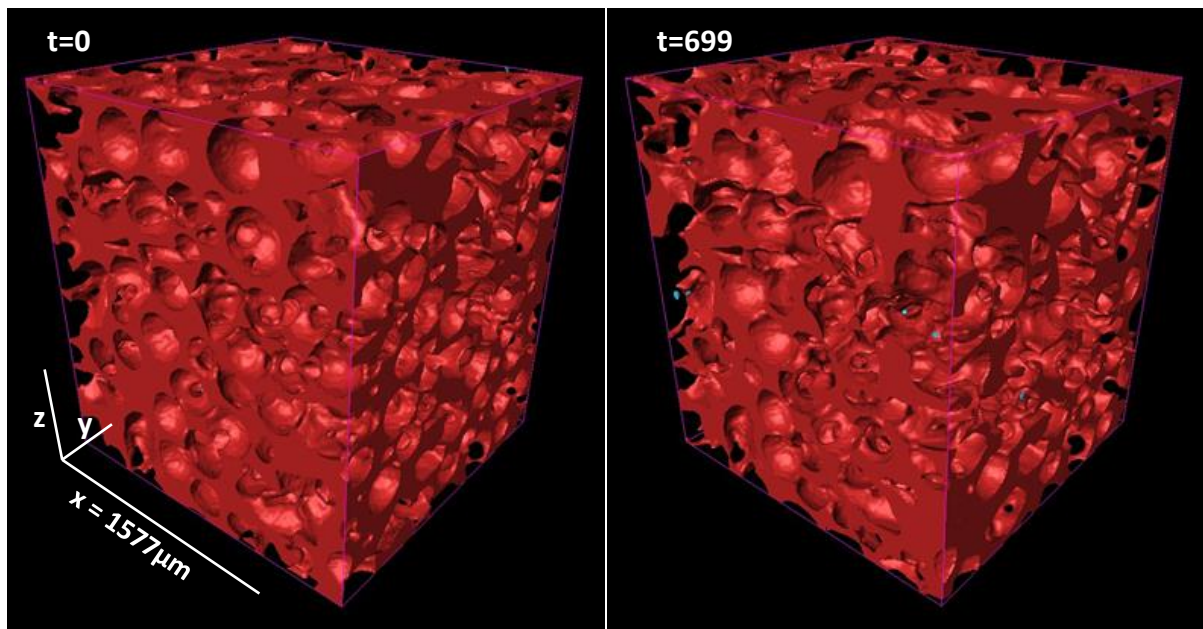


Figure 4.17: Evolution of overall and disconnected porosity (all axes) from a large and small subvolume for Experiment 30\_860, showing reduction in overall porosity and increase in disconnected porosity as the experiment progresses. The final values are displayed. Markers and standard error: Square = all porosity LSV ( $\pm 0.021$ ). Circle = all porosity SSV ( $\pm 0.022$ ). Plus = disconnected porosity LSV ( $\pm 0.0002$ ; smaller than marker size). Cross = disconnected porosity SSV ( $\pm 0.0004$ ; smaller than marker size). Red point = furnace temperature.



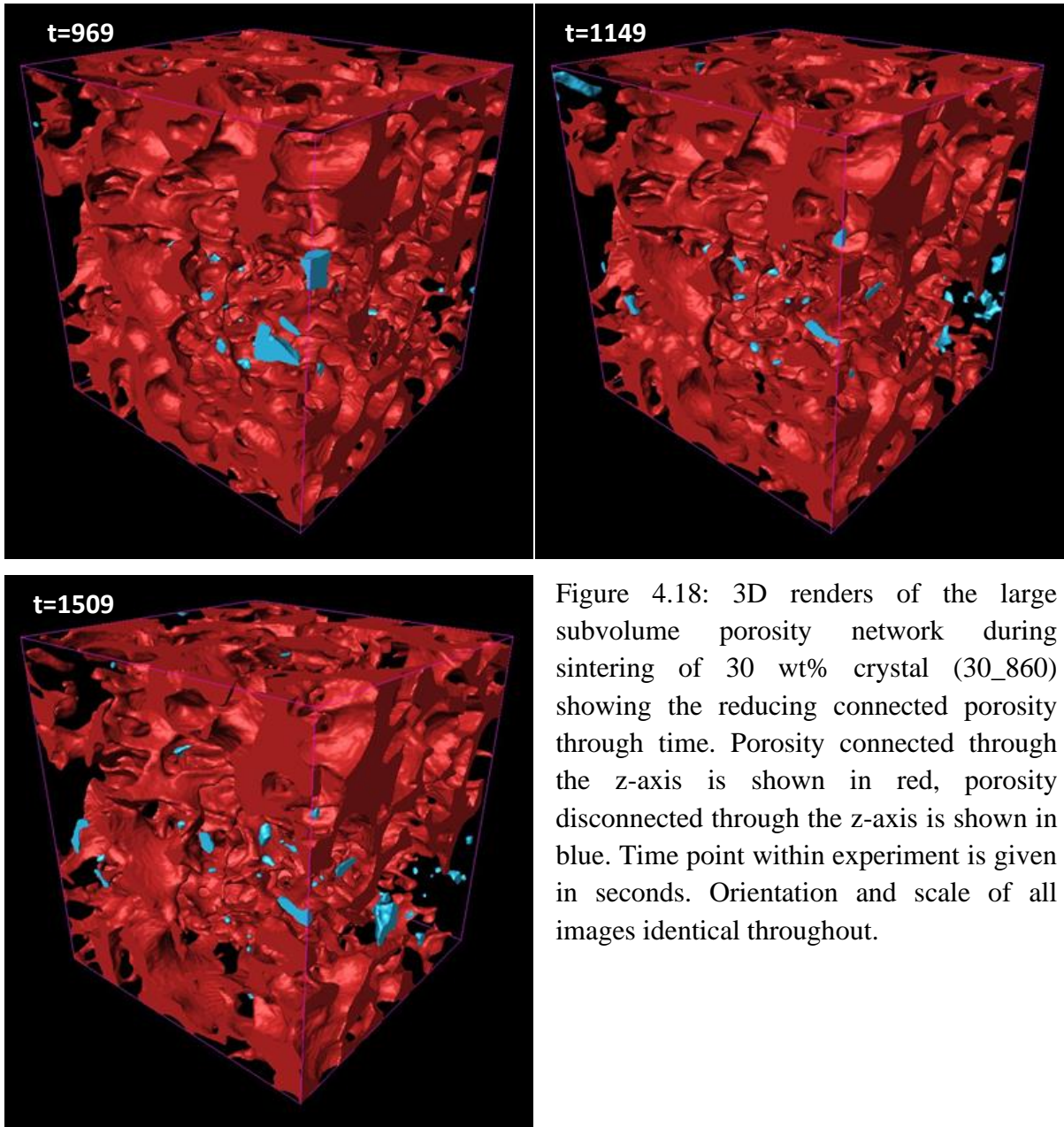


Figure 4.18: 3D renders of the large subvolume porosity network during sintering of 30 wt% crystal (30\_860) showing the reducing connected porosity through time. Porosity connected through the z-axis is shown in red, porosity disconnected through the z-axis is shown in blue. Time point within experiment is given in seconds. Orientation and scale of all images identical throughout.



### 4.1.2 Final porosities

The samples from 10\_880, 20\_880, and 30\_880 sintered at the highest single dwell temperature, 880°C. The final total porosity increases with a higher crystal content (Figure 4.19). A sintering sample with no rigid inclusions reaches an equilibrium porosity of ~0.03 (Wadsworth et al., 2016) which is used to extrapolate the linear fit for the data.

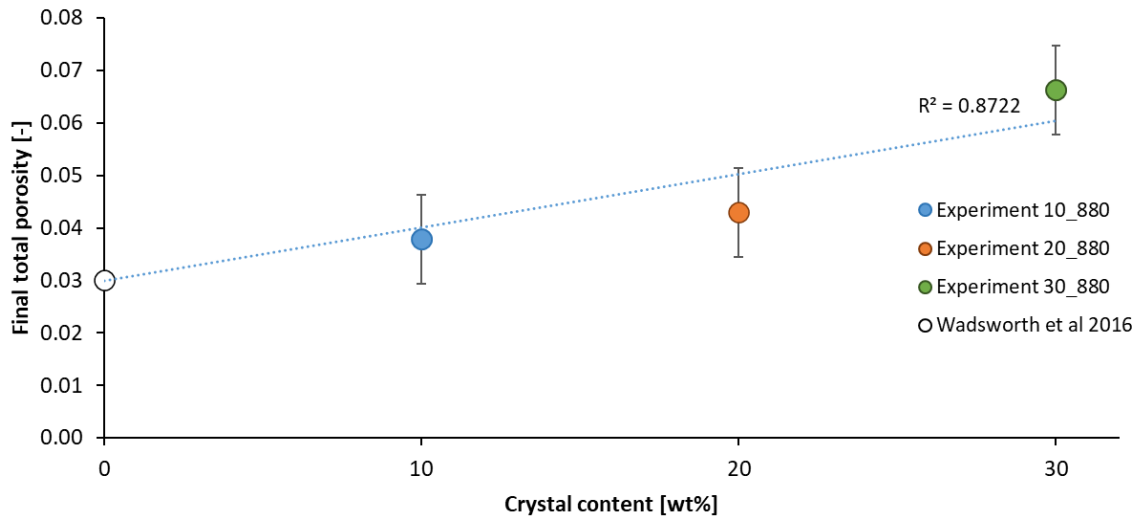


Figure 4.19: Final total porosity values (big extract) for highest dwell temperature experiments increasing with crystal content. Standard error  $\pm 0.00874$ .

The remainder of the experiments had a highest dwell temperature of 860°C. Again, the final total porosity increases with a higher crystal content (Figure 4.20). The final total porosity values of the 860°C experiments are 3-4 times greater than the lowest porosity value of their equivalent crystal content higher dwell temperature experiments. The data suggest that experiments that dwelled at 860°C did not sinter as much as the 880°C dwell experiments, and final total porosity is greater with higher crystal content, even when sintering is incomplete.

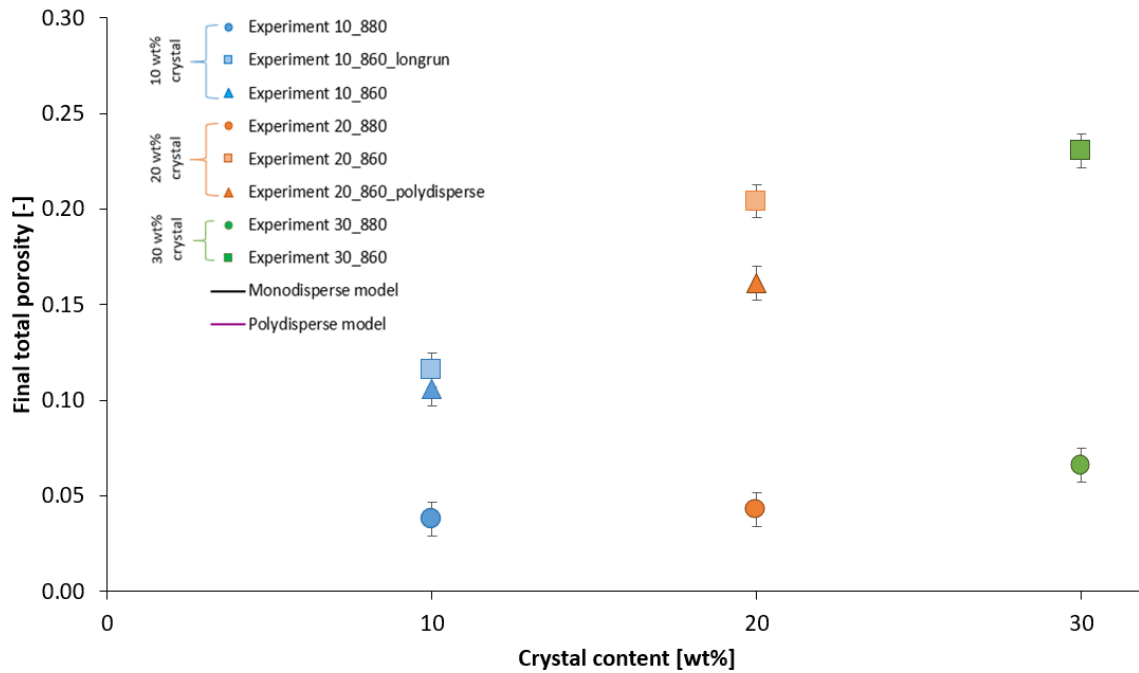


Figure 4.20: All final total porosity values for experiments (LSV). Error bars represent standard error calculated in previous figure ( $\pm 0.00874$ ). Blue symbols = 10 wt% crystal experiments. Blue circle = Experiment 10\_880. Blue square = Experiment 10\_860\_longrun. Blue triangle = Experiment 10\_860. Orange symbols = 20 wt% crystal experiments. Orange circle = Experiment 20\_880. Orange square = Experiment 20\_860. Orange triangle = Experiment 20\_860\_polydisperse. Green symbols = 30 wt% crystal experiments. Green circle = Experiment 30\_880. Green square = Experiment 30\_860.

### 4.1.3 Normalized porosity

As there were differing conditions between experiments, the results are normalized so that they can be compared to one another. All conditions with the exception of differing crystal content are accounted for by Equations 3.5. The results are offset from the monodisperse and polydisperse viscous sintering models of Wadsworth et al (2016) by approximately two orders of magnitude. The temperature correction of  $-106^{\circ}\text{C}$  (calculated in Section 3.4.3.1) is applied to all normalized results (Figure 4.21).

The shape of the data points curve is more similar to that of a monodisperse model. However, with increasing crystal content, the curve is marginally less steep, possibly due to a greater number of crystals making the system more polydisperse and increasing heterogeneity. There also seems to be a systematic overcorrection dependent on crystal content with the 10 wt% experiment closest to the monodisperse model, followed by the 20 wt% experiment, and the 30 wt% experiment furthest from the model.

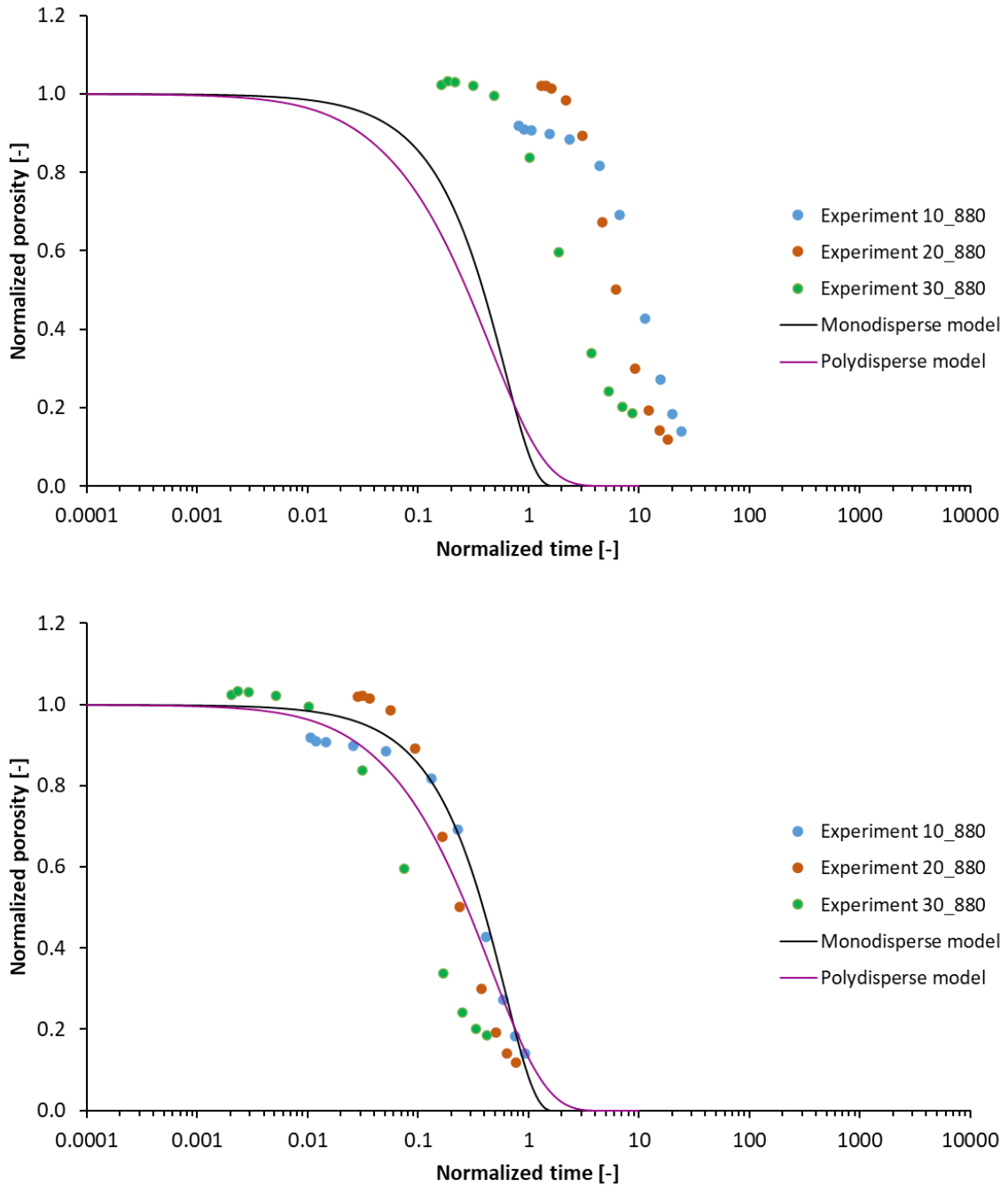


Figure 4.21. Temperature correction reducing the offset normalized total porosity (LSV) values for the High Dwell Temperature Group. Before (top) and after (bottom) temperature correction. Blue circle = Experiment 10\_880. Orange circle = Experiment 20\_880. Green circle = Experiment 30\_880. Black line = monodisperse model. Purple line = polydisperse model.

Equation 3.5 uses glass viscosity calculated using the VFT equation (3.6) which does not consider the effect of crystals. Therefore, Equation 3.9 is used for the viscosity, where the effect of suspended particles in a glass is considered. The spread of data around the monodisperse

line increases when glass viscosity with suspended particles is used to calculate normalized time (Figure 4.22).

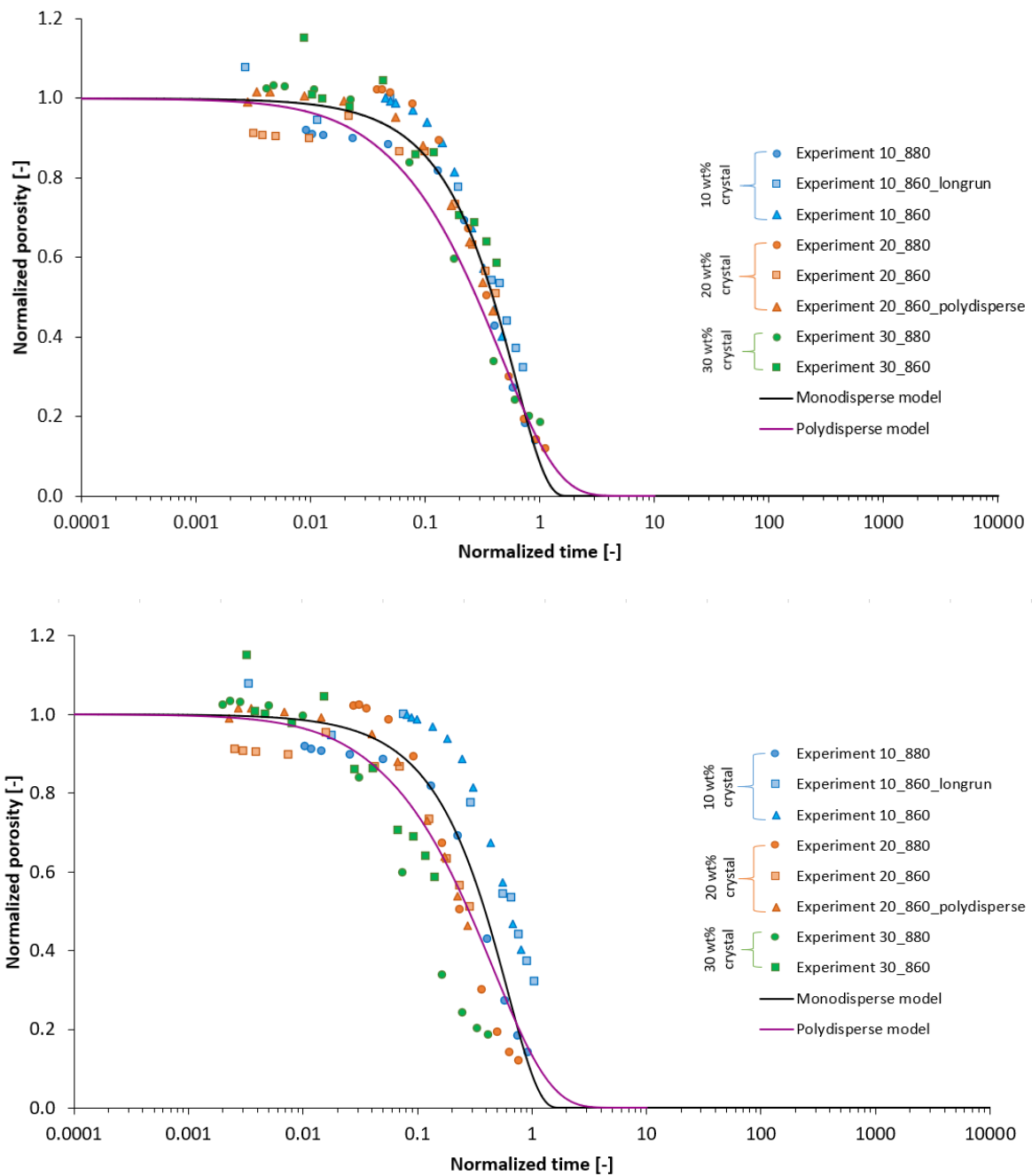


Figure 4.22: Normalized porosity (LSV) calculated with Eq 3.5 (top) and Eq 3.9 (bottom). The spread of data increases when normalized time is calculated using viscosity with suspended particles. Blue symbols = 10 wt% crystal experiments; circle = Experiment 10\_880, square = Experiment 10\_860\_longrun, triangle = Experiment 10\_860. Orange symbols = 20 wt% crystal experiments; circle = Experiment 20\_880, square = Experiment 20\_860, triangle = Experiment 20\_860\_polydisperse. Green symbols = 30 wt% crystal experiments; circle = Experiment 30\_880, square = Experiment 30\_860. Black line = monodisperse model. Purple line = polydisperse model.

#### 4.1.4 Connectivity

The connectivity of large subvolumes for all experiments decreases with total porosity (Figure 4.23). Connectivity remains near 1 until total porosity reaches  $\sim 0.17-0.23$ , after which connectivity decreases with total porosity. The connectivity of 20\_880 is the only of the experiments to reach 0 (total porosity = 0.05).

As established in Section 4.1.1, porosity decreases over time as the samples sinter. The data suggest that Experiment 20\_880 is the only experiment to encounter the percolation threshold (the porosity value at  $C = 0$ ),  $\varphi_c$  as  $\sim 0.05$ .

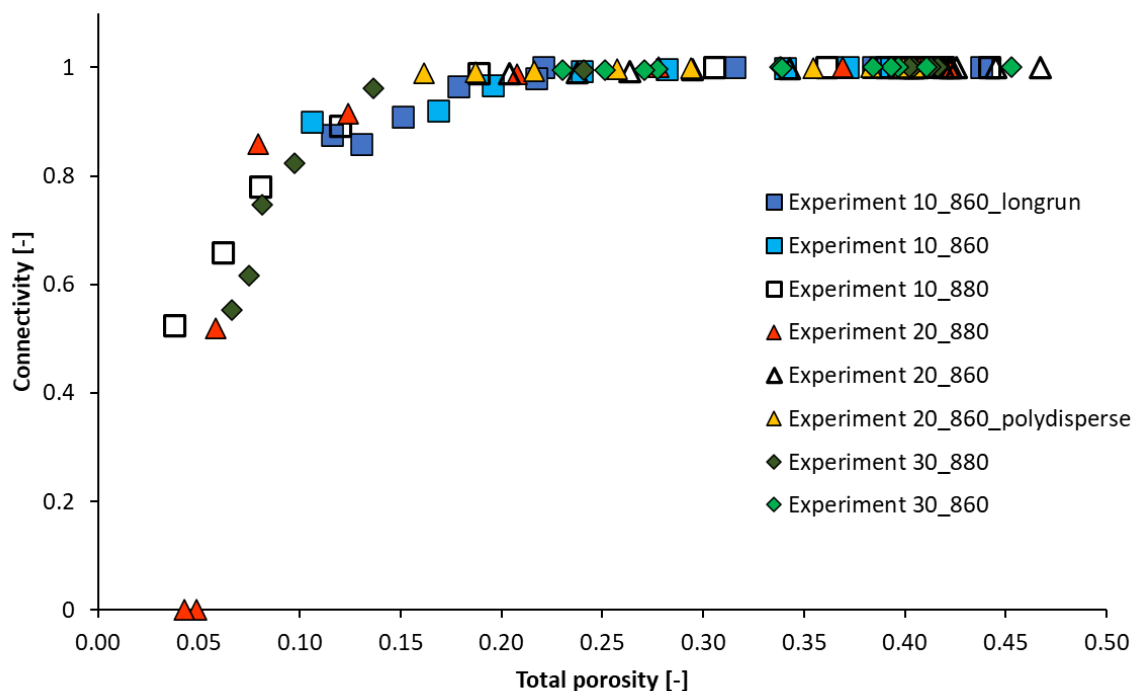


Figure 4.23: The covariance of connectivity and porosity for all experiments in this work. Dark blue square = Experiment 10\_860\_longrun. Light blue square = Experiment 10\_860. Open square = Experiment 10\_880. Red triangle = Experiment 20\_880. Open triangle = Experiment 20\_860. Yellow triangle = Experiment 20\_860\_polydisperse. Dark green diamond = Experiment 30\_880. Light green diamond = Experiment 30\_860.

#### 4.1.5 Pore analysis

The evolution of pores across the 10 wt% crystal (10\_880) and 30 wt% crystal (30\_880) experiments are compared using the parameters equivalent diameter, 3D shape, and volume.

The number of pores increase as Experiment 10\_880 progresses, with the initially right skewed equivalent diameter data morphing into a bimodal distribution (Figure 4.24). The distribution is initially polarised by one pore of extremely large diameter (>100 voxels) and the rest of equivalent diameters between 2 and 10 voxels. Over the course of the experiment, the number of smaller equivalent diameter pores increase, and pores with equivalent diameters between 20 and 100 voxels appear after  $t = 1203$ . The largest pore (>100 voxels) is no longer present at the end of the experiment. The data is initially unimodal, increasing from 2 to 4 to 6 voxels as time goes on. It becomes bimodal at  $t = 1383$  for the remainder of the experiment with peaks at 6 and 20 voxels. The data suggest that more pores appear as time goes by, possibly due to the large >100 voxel pore breaking down into increasing numbers of smaller equivalent diameter pores.

There are a greater number of pores, roughly double, at any given stage and the number of pores increase as the experiment (30\_880) progresses. The equivalent diameter data is also skewed right initially with a bimodal distribution appearing through the experiment. The initial modal peak at 4 voxels is a constant throughout the experiment, with the introduction of the second modal peak (20 voxels) at  $t = 1090$ . Larger diameter pores appear earlier in the experiment when compared to 10\_880 and the largest pore (>100 voxels) is still present in the final time step. The data suggest that a higher crystal content results in a greater number of pores and that larger pores are retained for a greater length of time.

The spread of equivalent diameter data is similar across both experiments, with modal peaks at the same equivalent diameters. However, fewer of the pores in 30\_880 have larger equivalent diameters when compared to 10\_880.

The shape of pores is initially unimodal, and the right skewed data shifts towards a bimodal distribution as the experiment (10\_880) progresses (Figure 4.25). The modal peak starts at 1 and as the experiment progresses, the skewed right modal peak shifts more left and strengthens, with 2 as the modal peak from  $t = 1203$  onwards. The second modal peak appears at 10 voxels at  $t = 1563$  and is present until experiment end. The data suggest that the majority of pores initially are close to spherical and the population becomes less spherical as time goes on. At

least one large convoluted pore shape is maintained throughout the experiment ( $>100$ ) and smaller, less convoluted shapes appear towards the end of the experiment.

Again, the unimodal shape factor data is initially skewed right and the strength of the peak increases as Experiment 30\_880 progresses. The modal peak is at 1 until  $t = 910$ , after which the peak is shared with 2 before the peak becomes clear at 2 at  $t = 1450$ . A deviation in the tail of the data at 10 appears at  $t = 910$  as a very weak second modal peak and is present until the experiment end. The data suggest that most pores are initially close to spherical and the population becomes less spherical throughout the experiment. A highly convoluted pore is maintained through the experiment and some less convoluted pore shapes appear towards the end.

The shape of the pores in both experiments is similar at any given time point, although Experiment 30\_880 has a greater ratio of convoluted shapes at 10 to spherical/near spherical pores (shape 1) than 10\_880.

The pore volumes are skewed right with the majority of pores composed of smaller volumes at any given time in the experiment (10\_880; Figure 4.26). Pores of volume  $\geq 1000$  voxels and  $\leq 20000$  voxels appear later in the experiment,  $t = 1203$  and onwards. Most of the timestamps are at least bimodal with peaks at 10 and 50 but some are trimodal or even multimodal with the third peak commonly at 500 voxels. There is at least one  $\geq 20000$  voxel volume pore present throughout the experiment which increases from  $t = 1383$ . The data suggest that there is one pore of massive volume with very few small pores initially. Small pores appear throughout the experiment and are most common. Larger pores appear later in the experiment and the largest pore possibly breaks down into several smaller (but still of volume  $>20000$  voxels) pores.

The distribution of pore volumes is similar with right skewed data and a majority of pores in initial stages of Experiment 30\_880 are of small volume. There is a strong initial peak at 10 voxel volume that strengthens as the experiment continues. A second peak appears at 50 voxel volume, the third peak at 500 voxel volume, and fourth peak at  $>20000$  voxel volume ( $t = 1090$ ). The data suggest that there is one pore of massive volume with few small pores initially. Small volume pores are most common and appear throughout the experiment, with larger pores becoming more common as the experiment progresses. The largest pore possibly breaks down into several smaller pores with volumes  $>20000$  voxels.

The multimodal peaks are clearer with the data of 30\_880 but both show the same large pore initially and few small pores, and the addition of pores with larger volumes throughout the

experiment. Pores with volumes  $\geq 1000$  and  $\leq 20000$  voxels consistently appear at  $t = 910$  (10\_880) which is equivalently one timestep earlier than Experiment 30\_880. This suggests that larger pores are appearing earlier in the 10 wt% crystal experiment.

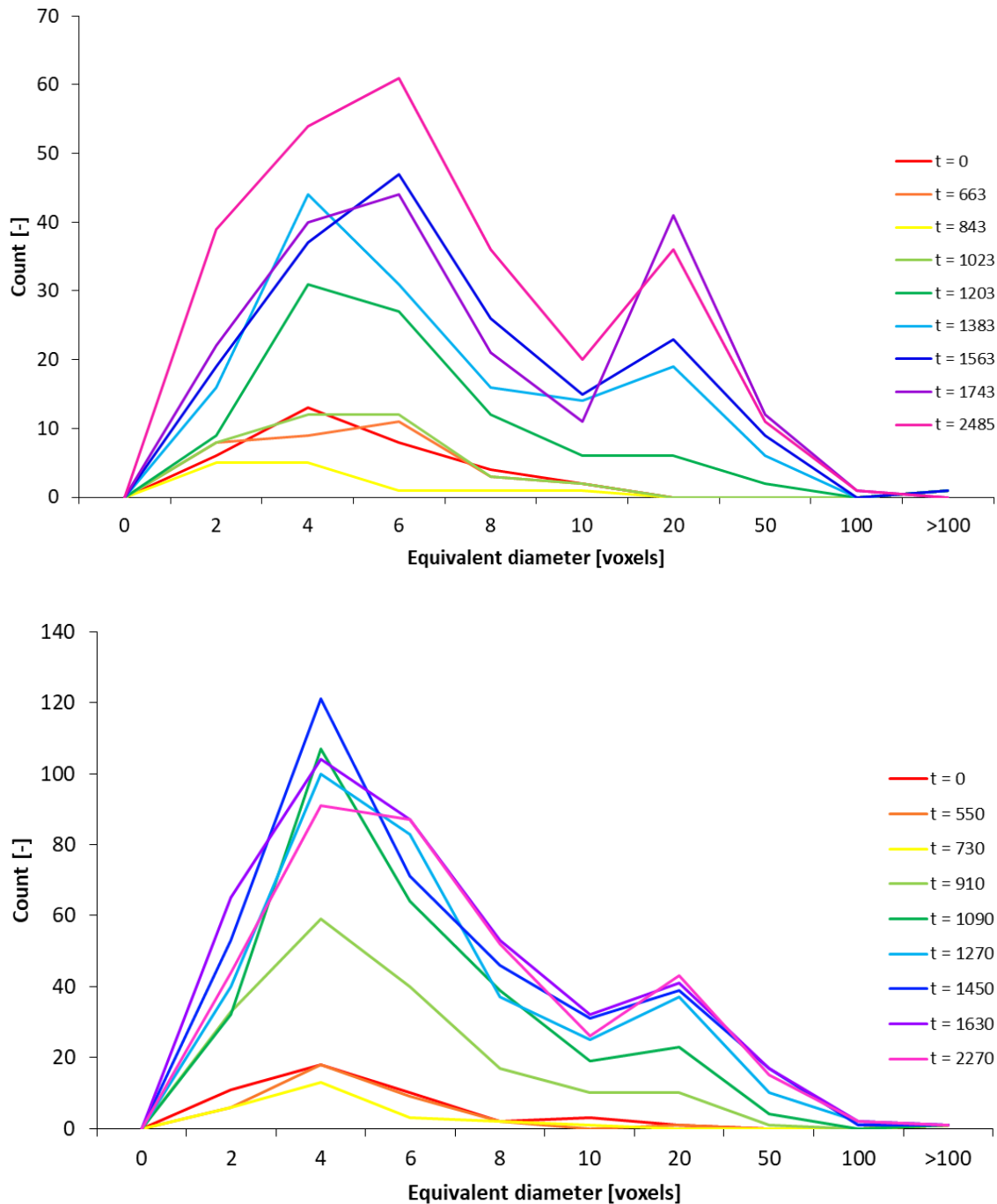


Figure 4.24: The distribution of equivalent diameters of pores from Experiment 10\_880 (top) and Experiment 30\_880 (bottom). The colours are equivalent timesteps between the experiment, e.g. the red line is the initial scan and the pink line is the final scan for both experiments, despite slightly differing times. The time is given in seconds.



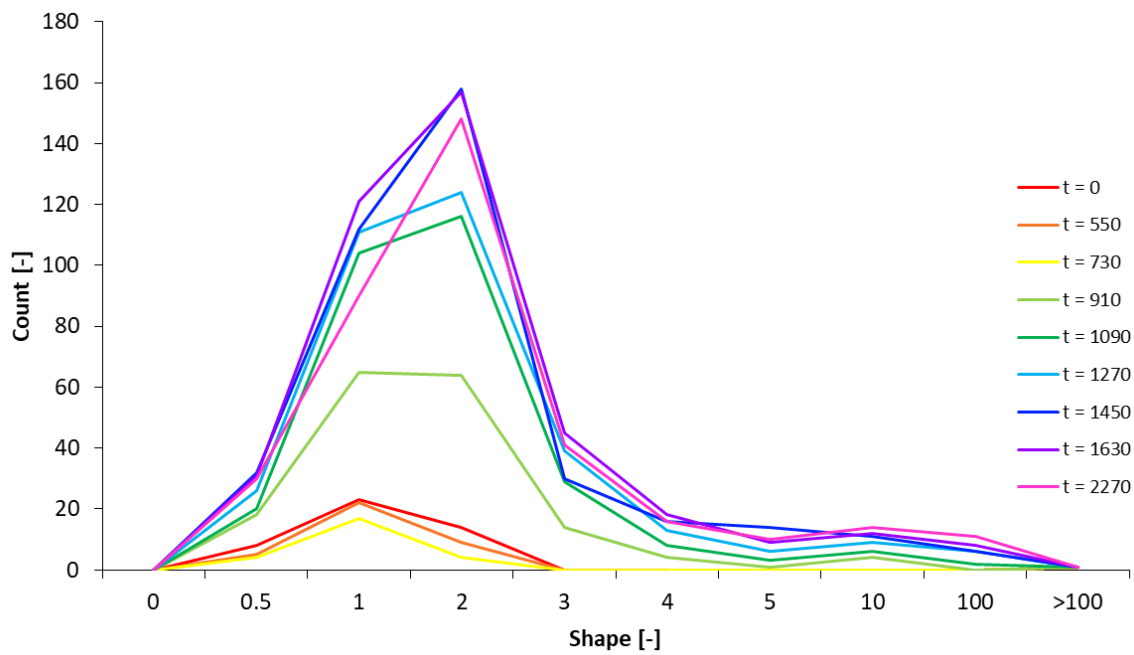
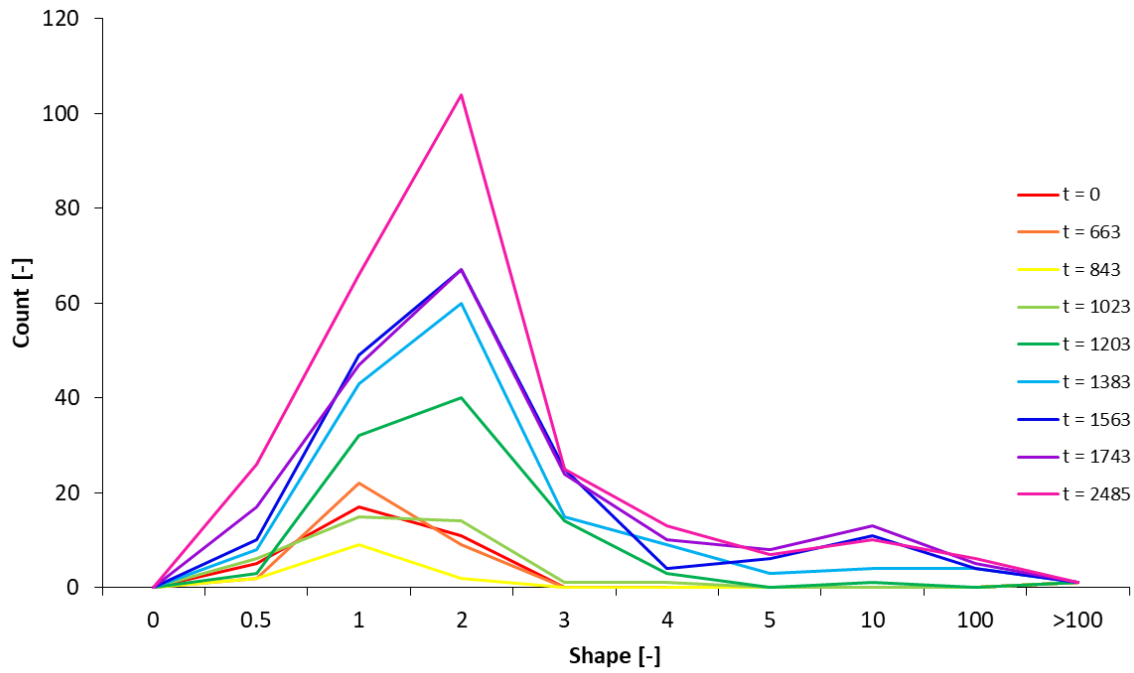


Figure 4.25: The distribution of shape factors of pores from Experiment 10\_880 (top) and Experiment 30\_880 (bottom). The colours are equivalent timesteps between the experiment, e.g. the red line is the initial scan and the pink line is the final scan for both experiments, despite slightly differing times. The time is given in seconds.

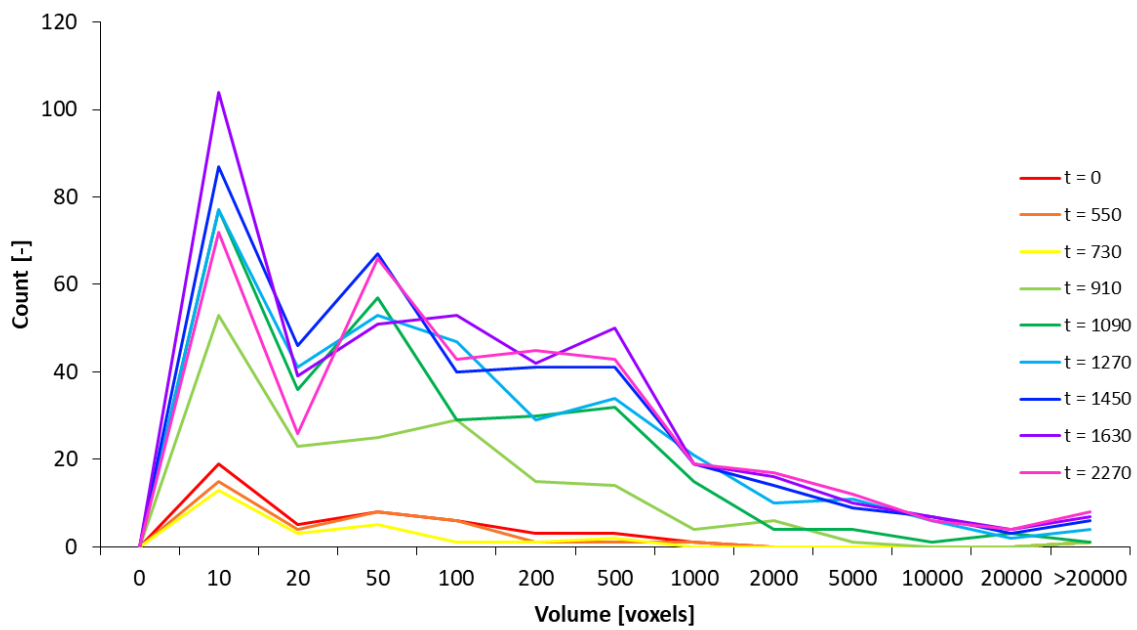
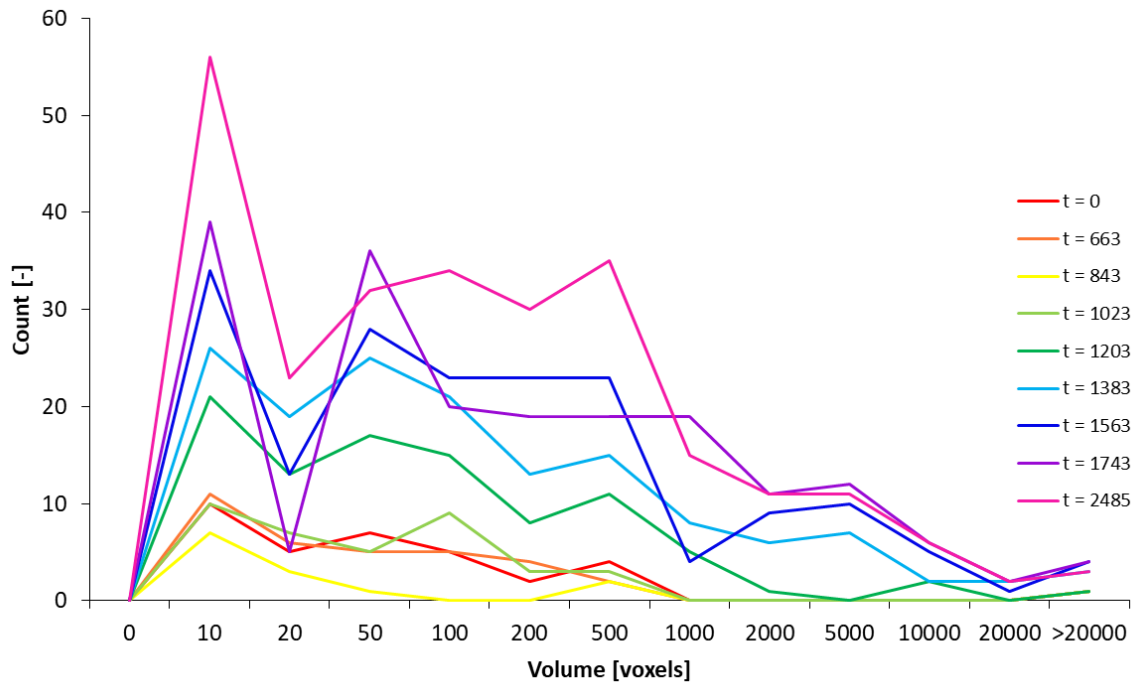


Figure 4.26: The distribution of pore volumes from Experiment 10\_880 (top) and Experiment 30\_880 (bottom). The colours are equivalent timesteps between the experiment, e.g. the red line is the initial scan and the pink line is the final scan for both experiments, despite slightly differing times. The time is given in seconds.

## 4.2 Volume fractions

The volume fractions of glass and crystal were obtained from the initial image of an experiment. The proportions of each as part of the solid fraction were compared against the volume fractions calculated with Equations 3.1 and 3.2, and mass fractions (Table 4.1). Experiment 20\_860\_polydisperse has been excluded as there are large errors associated with classification issues.

Experiment	155_00	162_00	186_00	166_00	180_00	171_00	174_00
<b>Total volume fraction – glass (gl)</b>	47.61	51.70	66.67	81.13	69.57	59.83	46.93
<b>Total volume fraction - crystal (xl)</b>	5.50	6.14	7.42	14.89	17.62	18.16	23.24
<b>Proportion of solid fraction - gl</b>	0.90	0.89	0.90	0.82	0.80	0.73	0.67
<b>Proportion of solid fraction - xl</b>	0.10	0.11	0.10	0.18	0.20	0.27	0.33
<b>Mass fraction – gl</b>	0.90	0.90	0.90	0.80	0.80	0.70	0.70
<b>Mass fraction – xl</b>	0.10	0.10	0.10	0.20	0.20	0.30	0.30
<b>Calculated volume fraction – gl</b>	0.9228	0.9228	0.9228	0.8416	0.8416	0.7560	0.7560
<b>Calculated volume fraction - xl</b>	0.0772	0.0772	0.0772	0.1584	0.1584	0.2440	0.2440

Table 4.1: The total volume fractions, the proportions of glass and crystal as part of the solid fraction, the calculated volume fractions, and the mass fractions of glass and crystal from initial images. Cells highlighted in blue are 10 wt% crystal content experiment, cells highlighted in orange are 20 wt% crystal content experiments, and cells highlighted in green are 30 wt% crystal content experiments. gl = glass. xl = crystal.

The volume fractions of glass are greater than the mass fraction, and the volume fractions of crystals are less than the mass fraction. The two calculations give similar values but there is a greater degree of error for solid fraction proportions as these values are based on machine learning software classification.

The volume fractions of xy slices were obtained to see how the proportions of phases changed through the z-axis between the start and end of an experiment. The volume fraction of phases is superimposed over an xz slice of 186\_36, a scan from the end of Experiment 10\_880 (Figure 4.27). There is a strong inverse relationship between glass and crystal; where there is less glass there is more crystal. Although not as clear, there also appears to be a general trend between crystal and pore; with a higher crystal volume fraction it is more likely that there is a higher pore volume fraction.

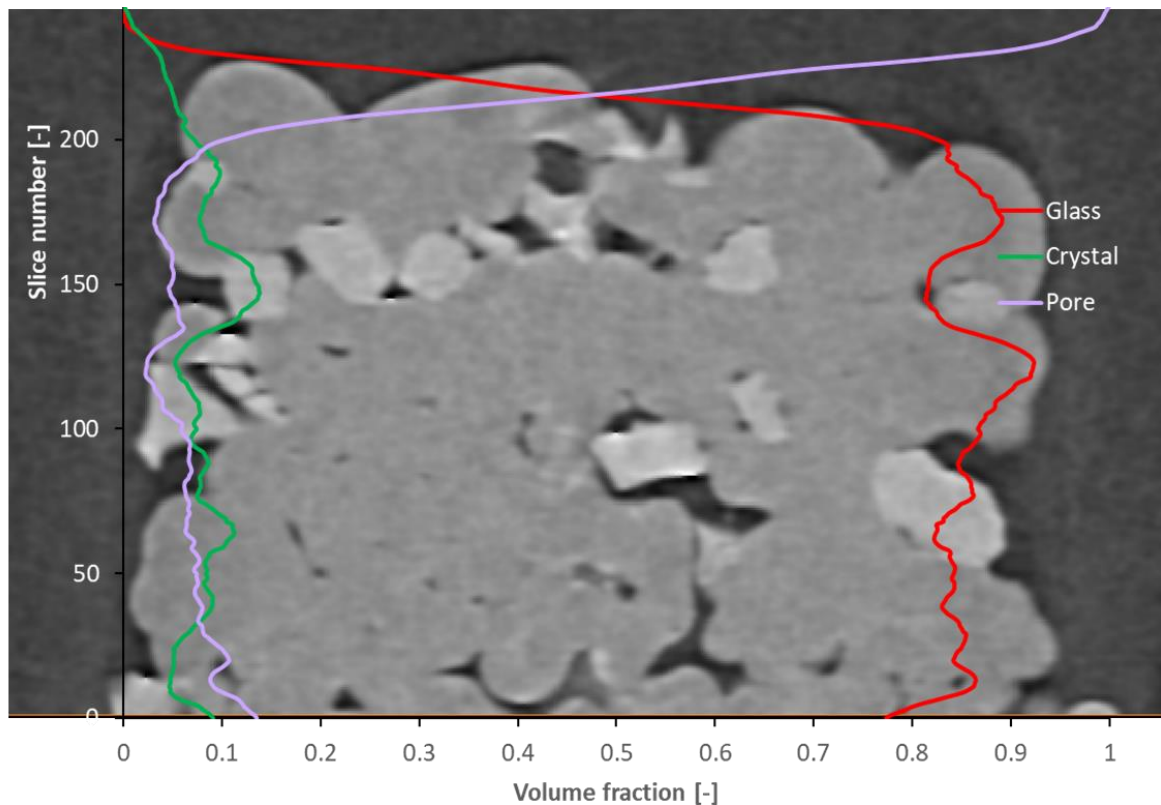


Figure 4.27: A slice through the z-axis of the sample from Experiment 10\_880 superimposed with the volume fraction graph. This shows how the volume fraction changes through the z-axis.

The volume fractions xy slices for the end of Experiments 10\_880, 30\_880, and 30\_860 are shown to illustrate the differences between a 10 wt% crystal experiment, a 30 wt% crystal experiment, and a 30 wt% crystal experiment where sintering was incomplete, respectively (Figure 4.28). There are greater changes in crystal volume fraction for 172\_00 (scan from end of 30\_880) than for 186\_36 (scan from end of 10\_880), and the relationship between pore and crystal is still evident; there is likely a higher pore volume fraction if the crystal volume fraction is greater. This relationship is not as well defined in 30\_880 compared to 10\_880. For 175\_36

(end scan from 30\_860), the pore volume fraction is greater than glass and crystal, sintering is incomplete. There is no discernible relationship between crystal and pore and the graph resembles much more closely volume fractions expected from an unsintered sample.

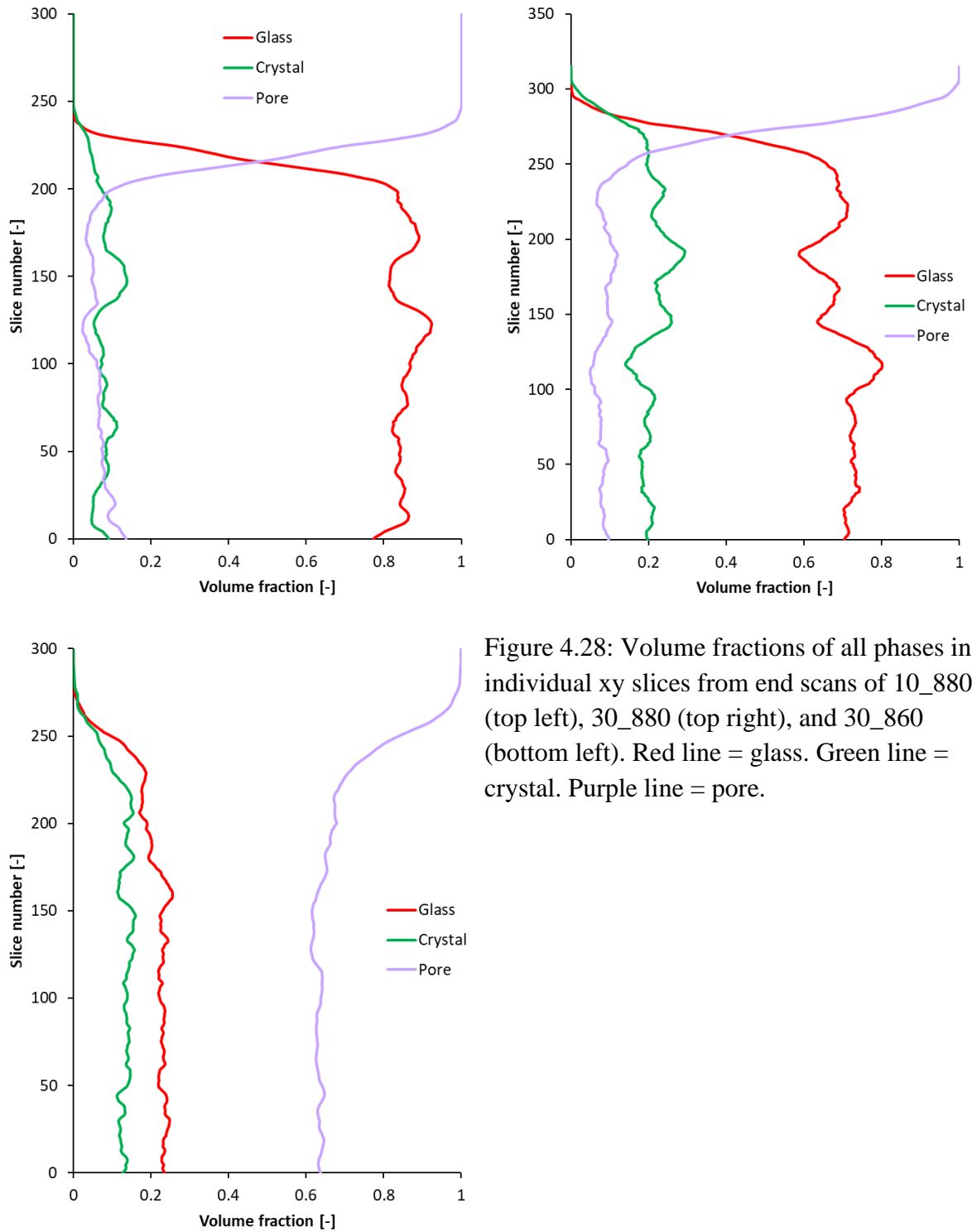


Figure 4.28: Volume fractions of all phases in individual xy slices from end scans of 10\_880 (top left), 30\_880 (top right), and 30\_860 (bottom left). Red line = glass. Green line = crystal. Purple line = pore.

### 4.3 Olivine analysis

The two crystal populations were compared using the parameters equivalent diameter, 3D shape, and aspect ratio.

The 90 to 180  $\mu\text{m}$  set (Population 1) is skewed left and shows a single modal peak around 210  $\mu\text{m}$ . The <90 and <250 set (Population 2) is skewed right and is bimodal with a strong peak at 20  $\mu\text{m}$  and wider spread peak at 160  $\mu\text{m}$  (Figure 4.29).

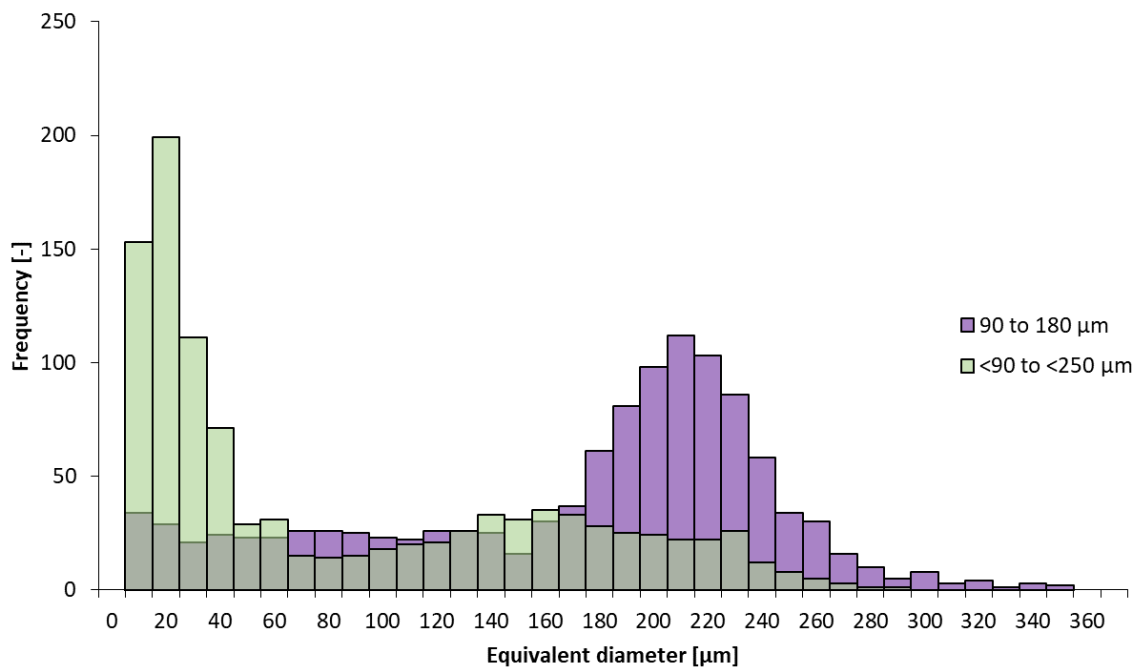


Figure 4.29: Equivalent spherical diameter of crystals from two differently distributed sets. Purple bars = 90 to 180  $\mu\text{m}$  (Population 1). Green bars = <90 to <250  $\mu\text{m}$  (Population 2).

The modal shape factor of the Population 1 crystals is  $\sim 3$  (Figure 4.30). Shapes similar to the blue and green shape insets in Figure 4.30 are what a typical crystal would look like, with fewer having a blade-like characteristic of the red inset. For Population 2, the modal shape factor is  $\sim 1$  which is likely caused by the small particle sizes even if the particle is not necessarily spherical.

The spread of aspect ratios for both crystal populations is quite similar with the modal peaks between 2 and 3 (Figure 4.31). This means the crystals are elongated rather than spherical, with a typical crystal 2-3 times longer than wide. The distribution is slightly skewed right indicating that the particles are more likely to be elongate than not. Population 2 has a second modal peak at  $\sim 1$  which is likely a bias because of the small size of crystals.

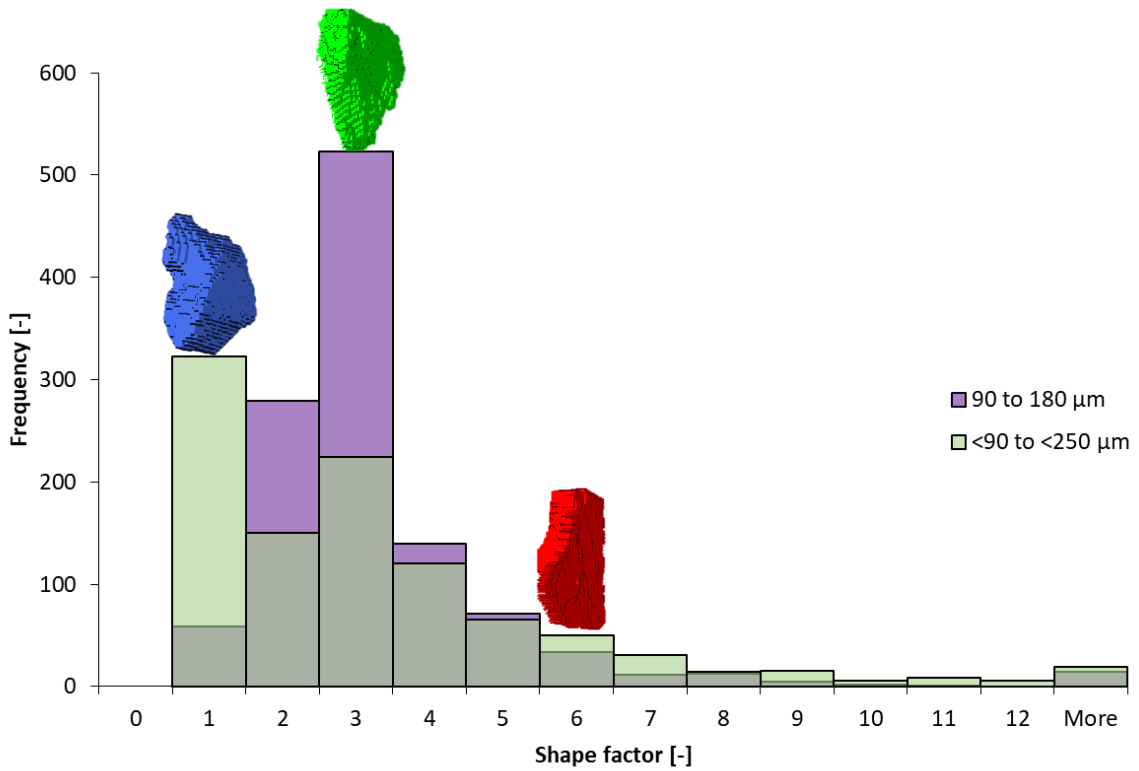


Figure 4.30: Shape factors of the different crystal sets. The blue shape inset represents a crystal with a shape factor of 1.8, the green shape inset that of 3.6, and the red inset a factor of 6.6. Purple bars = 90 to 180 μm set. Green bars = <90 to <250 μm set. Note how the crystal tends towards a greater difference between dimensions with increasing shape factor.

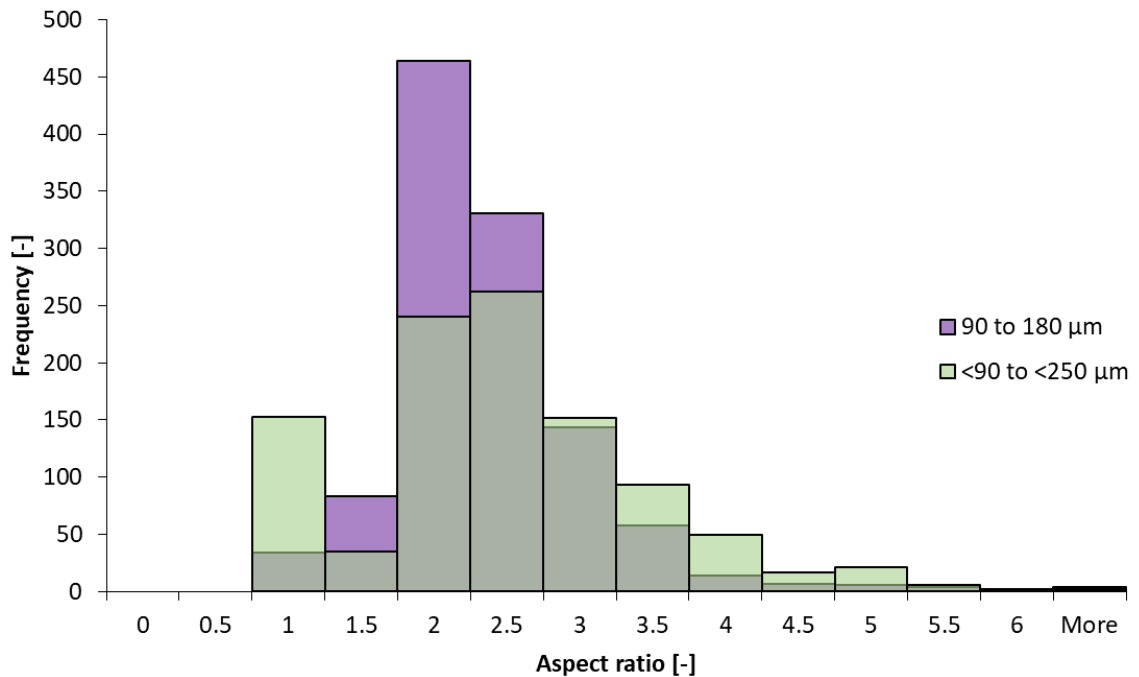


Figure 4.31: The range of aspect ratios for the different crystal populations. Purple bars = 90 to 180 μm set. Green bars = <90 to <250 μm set.

### 4.3.1 Crystal interfaces

For the samples that fully sintered or were very close to it, the materials that crystal particles were in contact with were obtained and quantified. The two contact types included here are crystal-pore and crystal-glass. The varying amounts are compared for the high dwell temperature experiment starts and ends, and crystal contents 10, 20, and 30 wt% (Figure 4.32). At the start of each experiment, crystal-pore contacts were greatest, but by the end of experiments, were least (with the exception of Experiment 10\_880). In comparison, the proportion of crystal-glass contacts starts low for all experiments and increase by the experiment end. The data suggest that greater crystal content results in higher values at the start and end of experiments for all contacts. In addition, the proportion of crystal in contact with glass increases during the experiment, and the proportion of crystal in contact with pore decreases, regardless of crystal content.

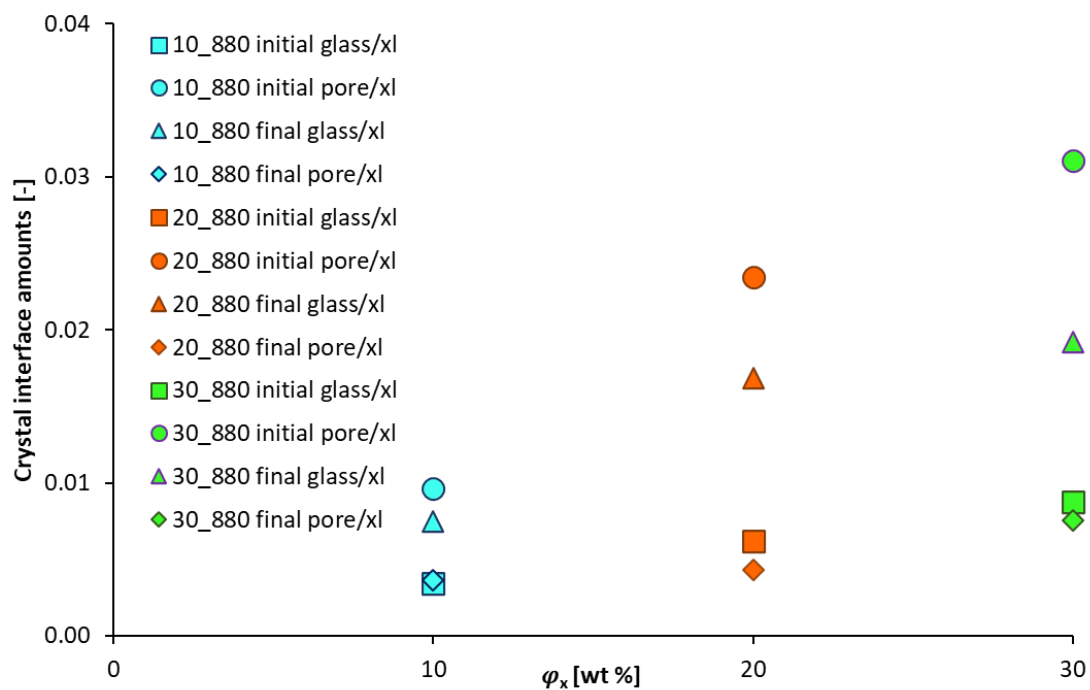


Figure 4.32: Amount of contact between crystal and glass, and crystal and pore, at the start and end of experiments 10\_880, 20\_880, and 30\_880. Blue symbols = 10 wt% crystal. Orange symbols = 20 wt% crystal. Green = 30 wt% crystal. Square = initial crystal-glass contact. Circle = initial crystal-pore contact. Triangle = final crystal-glass contact. Diamond = final crystal-pore contact.



## 4.4 DVC

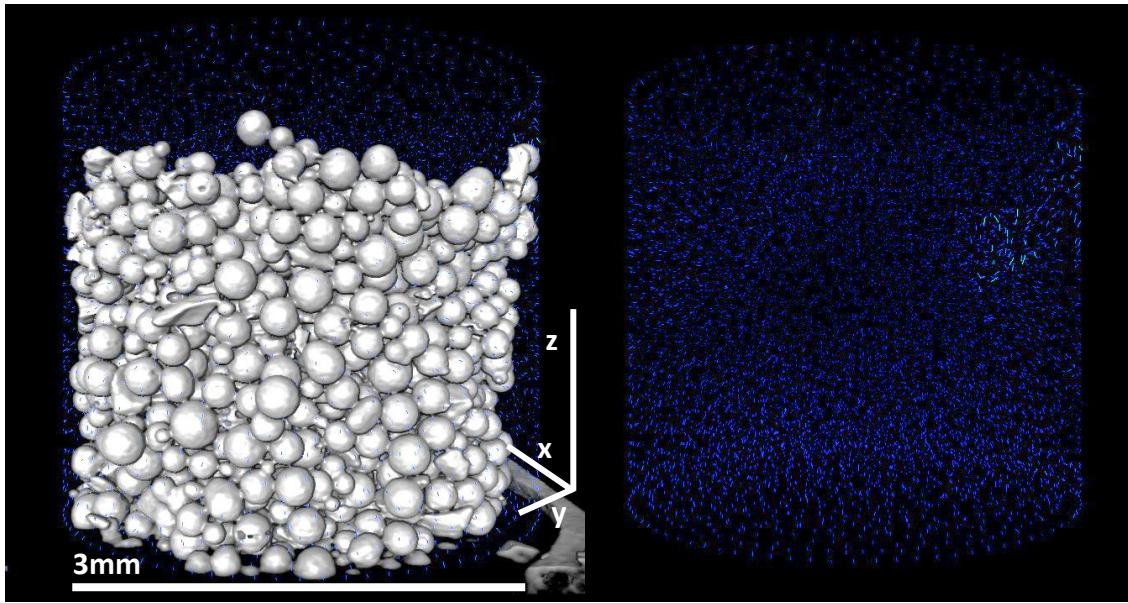
DVC was used to track the direction and magnitude of displacement of particles between various timesteps in experiments. All of the magnitudes are set to the same scale of 0-50 so displacement can be qualitatively assessed between experiments. The scans and times used for the displacement vector fields and times are in Appendix Table 5.

### 4.4.1 Experiment 10\_880

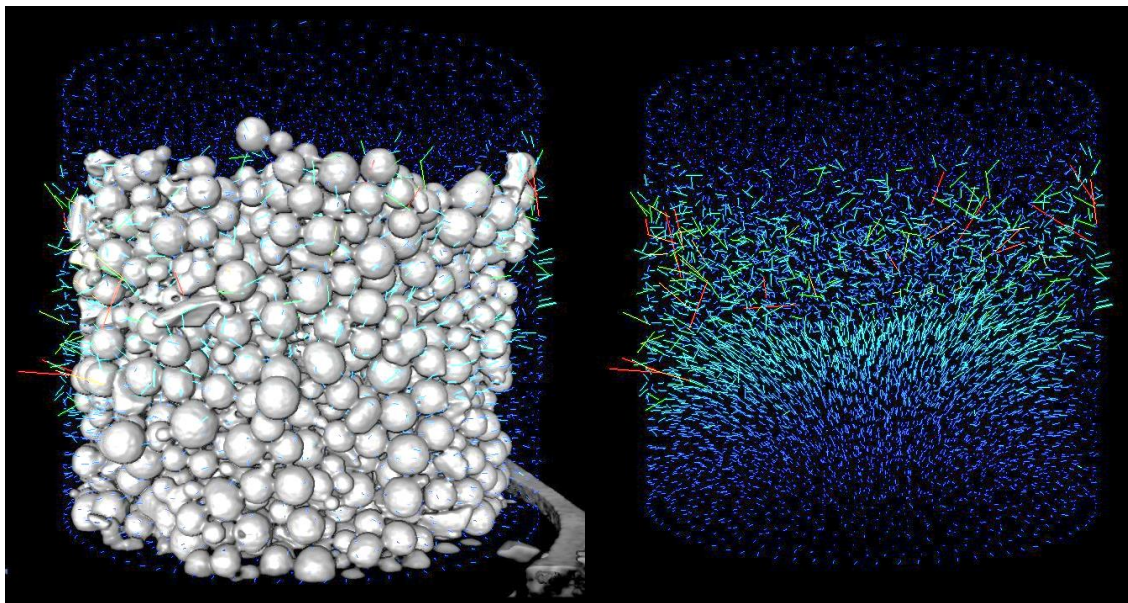
This 10 wt% crystal content experiment was almost fully sintered. The displacement between timesteps is shown as vector fields (Figure 4.33).

In VF1, there is essentially no displacement. The small patch of displacement is likely due to the slight shift of a glass bead. Next, in VF2, major displacement occurs from the top until approximately halfway down the sample. The general direction of vectors points towards the centre and slightly towards the base. Displacement is greatest near the top, with average values around 200  $\mu\text{m}$ , decreasing to  $\sim 70$   $\mu\text{m}$  towards the middle which decreases again to 0 at the base. In VF3, displacement is occurring throughout more of the sample, and the displacement is generally greater than the previous vector field. The direction of vectors is still towards the centre and slightly angled towards the base of the sample. Next, in VF4, the magnitude of displacement is slightly lower, but the direction has changed to pointing towards the base as the whole sample shrinks down. Displacement decreases to lower values of around 70  $\mu\text{m}$  by the next vector field, with direction mostly pointing towards the sample base. Finally, in VF5 and VF6, displacement is between 0 and 50  $\mu\text{m}$  with final vector directions pointing towards the base. This indicates that there is a radial shrinkage aspect of the sample earlier in the experiment before the sample shrinks down.

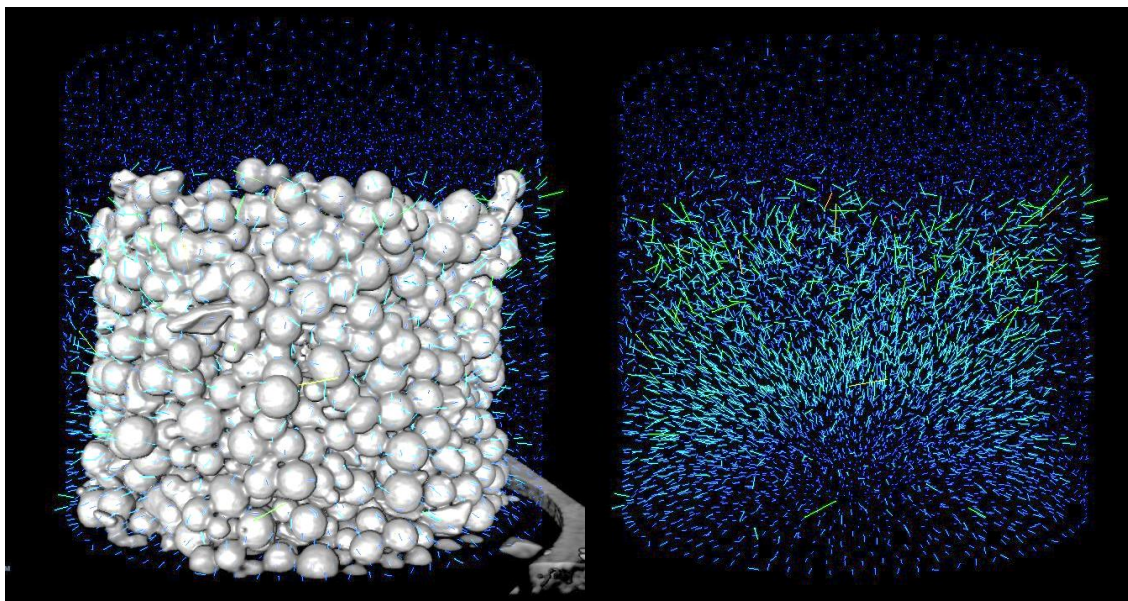
There are no isolated patches of great displacement that would indicate that olivine crystals are sinking on the timescale of these experiments.



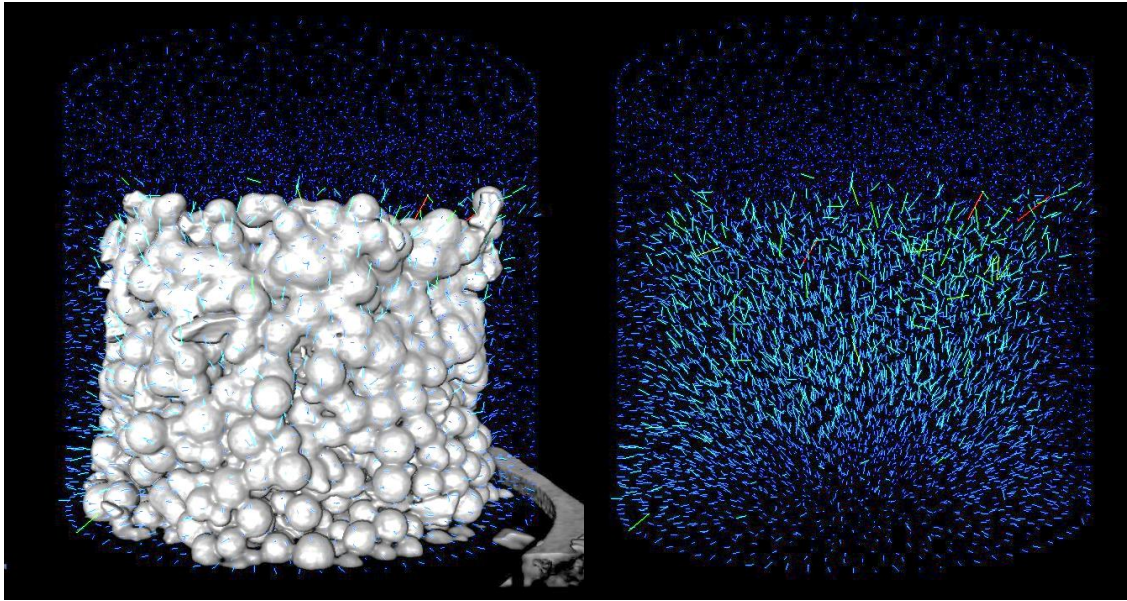
VF1



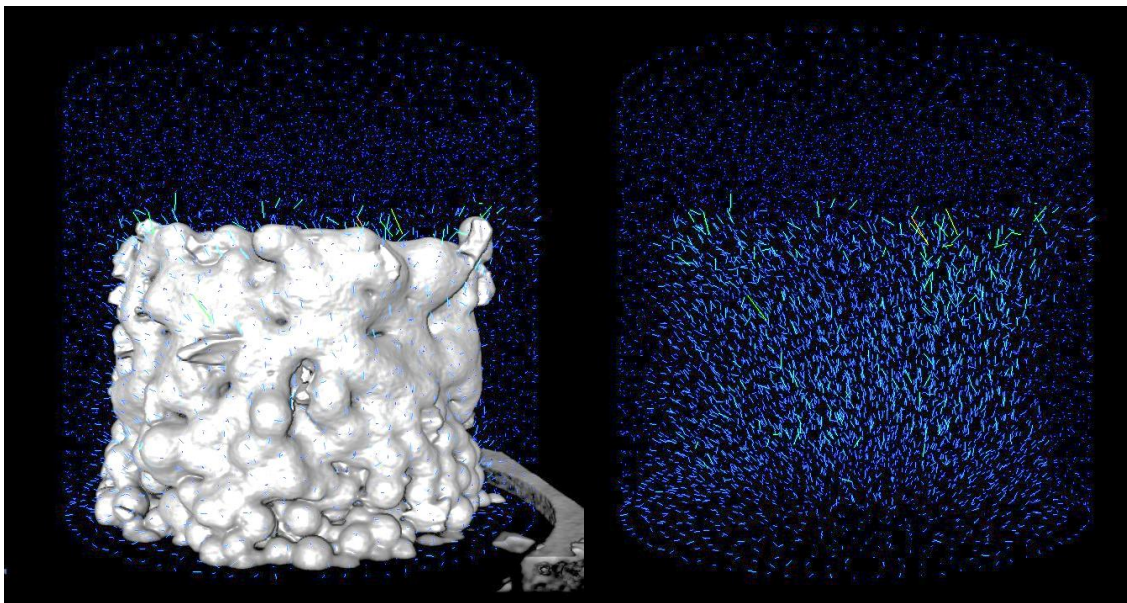
VF2



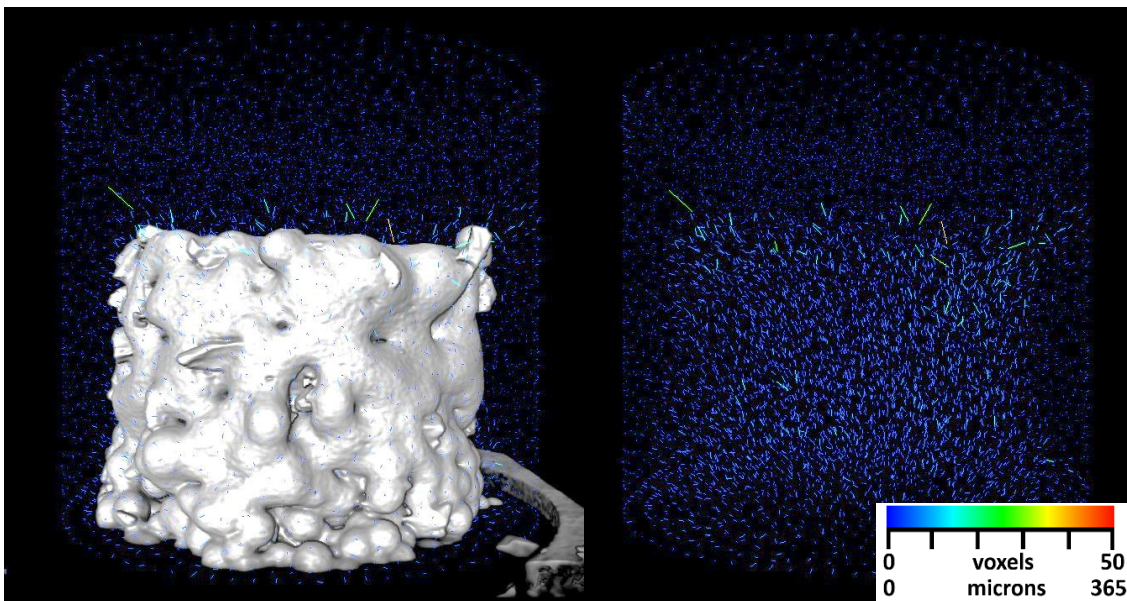
VF3



VF4



VF5



VF6

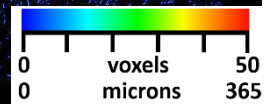


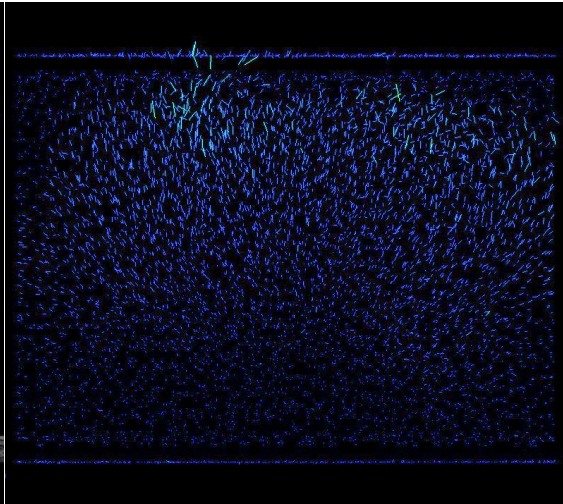
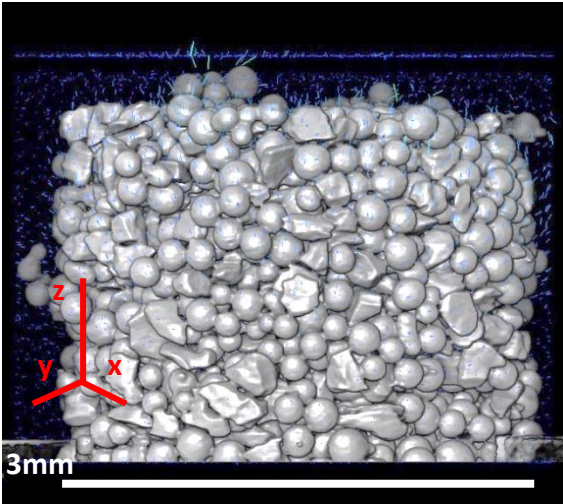
Figure 4.33: 3D renders of the 10\_880 sample during sintering, showing the change in displacement through time (left) and solely the displacement vector fields (left). The vectors display the magnitude of displacement using the colour scale. Orientation and scale of all images identical throughout

#### 4.4.2 Experiment 30\_860

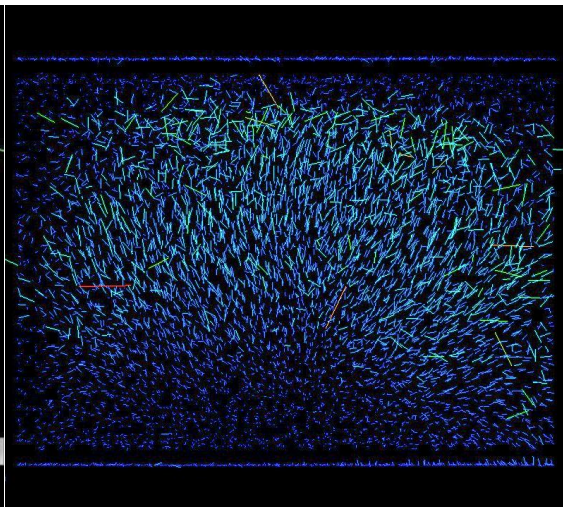
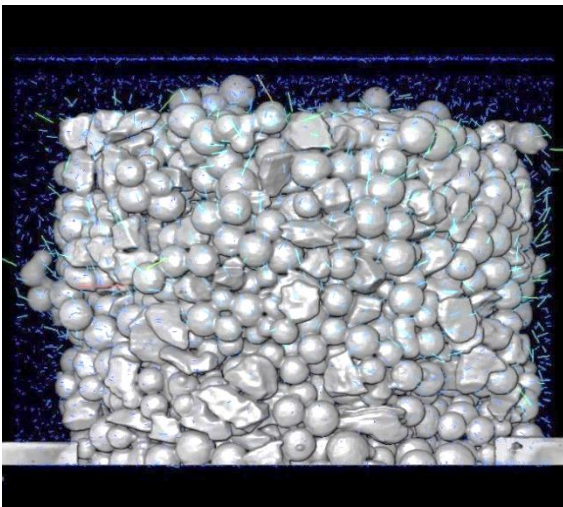
Sintering is incomplete in this 30 wt% crystal content experiment (30\_860). The displacement between timesteps is shown as vector fields (Figure 4.34).

Compared to 10\_880, the vector field for this incompletely sintered experiment looks very different. The magnitude of displacement is not as great as that in the more sintered samples at any given time. The direction of the vectors is mostly pointed towards the base, and only more towards the centre in VF14 (Figure 4.34).

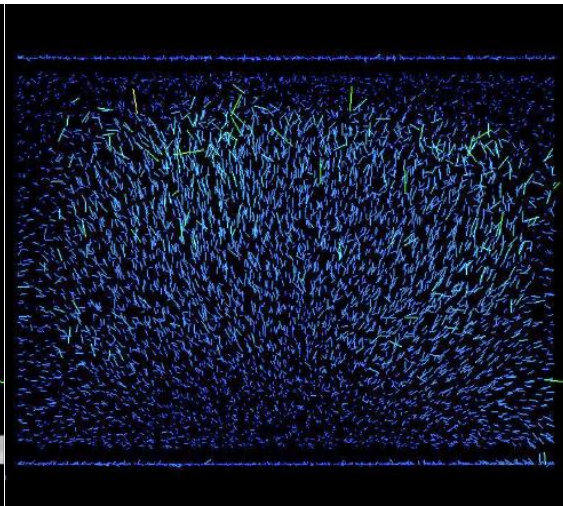
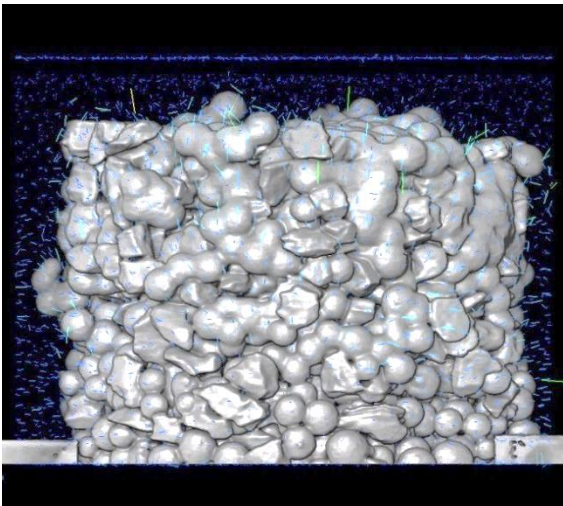
In VF7, there is essentially no displacement with only a small patch likely caused by the shifting of a particle. Next, in VF8, the largest displacement is focussed around the edges of the sample, and displacement is evident in approximately the top three quarters of the sample. The vectors at the edges point towards the centre of the sample and slightly towards the base, whilst vectors towards the middle point towards the centre of the base. Displacement is greatest near the edges with average values of  $\sim 200 \mu\text{m}$  and decreasing to  $\sim 70 \mu\text{m}$  towards the middle which decreases again to 0 at the base. In VF9, displacement is evident in the majority of the sample, but displacement is generally a lower magnitude than VF8. Most vectors indicate movement of  $\sim 100 \mu\text{m}$ . The direction of vectors is towards the base, with some focussing more towards the base centre. Next, in VF10, the magnitude of displacement decreases again to values of  $\sim 50\text{-}100 \mu\text{m}$  typically. Most vectors point towards the base, but the bottom quarter of vectors point towards the sample centre. There is little to no displacement through much of the sample in VF11 and VF12 with displacements of close to  $0 \mu\text{m}$ . The prominent vector direction is towards the sample base. This indicates that the general direction of sample displacement is down throughout the experiment as the sample shrinks down.



VF7



VF8



VF9

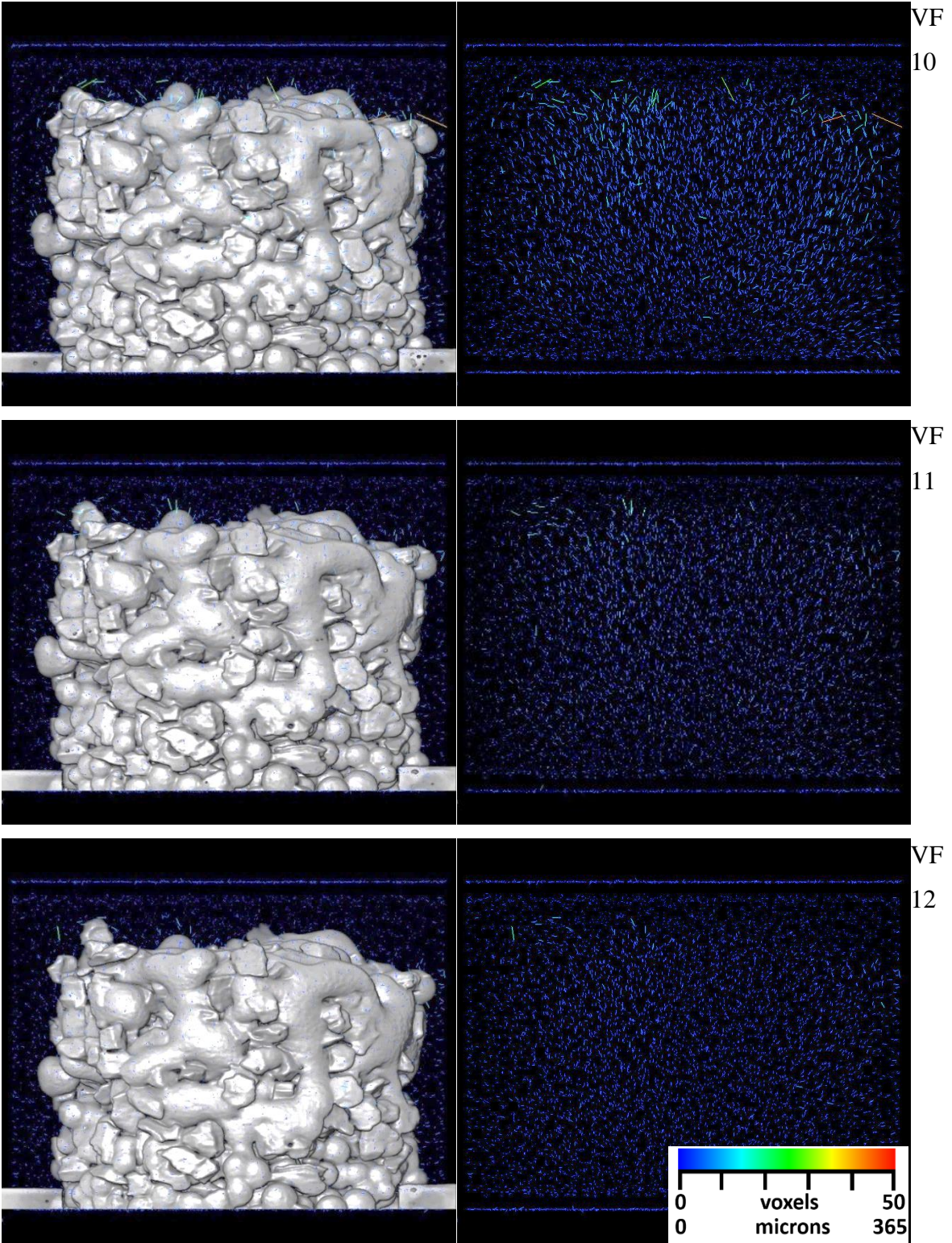


Figure 4.34: 3D renders of the 30\_860 sample during sintering, showing the change in displacement through time (left) and solely the displacement vector fields (left). The vectors display the magnitude of displacement using the colour scale. Orientation and scale of all images identical throughout.

## 5. Discussion

### 5.1 Discussion of results

In this section, the results are discussed in detail as well as experiment procedure and imaging.

#### 5.1.1 Overall, disconnected, and final porosities

The main products of these experiments are the porosity results, both overall and disconnected. For the overall porosity, this decreases as the experiment continues which is mimicked across all experiments despite differing conditions and crystal content. In this work, a sample was considered fully sintered if there was a smooth curve of porosity data that plateaued before the end of the main gapped scan, the values of the final and penultimate results were the same, and if the overall and disconnected porosity values met. Only Experiment 20\_880 met these criteria but Experiments 10\_880 and 30\_880 were close. All three were run at the highest temperatures, and so are grouped together as the High Dwell Temperature Group (HDT Group) for the discussions, representing the near fully sintered experiments. These display a clear shape similar to that from previous work (Eberstein et al., 2009; Amoros et al., 2019) and this occurs because the samples have almost fully sintered, and the pore space is near equilibrium. This relationship is not as clear to see in other experiments, because they have achieved a lesser degree of sintering, but is still present. The crystal content appears to have little effect on the overall results with only the final values of more sintered samples showing any effect.

In order to obtain porosity results, cuboid subvolume extracts were used. To see if using these subvolume extracts would be representative of the sample as a whole, two different sized subvolumes were used. The values between subvolumes should be similar if they are completely representative. However, there was almost always a difference in overall porosity values. This indicated that sintering was not occurring at the same rate throughout the entire sample and a degree of anisotropy was being introduced. The greatest differences between values were seen in the incompletely sintered experiments, and conversely, the smallest differences in the near fully sintered HDT Group experiments. The smaller extracts were located towards the middle and top of samples and porosity results of these small extracts from the HDT Group show that they were fully sintered. This, along with the 3D renders, indicate that sintering occurs first towards the top of samples and finishes sintering sooner than the base.

This is evident in Figure 5.1 where the yz orientated slice of a sample displays a greater degree of sintering at the top than at the base.

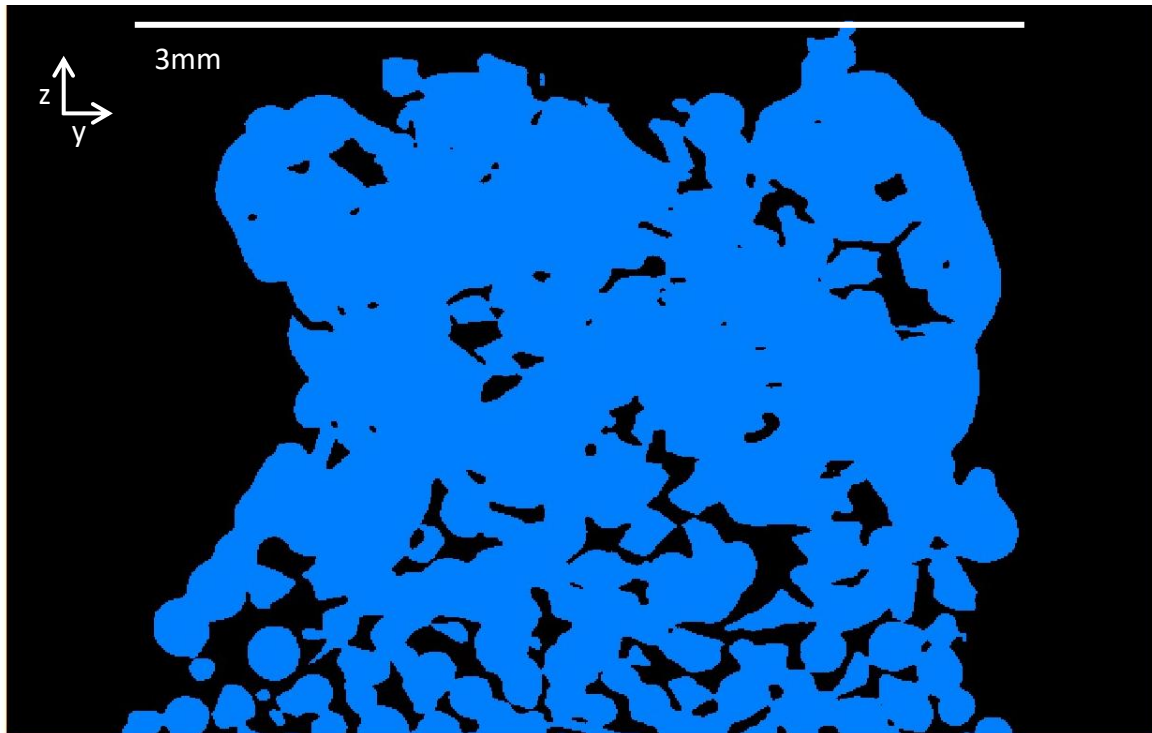


Figure 5.1: Difference in degree of sintering within a sample. The outlines of individual particles are still visible at the base indicating a lower degree of sintering than at the top.

The cause of this effect is the sample holder and spindle it is placed upon. They are both situated within the furnace, but the spindle extends outside, allowing drawdown of heat as it acts as a heat sink. The temperature held in the furnace and that held within the sample are different. The lower sample temperature results in slower sintering rates.

The definition of disconnected porosity in this work are pores that did not connect through the subvolume in any direction and is meant to represent the general changes in connection through sintering.

In general, the disconnected porosity increases from an initial value of 0, where the entire pore network is connected, to greater values as the experiment progresses, where the sintering glass begins to isolate sections of the pore network. For a fully sintered sample, disconnected porosity should be the only porosity remaining as the network is no longer connected. Once the disconnected porosity and overall porosity have the same value, there is no connection of the pore network through any axes, and the pore network is no longer open. The appearance of disconnected porosity is linked to degree of sintering which is in turn linked to temperature.



For the HDT Group, disconnected porosity appears ~500 seconds after the start of the main gapped scan and the dwell temperature is reached. The crystal content does not have a notable effect but may do if more scans were reconstructed before the disconnected value increased. The dwell temperature of the Medium Dwell Temperature Group (MDT Group) was 20°C lower (860°C), resulting in a reduced sintering rate, and a later appearance of disconnected porosity.

In Figure 4.4 (10\_860\_longrun), the image shows the porosity network change from connected to disconnected. The pore forms a ‘bottle neck’ shape in the connected image, which is gone in the disconnected image, shut off as the glass further sinters (Figure 5.2)

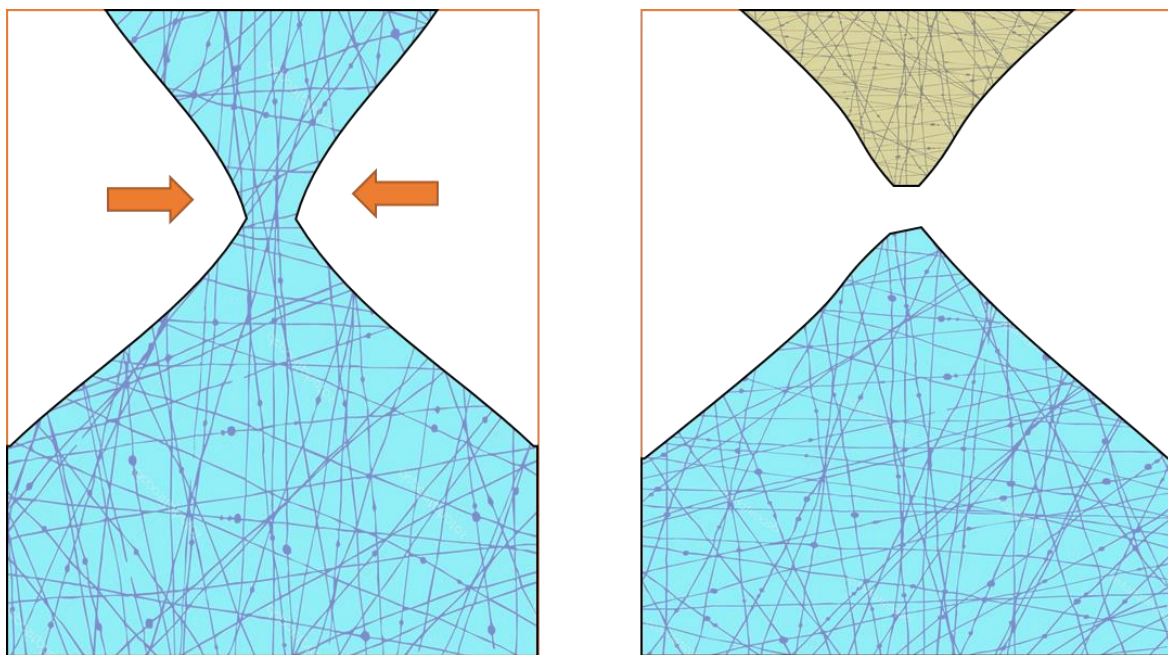


Figure 5.2: Simplified schematic of the pore network shape in Figure 4.4 before (left;  $t = 1760$ ) and after (right;  $t = 2575$ ) the neck thinned enough to disconnect the two sections of pore.

This is also seen in Figure 4.9 (20\_880) when the first image shows the majority of the network still connected but disconnected through the z-axis due to a pinch in the shape near the top of the pore network. Therefore, the formation of ‘neck’ shapes by the glass sintering is likely the main way in which smaller sections of pore space become separated from the network.

None of these disconnected porosity results are easily comparable to previous experiments such as Eberstein et al (2009) and Amoros et al (2019) because this work looks at disconnected porosity, not isolated porosity. In addition, previous work has estimated the porosity from shrinkage and density which are relative until calibrated with SEM scans. This is inherently

biased as a 2D section is unlikely to be representative of a 3D sample (e.g. Van Dalen and Koster, 2012).

Where crystals do have a notable effect is on the final values of near fully sintered samples; when the crystal content increases, the final porosity also increases. This relationship is evident as long as samples of equivalent sintering degree or samples run under the same experiment conditions are compared as in Figure 4.19, where the results from HDT Group samples are shown.

The final total porosity results from the most sintered samples are compared to previous work (Figure 5.3). All of the data fit the trend of increasing crystal content resulting in increased final porosity.

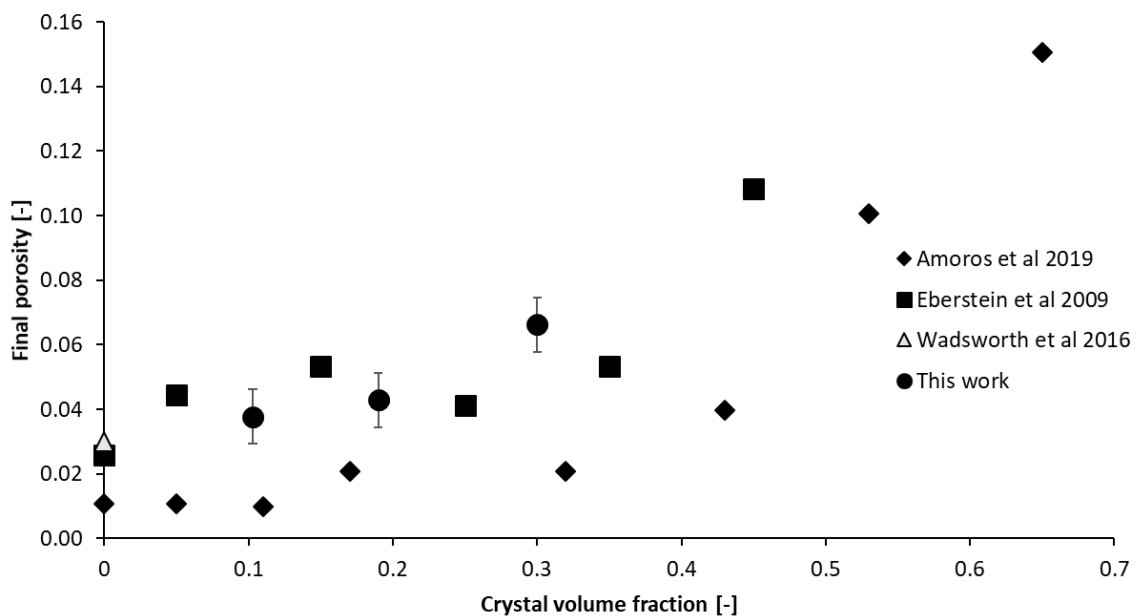


Figure 5.3: Final porosity values from sintering experiments with different crystal volume fractions compared to this work. Diamond = Amoros et al., 2019 data. Square = Eberstein et al., 2009 data. Triangle = Wadsworth et al., 2016 data. Circle = this work.

Experiments 10\_860, 20\_860, 20\_860\_polydisperse, and 30\_860 were held at the same maximum dwell temperature of 860°C and so are grouped together as the MDT Group for the purpose of discussions. Experiment 10\_860\_longrun is dissimilar as the sample was held at multiple increasing dwell temperatures and ran for almost 4 times as long as other experiments. The final porosity values are plotted, with the HDT Group picked out as circles, and everything but the blue square as part of the MDT Group (Figure 4.20). The MDT Group samples were incompletely sintered but still show larger final porosity values with more crystals. The

difference in final porosity values between the differing crystal content experiments in the MDT Group are greater than in the HDT Group, indicating the sintering is slower with more crystals.

None of the values are at equilibrium, bar Experiment 20\_880, with the HDT Group closest to equilibrium, and the MDT Group not close to equilibrium at all.

### **5.1.2 Normalised data**

The experiments were run under differing conditions and times and run differently to previous work such as Eberstein et al (2009) and Amoros et al (2019). Therefore, to compare the results, they were normalized to a common factor. Wadsworth et al (2016) provide validated models of sintering monodisperse and polydisperse populations. The experimental data of this work was plotted alongside the models. The results should fall onto one of the model lines and for this work, the shape of the curve best fits that of a monodisperse population.

Figure 4.21 illustrates the discrepancy between model and data that is corrected by adjusting the temperature. There is a difference between the input temperature, the temperature held in the furnace, and the temperature of the sample. Calibration against a crystal-free sintering sample is preferable but without this option, the 10 wt% crystal experiments were used as calibration. The residual sum of squares was smallest at temperatures of approximately  $-106^{\circ}\text{C}$  which is what the data is corrected by. The higher crystal content experiments appear to be overcorrected. There is likely another parameter that needs adjusting for future work where crystals are included in a sintering mix.

Another parameter considered and calculated was the pore size. The particle size distribution of the glass beads (from Vasseur et al., 2013) was entered into the editable Excel® sheet from Wadsworth et al (2019) and used to solve the welding code for isothermal or non-isothermal conditions, including for polydisperse particles (or droplets). Particle size distribution affects the dispersion of particles. Particles of the same size make up a monodisperse system and a relatively large pore size, and particles with a range of sizes make up a polydisperse system and a relatively smaller pore size as smaller particles fill some of the space (Figure 5.4).

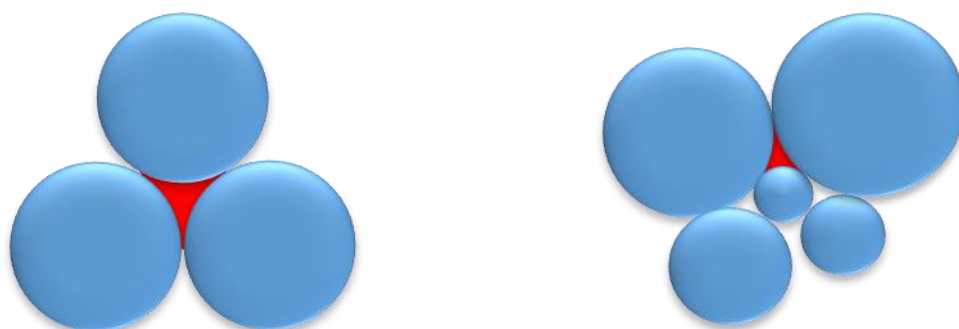


Figure 5.4: Schematic illustrating the relative difference in pore size between a monodisperse population (left) and polydisperse population (right).

As the code is geared towards polydisperse systems, a correction factor is calculated and applied to the calculated pore size if the system of particles is more monodisperse.

The offset is corrected, and data plotted in Figure 4.22, which showcases the difference produced between the two viscosity equations. The first graph uses the glass viscosity and shows more scatter at the beginning but mostly falls on the monodisperse model line. There is a small deviation at the end of Experiments 20\_880 and 30\_880 which may be due to the presence of crystals. The second graph uses the viscosity of glass with differing proportions of suspended particles. This, in theory, should allow the effects of the crystals alone to be apparent. This can be seen with the data from Eberstein et al (2009) where the data collapses on to one line, with deviations caused by increasing crystal content (Figure 5.5). However, when compared to the Eberstein data, the normalized porosity results from this work have not collapsed on to a single line, and there is much more scatter (Figure 5.6). This is likely due to the necessity of individual temperature corrections for each experiment, based on correcting for the temperature of the sample.

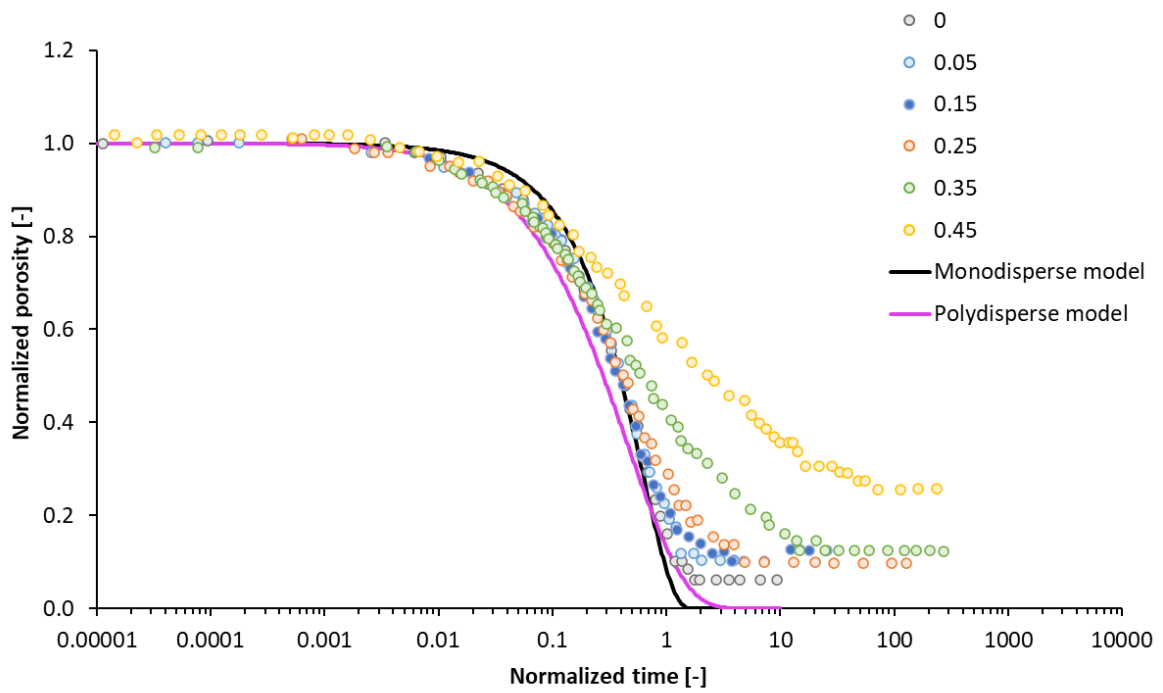
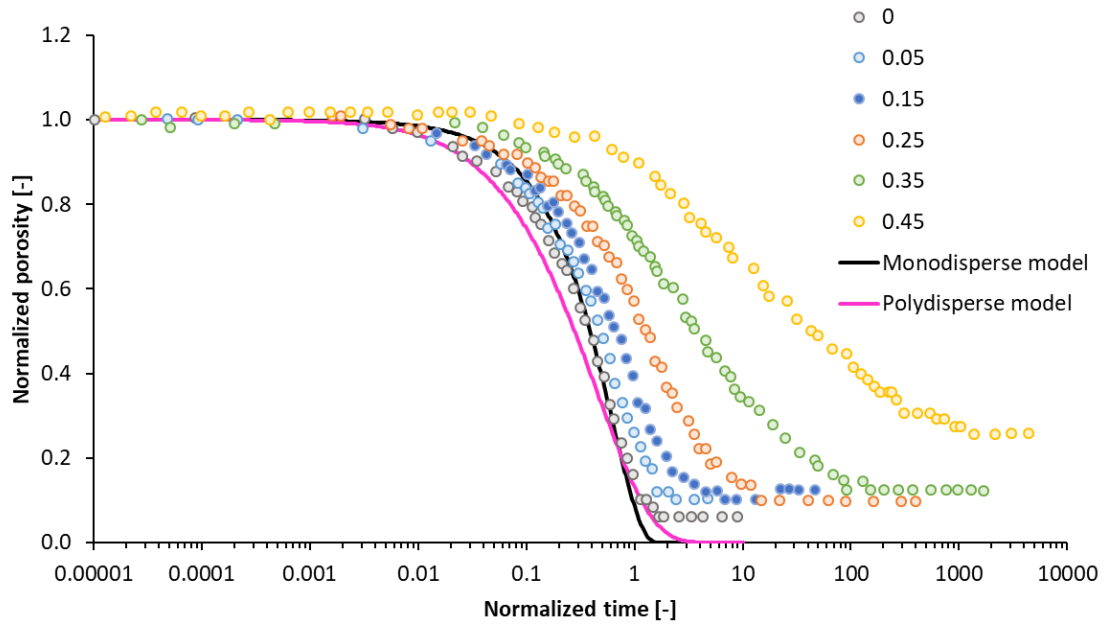


Figure 5.5: Normalized porosity data from various rigid inclusion fraction experiments from Eberstein et al (2009) using glass viscosity (top) and viscosity with suspended particles (bottom). Grey = no crystals. Light blue = 0.05 rigid inclusion fraction. Dark blue = 0.15 rigid inclusion fraction. Orange = 0.25 rigid inclusion fraction. Green = 0.35 rigid inclusion fraction. Yellow = 0.45 rigid inclusion fraction. Black line = monodisperse model. Pink line = polydisperse model.

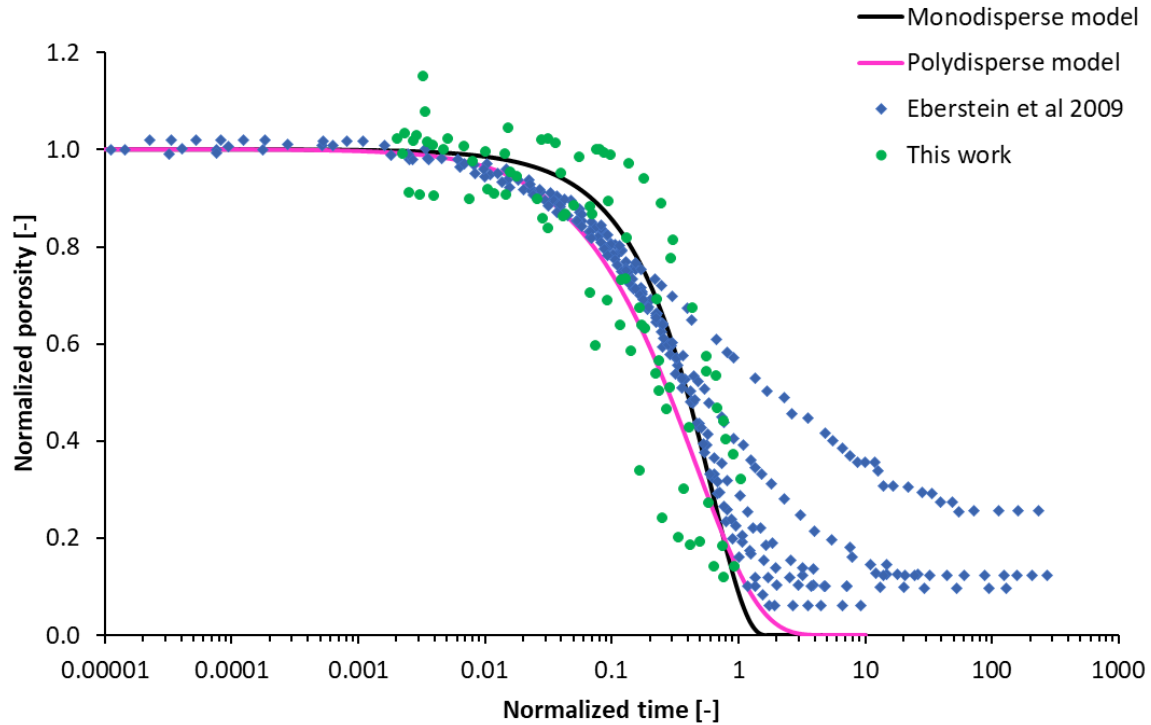


Figure 5.6: Normalized porosity data calculated using viscosity with suspended particles from Eberstein et al (2009) and this work. Black line = monodisperse model. Pink line = polydisperse model. Diamond = Eberstein et al (2009). Circle = this work.

### 5.1.3 Connectivity

The connectivity of samples is obtained at multiple time points across all experiments and are plotted with data collated in Colombier et al (2017; Figure 5.7). The results from this work fall within expected results of natural welded deposits but do not overlap with sintered glass data, showing greater connectivity maintained at lower porosities. Additionally, the higher crystal content experiments show the drop in connectivity being shifted towards lower porosities, indicating that crystals are the cause of the extended retention of connectivity. From this work, only the results of Experiment 20\_880 reached a connectivity of 0 at a porosity of  $\sim 0.05$ , which is echoed by results in Colombier et al (2017). Had the experiments reached equilibrium, I would expect the final porosity to be higher at  $C = 0$  for the 30 wt% crystal content experiments, and lower or the same for the 10 wt% crystal content experiments.

These values are artificial because of the use of subvolumes to remove edge effects, but they are generally representative of the whole sample.

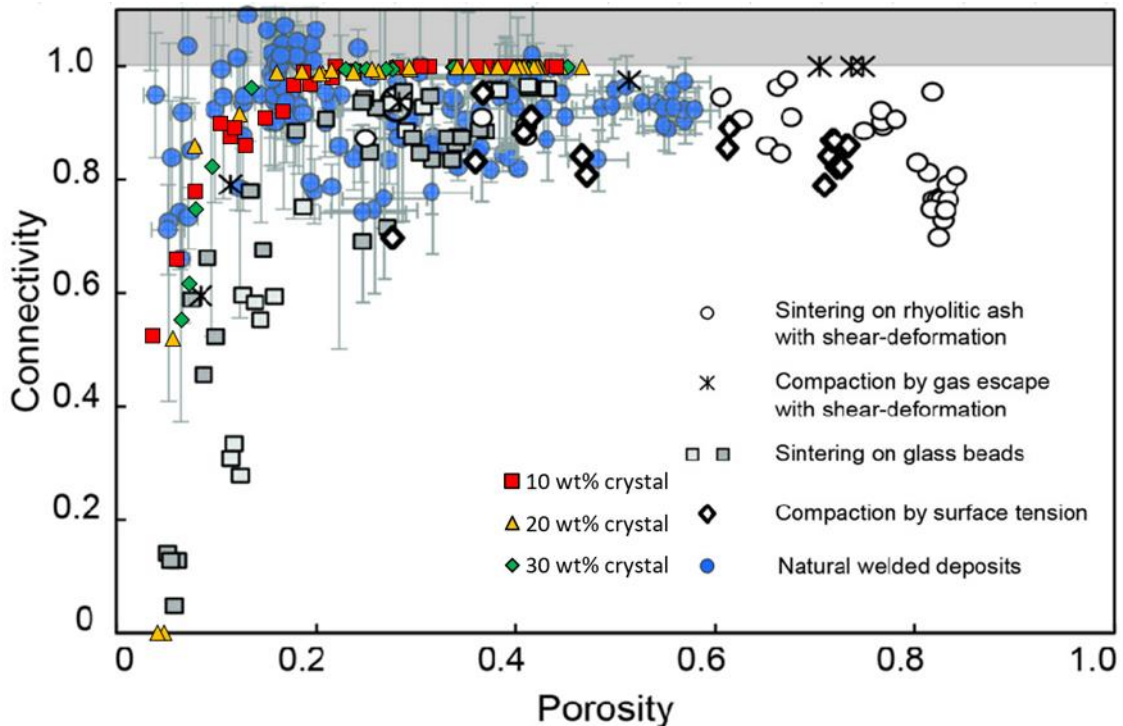


Figure 5.7: Connectivity of sintered glass-crystal samples plotted with results from densified experiments and natural samples. Red square = 10 wt% crystal experiments, yellow triangle = 20 wt% crystal experiments, green diamond = 30 wt% crystal experiments, open circle = sintered rhyolitic ash compaction, black crosses = rhyolitic melt compaction by gas escape, grey squares = glass bead sintering experiments, open diamond = surface tension compaction, blue circles = natural welded samples. Modified from Colombier et al (2017).

### 5.1.4 Pore analysis

The equivalent diameter, 3D shape, and volume of pores for two different crystal content experiments were used to investigate the evolution of the pores over an experiment, and to note any differences caused by the differing crystal content.

The major finding is that at any given time point in the experiments, there was approximately double the number of individual pores in the 30 wt% crystal content sample (30\_880) than in the 10 wt% crystal content sample (10\_880). Therefore, increased crystal content results in a greater number of pores and greater porosity.

In both experiments, the pore network is dominated by one large, convoluted pore during initial stages which slowly breaks down into smaller, convoluted pores as the experiment progresses. In Experiment 30\_880, the largest pore, >100 voxels in equivalent diameter, was still present at the experiment end unlike in Experiment 10\_880 where it had broken down into smaller sections before  $t = 1630$ . I suggest that the greater crystal content allowed the larger pore to

persevere for longer, perhaps by slowing the sintering rate, or by propping open sections of the pore and delaying the divergence and formation of smaller pores.

### 5.1.5 Volume fractions

The volume fraction of phases for xy slices were extracted from three samples to compare a sintered 10 wt% crystal sample (10\_880), a sintered 30 wt% crystal sample (30\_880), and an incompletely sintered 30 wt% crystal sample (30\_860). Both sintered samples show similar relationships in that glass was the largest phase but in the incompletely sintered sample, pore was the dominant phase. In general, the pore phase makes up a greater fraction of a slice of 30\_880 than 10\_880. This indicates that increased crystal content results in more pores which agrees with the findings from the pore analysis. There is a strong inverse relationship between the glass and crystal proportions in all of the samples, with glass making up a greater proportion of a slice if the crystal proportion is lower.

There appears to be a relationship between the crystal and pore phases in the sintered samples: the pore fraction is likely to be greater when there is a greater fraction of crystal in the slice. This may be because a greater crystal content increases the chance of crystal clusters and the pore space in and around the clusters has a better chance of preservation (Figure 5.8). The heat capacity,  $C_p$  of the olivine may locally affect the viscosity with  $C_p = 576 \text{ J/kg/}^\circ\text{K}$  at  $20^\circ\text{C}$  to  $\sim 900 \text{ J/kg/}^\circ\text{K}$  at  $800^\circ\text{C}$  (calculated using Equation 18 and 19 from Waples and Waples, 2004). This is much greater than the  $C_p$  of glass, meaning more energy is required to increase the temperature of an olivine particle by one temperature unit than a glass particle. The olivines could therefore be acting as miniature heat/energy sinks that very locally affects the viscosity of the glass, increasing it, and making it more likely that a pore forms or is retained by crystals. In addition, the crystals are not homogeneously distributed throughout the samples which is particularly evident in the 30 wt% crystal sample (Figure 5.8). This initial heterogeneous distribution of crystals is maintained during the sintering process, allowing chains and clusters of crystals to stay together. As they are not sintering, pore space between crystals can be preserved. More sufficient mixing by hand, or by a mechanical method, would be required to achieve a more homogeneous initial distribution. The crystal shape also affects how easy it is to distribute evenly within a sample; spheroid crystals would distribute much more efficiently than platelet shapes for example. With crystal contents  $>30 \text{ wt\%}$ , crystal clusters will become unavoidable.



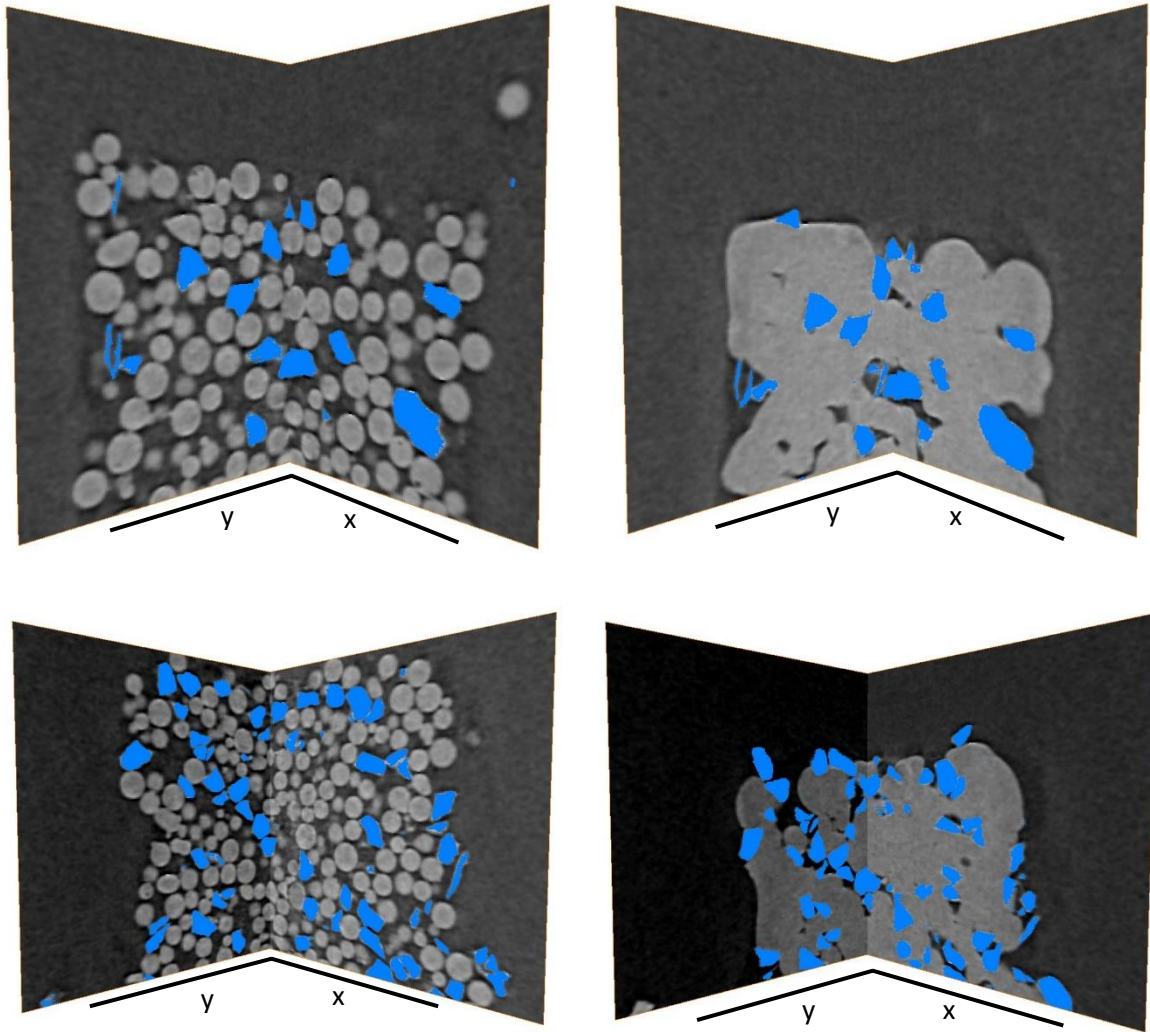


Figure 5.8: Intersecting xz and yz slice views of samples at the start (left) and end (right) of a 10 wt% crystal sample (top) and 30 wt% crystal sample (bottom) displaying the olivines in blue illustrating that the sample is not completely homogeneous, that crystal clusters are more common in the sample with more crystals, and that pore space seems to be preferentially located around crystal. The samples at the start of the experiment are 3mm across.

### 5.1.6 Olivine analysis

The two olivine populations were analysed to identify the particle size distribution and shapes of the crystals as these can affect the dispersal of crystals throughout the sample.

The dispersion of the crystals is mainly affected by the particle size distribution. Population 2 is more polydisperse than Population 1. This does not have a major effect on the overall

character of the sample as the glass beads are a greater component, and therefore, dictate that the sample is fairly monodisperse despite the polydisperse crystal populations. The equivalent diameter gives the diameter of crystals if they were spheres to compare with the glass beads. The majority of olivines in Population 1 are of equivalent size to that of the glass beads. The crystals of Population 2 are typically smaller than the glass beads. This means the microstructure of the sample is less homogeneous than that of a sample with larger rigid inclusions and smaller matrix particles, and the sintering rate is not as greatly slowed (Jean and Gupta, 1992; Yan et al., 2013). The aspect ratios and shape results both show that the crystals are elongated in shape, generally two times longer than wide. The olivines are not spherical, are more difficult to disperse evenly throughout the sample, and sinter faster than a spherical olivine of equivalent size (Cutler and Hendricksen, 1968; Giess et al., 1984; Giess et al., 1985). The modal shape of Population 2 is 1, indicating that the crystals are more spherical. However, the small sizes of the majority of particles introduces bias. The modal peak in equivalent diameter is 20  $\mu\text{m}$  which represents only 3 voxels across on the screen. This translates to most small particles being made up of  $\sim 27$  voxels or less, of which the shape is unlikely to be determined accurately (Figure 5.9). Overall, the jagged shape of particles and the size of the olivines in comparison to the matrix lend themselves to relatively faster sintering rates.

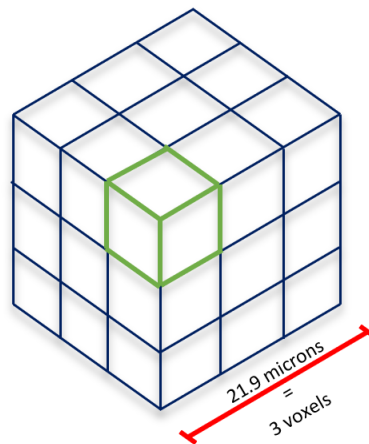


Figure 5.9: Schematic illustrating the shape bias in small particles. A voxel (highlighted in green) as part of a small particle e.g. a particle that would fall into the 20  $\mu\text{m}$  class of equivalent diameter and indicate a spherical shape from the shape factor of 1.

The amount of material that the olivine particles are in contact with at the beginning and end of an experiment was quantified for different crystal content experiments. Crystal-crystal interfaces were not identified as touching crystals were counted as a single larger crystal. Although there is an upward trend in all values, this is accounted for by the increasing crystal

content and hence increasing value of crystal interfaces. When the values are divided by the crystal content, there is no visible trend meaning that for any rigid inclusion content, the crystals stay in contact with similar proportions of material (Figure 5.10). As mentioned previously, the overall porosity of a sample increases with increasing crystal content. This suggests that the pores in contact with the crystals stay large or grow bigger if there are more crystals, or that there are more pores not in contact with the crystals (Figure 5.11). It is also possible that both mechanisms can occur concurrently.

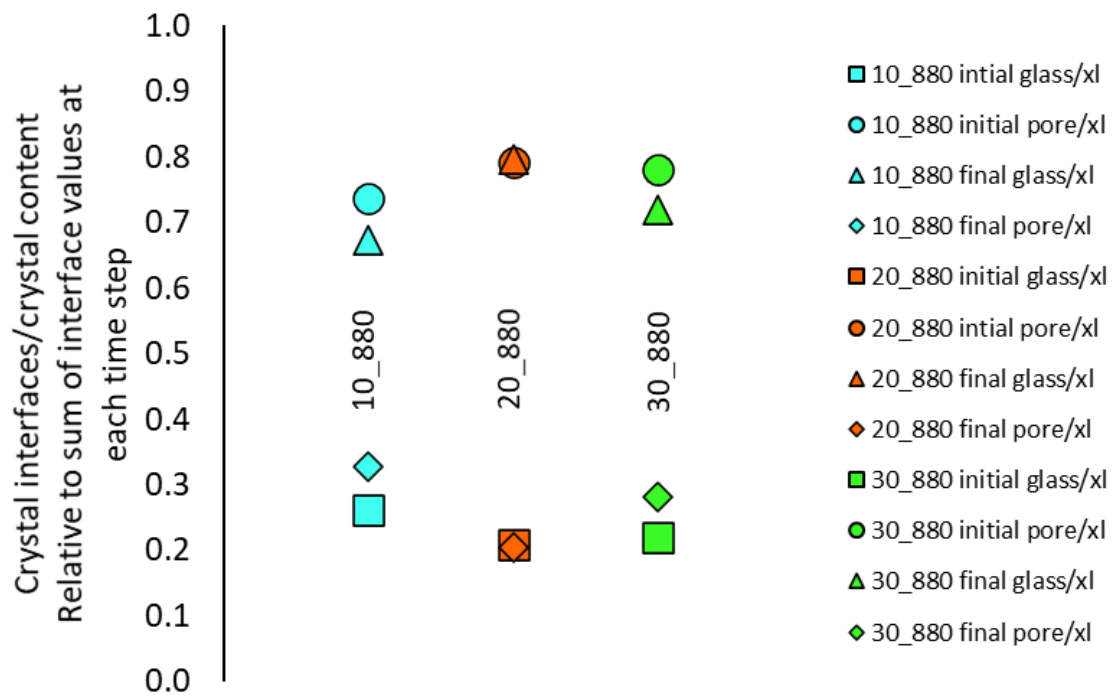


Figure 5.10: Actual crystal interface values divided by the crystal content showing that increasing crystal content does not appear to affect the proportions of materials in contact with crystals.

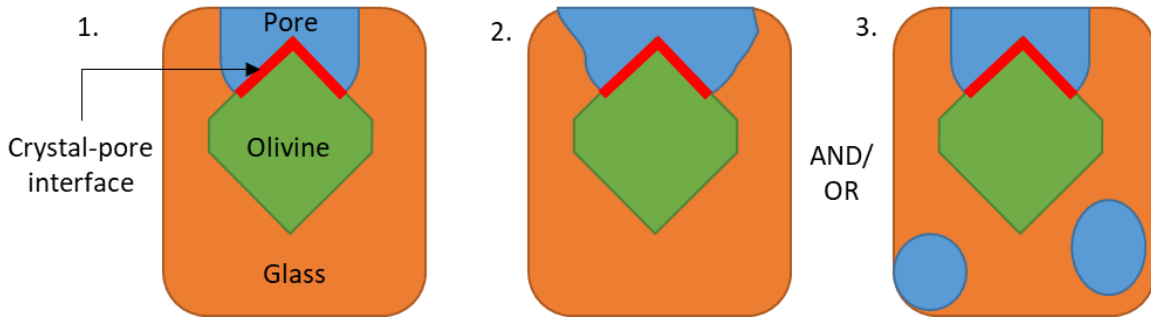


Figure 5.11: Simplified illustrations showcasing how the crystal-pore interface proportion can stay the same as (1) but increase porosity as crystal content increases. (1) Orange = glass. Green = olivine. Blue = pore. Red = crystal-pore interface. (2) The pore increases in size but does not further encompass the crystal. (3) More pores appear but do not interact with crystals.

### 5.1.7 DVC discussion

The magnitude and direction of particle displacements were tracked through experiments using DVC. The displacement is greater for the fully sintered experiment and more widespread throughout the whole sample than displacement in the incompletely sintered experiment. There appear to be patches within the vector fields of both experiments that do not show as much displacement which could be due to the presence of crystals restricting movement, either through physically being in the way, or as mentioned previously, diverting energy and heat away from the glass in very local proximities. There is a greater radial shrinkage component initially in Experiment 10\_880 (VF2) where the vectors are pointing towards the centre or slightly towards the centre at the base. This decreases as the experiment continues with the axial shrinkage taking over as the major component from VF3 to VF6. This indicates that the sample shrinks towards the centre initially and then shrinks down as sintering continues. However, the displacement vectors in Experiment 30\_860 almost exclusively point towards the base, indicating the shrinkage is mainly axial with very little radial shrinkage. From this, I suggest that temperature has a strong influence on the direction and magnitude of displacement that occurs within a sintering sample. It is unclear if the greater crystal content exerts an influence on the displacement vectors.

## 5.2 Crystals in experiments and nature

Sintering with crystals is important because they can have a pronounced effect on porosity and permeability, potentially extending the lifetime of permeable outgassing pathways (e.g. Sparks et al., 2000; Kolzenburg et al., 2012; Heap et al., 2014; Kendrick et al., 2016; Colombier et al., 2020). Crystals are near ubiquitous throughout volcanic systems. They can act as rigid inclusions and are not involved in the sintering process themselves (Figure 5.12).

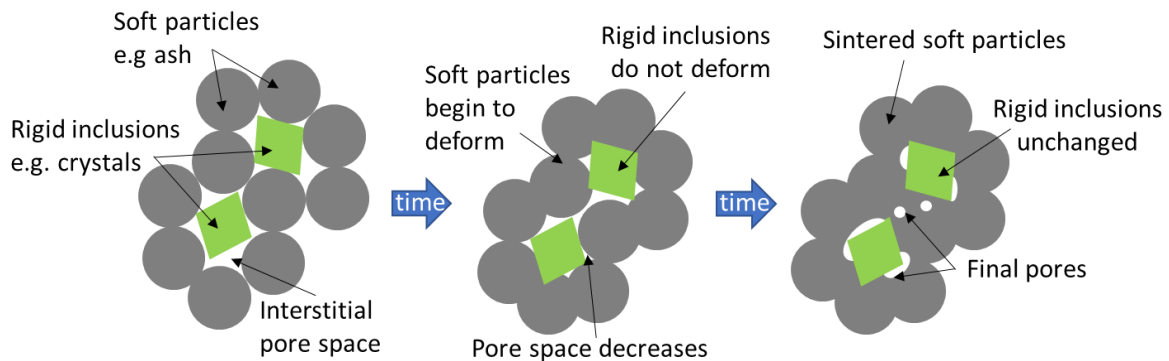


Figure 5.12: The evolution of sintering particles with rigid inclusions in the mixture.

They slow the rate of sintering melt, they can prop open pore networks, and these effects become more pronounced as crystal content increases (e.g. Eberstein et al., 2009; Amoros et al., 2019).

### 5.2.1 Volcanic processes

The evolving microstructure and porosity of these sintering samples is rarely captured in natural sintered products. This is because only a snapshot is preserved, usually once viscous sintering has reached equilibrium and once the material has fully sintered. Compaction processes and chemical alteration may also affect a natural sintered product, markedly increasing the differences to the final sintered samples of these ideal analogue experiments.

Welding processes are seen throughout volcanic systems (Figure 1.1). Silicic volcanic conduits are of particular interest for this project as efficient degassing may shift the behaviour of activity from explosive to effusive (Figure 5.13). The conduit is a place of high temperature, stresses, and strain rates where the magma can repeatedly fracture and repeatedly heal (e.g. Gonnerman and Manga, 2003; Tuffen et al., 2003). This likely induces a cycle of fracturing and sintering that continues as long as the necessary conditions are sustained (Figure 1.4).

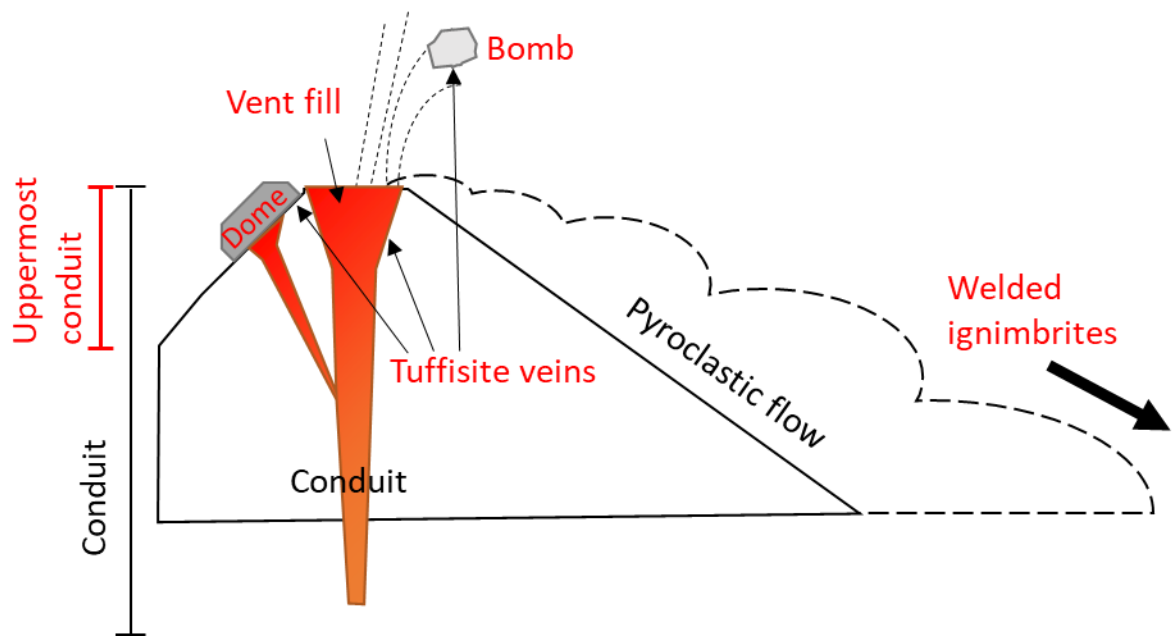


Figure 5.13: Schematic of a silicic volcanic conduit highlighting regions and features where this work may be particularly applicable.

The experiments of this work were run under non-isothermal conditions with the samples held at specific dwell temperatures, under normal atmosphere pressure, and with increasing crystal content. These experiment results best lend themselves to tuffisite veins in the upper tens of metres of the volcanic conduit, or infiltrating features such as domes. This is for several reasons. High temperatures are maintained for long periods of time, the effect of pressure is low near the surface and compaction processes are less likely to be dominant, shear-induced fractures within the conduit provide starting material to sinter, and there are examples of tuffisites with crystal contents ranging from essentially 0%, up to  $\geq 80$  vol% (e.g. Stasiuk et al., 1996; Tuffen et al., 2003; Kolzenburg et al., 2012; Kendrick et al., 2016).

Experiments replicating the cyclicity of fracturing and sintering would come closer to mimicking expected upper conduit conditions and provide a more realistic idea of natural sintering.

### 5.2.1.1 Tuffisite veins and crystals

Tuffisite veins, permeable outgassing pathways, are present in the upper conduit and vent-filling proximal deposits of volcanoes around the world and in volcanic settings from basaltic diatremes (e.g. Cloos, 1941), to andesitic domes (e.g. Kolzenburg et al., 2012), to rhyolitic

conduits (e.g. Tuffen et al., 2003). This outgassing mechanism may facilitate extensive degassing of a magma system, reducing overpressure, and potentially help shift behaviour from an explosive to effusive regime (e.g. Stasiuk et al., 1996; Degruyter et al., 2012; Berlo et al., 2013; Schipper et al., 2013; Cabrera et al., 2015; Kendrick et al., 2016; Saubin et al., 2016; Paisley et al., 2019).

The style of a volcanic eruption is dominantly controlled by the efficiency of outgassing of volatiles from shallow level systems (e.g. Schipper et al., 2013) which is in turn governed by the connectivity and permeability of a pore network (e.g. Rust and Cashman, 2004). If the tuffsite veins are connected to the surface, they can allow degassing of material within the conduit. They form or take advantage of natural fractures and become filled with fractured volcanic material as a mobile fluid phase deposit grains, with some even showing sedimentary features such as bedding (Stasiuk et al., 1996, Tuffen et al., 2003). If the particles mostly consist of fractured melt and temperature is above  $T_g$ , these particles weld together, reducing porosity and permeability until the vein is completely welded shut (Figure 1.4). The porosity at which the pore network becomes patches of isolated pores and there is no thoroughfare for volatiles to travel along is called the percolation threshold. In this work,  $\varphi_c$  was defined as the porosity at which connectivity became 0. From sintered natural deposits with high crystal contents (e.g. Kendrick et al., 2016; Lindoo et al., 2017), it has been demonstrated that high crystal contents can slow or even possibly stop welding processes altogether (e.g. Sparks et al., 2000). This should be reflected in connectivity results, with the connectivity remaining close to 1 for longer (i.e. the drop in connectivity does not occur until lower porosities).

In this work, the drop in connectivity does not happen until lower porosities are reached when compared to crystal-free sintered glass data collated in Colombier et al (2017; Figure 5.7). The porosity continually decreases over time, and so, a lower porosity means a greater length of time has taken place. The crystal content of these experiments is the only variable that would affect the shape that the data plots. Therefore, the high connectivity that is retained to lower porosities indicates that crystals can allow significant outgassing for a longer period of time compared to sintering materials without crystals, and hence permeability is also retained for a longer period of time. If permeability values stay higher for a greater length of time, degassing is more efficient, and a greater proportion of the system can be degassed. This may potentially reduce the frequency of explosive episodes of volcanism, and/or quicken the transition from explosive to effusive regimes, because if the crystals can affect the efficiency of outgassing, the style of eruption can be affected (e.g. Schipper et al., 2013).

Typical tuffisite vein compositions depend entirely on the host that is infiltrated. As crystals are almost ubiquitous in volcanic systems, it is not uncommon for there to be at least a small (<5 vol%) crystal fraction present. Generally, a mix of micron to centimetre sized clasts are deposited within the vein and may be non-welded to fully welded.

Kolzenburg et al (2012) found that the tuffisite veins contained a greater fraction of phenocryst content than the host rock (~80 vol% compared to ~45 vol%) which indicates that there may be a process that preferentially leaves crystals behind in the vein. Perhaps the shape of particles has an effect (e.g. fragmented phenocrysts and rounded lithics, Kolzenburg et al., 2012), or phenocrysts with greater density are deposited by the flow of gas whilst lower density melt is carried further along or out of the vein.

Kendrick et al (2016) estimated that the sintering timescale at Volcàn de Colima with 60 vol% crystal content was on the order of a week, to several weeks, much greater than the timescale of minutes to days suggested for tuffisite veins with negligible crystal content (e.g. Castro et al., 2012). This suggests the crystals keep the veins permeable for longer. For moderate crystal contents, they may do this by forming clusters which was seen in this work (Figure 5.8), preserving pore space at the centre by preventing sintering melt from reaching it (Figure 5.14).

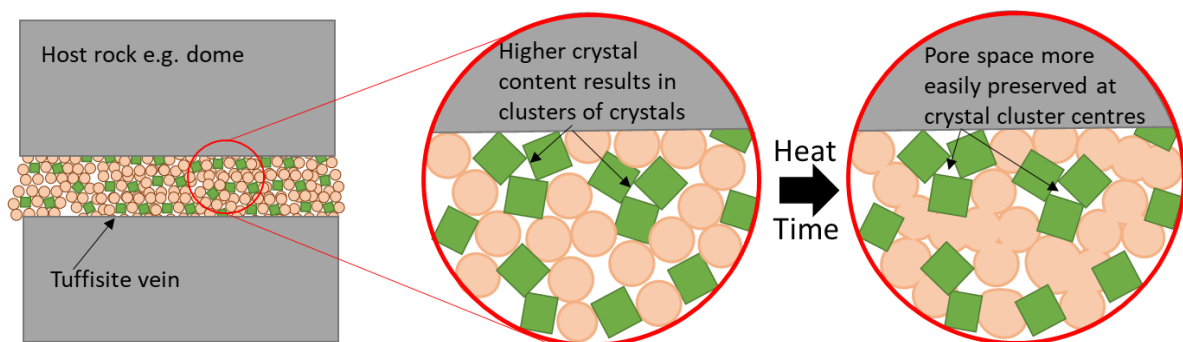


Figure 5.14: Sintering in a tuffisite vein with a moderate crystal content. Crystal particles clump together into clusters which preserve pore space as melt particles sinter around the cluster.

Or, with a high enough crystal content, they may form a framework that is unaffected by viscous sintering, with only small patches of melt particles sintering and very locally affecting the porosity (Figure 5.15). In this case, the veins may not every fully close unless conditions for solid-state sintering of the crystals are met.



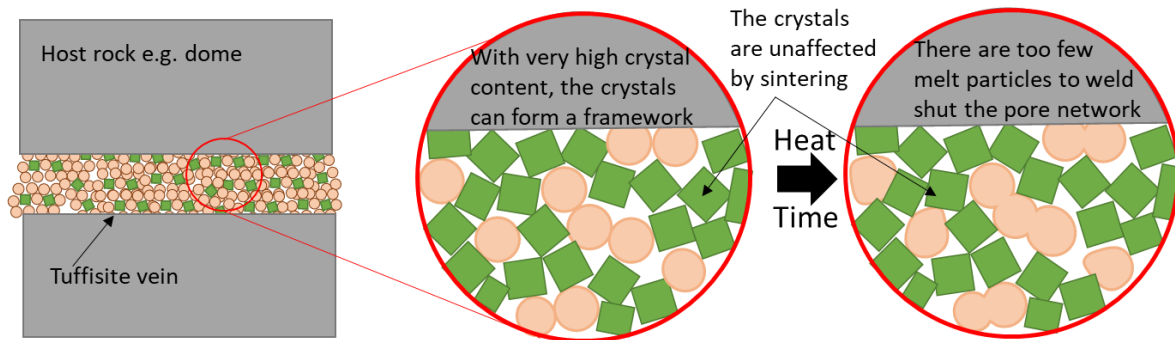


Figure 5.15: Sintering in a tuffisite vein with very high crystal content. Local patches of melt particles sinter but the majority of the crystal framework is unaffected.

With more time to degas compared to crystal-free systems, degassing is more effective, a greater quantity of gas can escape, and pressure build up in the conduit could be lessened. The more efficient outgassing may then result in longer intervals between explosive events and/or it may help transition to effusive behaviours.

### 5.2.1.2 Welded ignimbrites

Welded ignimbrite deposits with high emplacement temperatures are another example of where these results may be applicable. However, the temperature is decreasing from the moment of deposition, and the emplacement temperature of most ignimbrites may not be particularly high to begin with and may not stay above  $T_g$  for long. In particularly thick deposits, a compacting welding regime would be more dominant the closer to the bottom of the deposit, and pressure is not considered in these experiments.

### 5.2.2 Experiments to nature

The experiments are simplified and idealistic with well controlled heating rates and temperatures, spherical sintering particles, furnace temperatures above  $T_g$  and up to approximately 880°C. Yet in nature, there is a huge variety of temperatures, times, and pressures. If we consider just the conduit, there can be massive differences between the temperature at the surface exposed to the atmosphere and temperatures deeper in the conduit. With increasing depth or material overlying and acting as a load, the effects of pressure are added. Further investigations into sintering conditions at different locations in and out of the volcanic system (Figure 1.1) is needed to determine what effects these temperatures and

pressures have on the sintering process. Lastly, the time can greatly affect the degree of sintering. A lower temperature and longer time span could result in the same degree of sintering as that of higher temperature and shorter time, but it is not known if there are ways to distinguish between the two regimes. These are a few of the complexities that can build upon this base of experimental data.

Natural welded samples overwrite the section of sintering that is investigated here, as densification and compaction eliminate much of the pore space regardless of crystal content. As the samples of this work did not reach equilibrium, it is unknown whether the differences in final porosity caused by the differing crystal content would be preserved. However, this could still be useful in recreating a general history of sintered products. For example, a natural sample with high rigid inclusion content would sinter more slowly than a sample with low rigid inclusion content under the same conditions, so it could be assumed the rigid inclusions prolonged the outgassing phase. The absence of pores in a high crystal content sample would suggest a significant period of time above  $T_g$ , but below the melting temperatures of the crystals, where sintering occurred, and compaction removed remaining pore space.

### **5.2.2.1 Particle size distribution**

In nature, the particle size distribution of particles produced by fracturing in volcanic conduits is a factor to consider when determining the effects and rates of sintering, as well as the size of any rigid inclusions in relation to the sintering ash matrix. I believe a common example where this could be applied is with larger phenocrysts in a finer grained ash matrix. In tuffisite veins, the sizes of grains and clasts range from microns up to tens of millimetres, generally with a fine matrix and some larger clasts/phenocrysts (e.g. Saubin et al., 2016). Rigid inclusions that are larger than the sintering matrix particles slow sintering as it forms a more homogeneous microstructure (Jean and Gupta, 1992; Yan et al., 2013). Smaller particles sinter faster than larger particles, so tuffisite veins that have finer particles likely did not outgas for as long as those with larger clasts.

Permeability can be affected by the range of particle sizes. A polydisperse population of particles would have a slightly lower permeability compared to a monodisperse population as particles take up space more efficiently (Figure 5.4). This work represents a monodisperse population of particles, with crystals of roughly similar size. Garnering the actual permeability of the samples from this work, how it changes over the course of experiments, and how it

compares to other work would be a future avenue of research to be considered because a high connectivity alone does not necessarily mean high permeability.

### **5.2.2.2 Geochemistry**

The geochemistry of the sintering particles in volcanic conditions could have a major effect on sintering, with changing silica content the largest contributor as the viscosity increases with increasing SiO<sub>2</sub>. These experiments were replicating the chemistry of silicic melts as they are far more likely to be explosive. Understanding the role of sintering on explosivity in silicic conduits is important. However, the effects of lower silica content sintering is an important future avenue as well as investigating the roles of other elements such as differing alkaline content.

Tuffisite veins have been found in a wide variety of compositions, from basaltic (e.g. Cloos 1941), to andesitic (Kendrick et al., 2016), to rhyolitic (Tuffen et al., 2003). They are, however, most commonly found in rhyolitic compositions (Heiken et al., 1988; Stasiuk et al., 1996; Gonnerman and Manga, 2003; Tuffen et al., 2003; Cabrera et al., 2011; Castro et al., 2012; Berlo et al., 2013; Castro et al., 2014). I think this is because the viscosity of the melt is higher, the magma behaviour is non-Newtonian, there are shear stresses and more fragmentation events, and the temperatures are generally lower than basaltic systems. Therefore, evidence of tuffisite veins is more readily preserved and more easily distinguished. I think tuffisite veins have a degassing role to play in all systems but are more important as an outgassing mechanism in rhyolitic systems. Fractures are more abundant from the greater stresses within the conduit and with the generally lower temperatures of rhyolitic melts, I suggest that phenocrysts and crystals from melt crystallisation would form a greater component of any sintering mixture. Therefore, when compared to basaltic systems, I would expect tuffisite veins to be longer lived and to play a greater role in degassing the system because of the increased presence of crystals.

## 6. Conclusions

This is the first work investigating the effects of systematically increasing crystal content on sintering in volcanological settings, where crystals are acting as rigid inclusions. The use of synchrotron XCT is crucial for this work as it is the only method that allows non-destructive *in situ* observation of the evolving microstructure. This allows the visualisation and quantification of the exterior and interior of 3D data throughout an experiment so that changes in sintering behaviour can be directly linked to the presence of crystals.

The total porosity decreases, and the disconnected porosity increases as sintering continues. However, the presence of crystals affects the final porosity value: a higher crystal content results in a greater final porosity. The porosity and time data can be normalized to enable comparisons between experiments and previous work of different temperature and time conditions. Currently, this work requires further temperature calibration to enable the effect of crystals to be seen clearly in normalized data.

The porosity networks of these samples initially disconnect through the z-axes and typically do so by closing a ‘neck’ structure. An increased crystal content results in more pores, potentially by preventing the closure of a ‘neck’. The high connectivity of these sintered glass bead samples containing crystals is maintained to lower porosities (i.e. connected pores are maintained for longer periods of time) than that of sintered glass beads alone. This indicates that crystals are the cause of this longer-lived connectivity and may prolong outgassing. This supports previous research that demonstrated crystal-rich tuffisite veins welded on the timescale of a week to weeks compared to crystal-free tuffisite veins that weld on the timescale of minutes to hours.

Future work would be best focussed on:

- Sintering experiments with crystal contents up to 60 vol% until the final porosity is at equilibrium.
  - Experiments run under the temperature/pressure conditions with the only difference being crystal content varying between 0-60 vol% would allow the effect of crystals to be picked out effectively. If they are left to run so that the porosity reaches equilibrium, an estimate of lifespans for tuffisite veins of varying crystal content could be made.

- Sintering experiments with crystal contents up to 60 wt% at different pressures to replicate different sintering conditions in volcanic conduits.
  - This work is best suited to the upper conduit where pressure is close to 1 atmosphere. However, tuffisite veins are known to extend to at least 500m depth, sintering at conduit walls may occur to 1.5km depth, and a particularly thick ignimbrite deposit that is welding can exert pressure at the centre of the deposit. The longevity of degassing would be expected to be shorter with increasing pressure, but timescales could be quantified. Again, with crystal content varying across experiments between 0-60 vol%, the effect of crystals on sintering could be picked out and see how much of a difference pressure makes.
- Permeability calculations.
  - Although porosity is a good initial measure of welding degree, the rate at which volatiles can be degassed and the overall amount that can be degassed can only be quantified with permeability tests. Other works have permeability results for crystal-bearing sintering samples that could be used for comparison.
- Understanding the textures of natural sintered material containing crystals by replicating textures through experimental work.
  - Natural material introduces further complexities such as irregular particles shapes and sizes, multiple clast types, and differing silica compositions which cannot be replicated well using ideal starting analogue materials.

# Appendix

Parameter	Particle Size Distribution (diameter)				Composition			
	Mean value	10% finer than	50% finer than	90% finer than	SiO <sub>2</sub>	Na <sub>2</sub> O	CaO +MgO	Al <sub>2</sub> O <sub>3</sub>
<b>Units</b>	Micron	Micron	Micron	Micron	%	%	%	%
	180	140	175	220	71-73	12-14	11-16	0.5-1.5

Appendix Table 1: Properties of 1922 A-glass Spheriglass© spheres, Potters Industries LLC. (<https://www.pqcorp.com/products/markings-spheres/solid-glass-microspheres>)

Scan number	Scan frame	Histogram minimum	Histogram maximum
<i>155</i>	<i>0</i>	<i>19000</i>	<i>32000</i>
<b>156</b>	0	19000	32000
<b>156</b>	18	24000	33000
<b>156</b>	36	23000	33000
<b>157</b>	0	18000	29000
<b>157</b>	9	18000	29000
<b>157</b>	18	20000	31000
<b>157</b>	27	20000	31000
<b>157</b>	36	20000	31000
<b>158</b>	0	18000	30000
<b>158</b>	9	18000	30000
<b>158</b>	18	18000	30000
<b>158</b>	27	20000	31000
<b>158</b>	36	20000	31000
<b>159</b>	0	20000	31000
<b>159</b>	9	20000	31000
<b>159</b>	18	20000	31000
<b>159</b>	27	20000	31000
<b>159</b>	36	20000	31000
<i>162</i>	<i>0</i>	<i>30000</i>	<i>44000</i>
<b>163</b>	0	30000	41000
<b>163</b>	1	30000	41000
<b>163</b>	2	30000	41000
<b>163</b>	4	30000	41000
<b>163</b>	6	29500	41500
<b>163</b>	9	29500	41500
<b>163</b>	12	29500	41000
<b>163</b>	18	29000	41000
<b>163</b>	24	30000	41000
<b>163</b>	30	29500	40500
<b>163</b>	36	30000	41000
<b>164</b>	0	24000	36000

165	<b>0</b>	<b>27000</b>	<b>39500</b>
166	0	27000	41000
166	1	28000	40000
166	2	28000	40000
166	4	28000	40000
166	6	28000	40000
166	9	28000	40000
166	12	28000	40000
166	18	28000	40000
166	24	28000	40000
166	30	28000	40000
166	36	28000	40000
167	0	28000	48000
170	<b>0</b>	<b>24000</b>	<b>34000</b>
171	0	24500	36000
171	1	25000	36000
171	2	25000	36000
171	4	25000	36000
171	6	25000	36000
171	9	25000	36000
171	12	25500	36000
171	18	25500	36000
171	24	25500	36000
171	30	25500	36000
171	36	25500	36000
172	0	21000	31000
174	<b>0</b>	<b>12000</b>	<b>18000</b>
175	0	10000	17000
175	1	10000	17000
175	2	10000	17000
175	4	10000	17000
175	6	10000	17000
175	9	10000	17000
175	12	8500	18000
175	18	10000	17000
175	24	11000	17000
175	36	10000	17000
180	<b>0</b>	<b>18000</b>	<b>37000</b>
181	0	17000	32000
181	1	17000	32000
181	2	17000	32000
181	4	17000	32000
181	6	17000	32000
181	9	17000	32000
181	12	17000	32000
181	18	17000	32000
181	24	17000	32000
181	30	17000	32000

<b>181</b>	36	17000	32000
<b>183</b>	0	17000	32000
<i>185</i>	<b>0</b>	<b>16000</b>	<b>36000</b>
<b>186</b>	0	23500	36000
<b>186</b>	1	23500	36000
<b>186</b>	2	23500	36000
<b>186</b>	4	23500	36000
<b>186</b>	6	23500	36000
<b>186</b>	9	23500	36000
<b>186</b>	12	23500	36000
<b>186</b>	18	23500	36000
<b>186</b>	24	23500	36000
<b>186</b>	30	23500	36000
<b>186</b>	36	23500	36000
<b>188</b>	0	22000	35000
<i>190</i>	<b>0</b>	<b>21000</b>	<b>30500</b>
<b>191</b>	0	23000	30000
<b>191</b>	1	23000	30000
<b>191</b>	2	23000	30000
<b>191</b>	4	23000	30000
<b>191</b>	6	23000	30000
<b>191</b>	9	23000	30000
<b>191</b>	12	23000	30000
<b>191</b>	18	23000	30000
<b>191</b>	24	23000	30000
<b>191</b>	30	23000	30000
<b>191</b>	36	23000	30000
<b>194</b>	0	20000	30000

Appendix Table 2: Input values for *Auto Thresholding* module in Figure 3.3.

Experiment	Min x	Min y	Min z	Size x	Size y	Size z
Large subvolume						
<b>10_860_longrun</b>	76	56	0	556	647	486
<b>10_860</b>	57	154	0	558	560	486
<b>20_880</b>	130	198	0	517	524	486
<b>30_880</b>	58	43	0	655	674	486
<b>30_860</b>	112	129	0	534	518	397
<b>20_860</b>	123	133	0	516	530	376
<b>10_880</b>	126	140	0	532	508	432
<b>20_860_polydisperse</b>	122	103	0	519	547	369
Small subvolume						
<b>10_860_longrun</b>	188	259	232	207	192	136
<b>10_860</b>	170	204	146	246	192	136
<b>20_880</b>	136	163	178	222	199	147
<b>30_880</b>	175	248	145	205	196	179
<b>30_860</b>	185	172	107	197	201	131
<b>20_860</b>	160	163	69	219	135	129



<b>10_880</b>	146	142	95	192	195	129
<b>20_860_polydisperse</b>	181	183	73	193	195	109

Appendix Table 3: Input values to extract large and small subvolumes in Figure 3.6.

	Start	Start	Start	End	End	End
Method	Weka	Phases	Manual	Weka	Phases	Manual
Number of crystals	4846	161	157	3156	117	152
Weighed crystal fraction	0.10	0.10	0.10	0.10	0.10	0.10
Calculated crystal fraction	0.109	0.098	0.104	0.135	0.133	0.091

Appendix Table 4: Comparison of values produced by different processing methods for the initial and final image of Experiment 10\_880.

Experiment	Frame	Vector field image	Time 1	Time 2
-	-	-	s	s
10_880	186_00 to 186_06	VF1	663	843
10_880	186_06 to 186_12	VF2	843	1023
10_880	186_12 to 186_18	VF3	1023	1203
10_880	186_18 to 186_24	VF3	1203	1383
10_880	186_24 to 186_30	VF5	1383	1563
10_880	186_30 to 186_36	VF6	1563	1743
30_860	175_00 to 175_06	VF7	429	609
30_860	175_06 to 175_12	VF8	609	789
30_860	175_12 to 175_18	VF9	789	969
30_860	175_18 to 175_24	VF10	969	1149
30_860	175_24 to 175_30	VF11	1149	1329
30_860	175_30 to 175_36	VF12	1329	1509

Appendix Table 5: Input scans and times for the displacement vector fields.

## References

- AMOROS, J. L., BLASCO, E., MORENO, A., ZUMAQUERO, E. & FELIU, C. 2019. Non-isothermal sintering of powdered vitrified composites. A kinetic model. *Materials Letters*, 236, 236-239.
- ANDREWS, G. D. M. & BRANNEY, M. J. 2011. Emplacement and rheomorphic deformation of a large, lava-like rhyolitic ignimbrite: Grey's Landing, southern Idaho. *Geological Society of America Bulletin*, 123, 725-743.
- ASHWELL, P. A., KENDRICK, J. E., LAVALLEE, Y., KENNEDY, B. M., HESS, K. U., VON AULOCK, F. W., WADSWORTH, F. B., VASSEUR, J. & DINGWELL, D. B. 2015. Permeability of compacting porous lavas. *Journal of Geophysical Research-Solid Earth*, 120, 1605-1622.
- BERLO, K., TUFFEN, H., SMITH, V. C., CASTRO, J. M., PYLE, D. M., MATHER, T. A. & GERAKI, K. 2013. Element variations in rhyolitic magma resulting from gas transport. *Geochimica Et Cosmochimica Acta*, 121, 436-451.
- BOCCACCINI, A.R., 1995. Sintering of glass matrix composites containing a particulate inclusion phase. *Advanced Composites Letters*, 4(5), p.096369359500400502.
- BOCCACCINI, A. R. 1997. Determination of internal stresses during sintering of dispersion reinforced glass matrix composites. *Materials Chemistry and Physics*, 48, 186-189.
- BOCCACCINI, A. R. 1998. On the sintering with rigid inclusions. *Materialwissenschaft Und Werkstofftechnik*, 29, 77-79.
- BOCCACCINI, A. R. & CONRADT, R. 2001. Isotropic shrinkage of platelet containing glass powder compacts during isothermal sintering. *International Journal of Inorganic Materials*, 3, 101-106.
- BOCCACCINI, A. R. & OLEVSKY, E. A. 1999. Processing of platelet-reinforced glass matrix composites: effect of inclusions on sintering anisotropy. *Journal of Materials Processing Technology*, 96, 92-101.
- BORDIA, R. K. & RAJ, R. 1986. Analysis of Sintering of a Composite with a Glass or Ceramic Matrix. *Journal of the American Ceramic Society*, 69, C55-C57.
- BORDIA, R. K. & SCHERER, G. W. 1988. On Constrained Sintering .3. Rigid Inclusions. *Acta Metallurgica*, 36, 2411-2416.
- BOUVARD, D., 2000. Densification behaviour of mixtures of hard and soft powders under pressure. *Powder technology*, 111(3), 231-239.
- BRANNEY, M. J., KOKELAAR, B. P. & MCCONNELL, B. J. 1992. The Bad Step Tuff - a Lava-Like Rheomorphic Ignimbrite in a Calc-Alkaline Piecemeal Caldera, English Lake District. *Bulletin of Volcanology*, 54, 187-199.
- BRIGGS, N. D. 1976. Welding and Crystallization Zonation in Whakamaru Ignimbrite, Central-North-Island, New-Zealand. *New Zealand Journal of Geology and Geophysics*, 19, 189-212.

- BROWN, D. J. & BELL, B. R. 2013. The emplacement of a large, chemically zoned, rheomorphic, lava-like ignimbrite: the Sgurr of Eigg Pitchstone, NW Scotland. *Journal of the Geological Society*, 170, 753-767.
- CABRERA, A., WEINBERG, R. F. & WRIGHT, H. M. N. 2015. Magma fracturing and degassing associated with obsidian formation: The explosive-effusive transition. *Journal of Volcanology and Geothermal Research*, 298, 71-84.
- CABRERA, A., WEINBERG, R. F., WRIGHT, H. M. N., ZLOTNIK, S. & CAS, R. A. F. 2011. Melt fracturing and healing: A mechanism for degassing and origin of silicic obsidian. *Geology*, 39, 67-70.
- CASSIDY, M., MANGA, M., CASHMAN, K. & BACHMANN, O. 2018. Controls on explosive-effusive volcanic eruption styles. *Nature Communications*, 9.
- CASTRO, J. M., BINDEMAN, I. N., TUFFEN, H. & SCHIPPER, C. I. 2014. Explosive origin of silicic lava: Textural and delta D-H<sub>2</sub>O evidence for pyroclastic degassing during rhyolite effusion. *Earth and Planetary Science Letters*, 405, 52-61.
- CASTRO, J. M., CORDONNIER, B., TUFFEN, H., TOBIN, M. J., PUSKAR, L., MARTIN, M. C. & BECHTEL, H. A. 2012. The role of melt-fracture degassing in defusing explosive rhyolite eruptions at volcan Chaiten. *Earth and Planetary Science Letters*, 333, 63-69.
- CIMARELLI, C., YILMAZ, T., COLOMBIER, M., VILLANOVA, J., HÖFER, L., HESS, K.-U., RUTHENSTEINER, B. & DINGWELL, D. Micro- and nano-CT textural analysis of an experimental volcanic fulgurite. *EGU General Assembly Conference Abstracts*, 2017. 17928.
- CLOOS, H., 1941. Bau und Tätigkeit von Tuffschloten. *Geologische Rundschau*, 32(6-8), pp.709-800.
- COLOMBIER, M., WADSWORTH, F. B., GURIOLI, L., SCHEU, B., KUEPPERS, U., DI MURO, A. & DINGWELL, D. B. 2017. The evolution of pore connectivity in volcanic rocks. *Earth and Planetary Science Letters*, 462, 99-109.
- COLOMBIER, M., WADSWORTH, F. B., SCHEU, B., VASSEUR, J., DOBSON, K. J., CACERES, F., ALLABAR, A., MARONE, F., SCHLEPUTZ, C. M. & DINGWELL, D. B. 2020. In situ observation of the percolation threshold in multiphase magma analogues. *Bulletin of Volcanology*, 82.
- COSTA, A. 2005. Viscosity of high crystal content melts: Dependence on solid fraction. *Geophysical Research Letters*, 32.
- CUTLER, I. B. & HENRICHSEN, R. E. 1968. Effect of particle shape on the kinetics of sintering of glass. *Journal of the American Ceramic Society*, 51, 604-604.
- DE JONGHE, L. & RAHAMAN, M. 1984. Loading dilatometer. *Review of scientific instruments*, 55, 2007-2010.
- DEGRAFFENRIED, R.L., LARSEN, J.F., GRAHAM, N.A. & CASHMAN, K.V., 2019. The influence of phenocrysts on degassing in crystal-bearing magmas with rhyolitic groundmass melts. *Geophysical Research Letters*, 46(10), pp.5127-5136.
- DEGRUYTER, W., BACHMANN, O., BURGISSER, A. & MANGA, M. 2012. The effects of outgassing on the transition between effusive and explosive silicic eruptions. *Earth and Planetary Science Letters*, 349, 161-170.

- DOBSON, K. J., COBAN, S. B., MCDONALD, S. A., WALSH, J. N., ATWOOD, R. C. & WITHERS, P. J. 2016. 4-D imaging of sub-second dynamics in pore-scale processes using real-time synchrotron X-ray tomography. *Solid Earth*, 7, 1059-1073.
- DRAKOPOULOS, M., CONNOLLEY, T., REINHARD, C., ATWOOD, R., MAGDYSYUK, O., VO, N., HART, M., CONNOR, L., HUMPHREYS, B. & HOWELL, G. 2015. I12: the joint engineering, environment and processing (JEEP) beamline at diamond light source. *Journal of synchrotron radiation*, 22, 828-838.
- DUCAMP, V. C. & RAJ, R. 1989. Shear and densification of glass powder compacts. *Journal of the American Ceramic Society*, 72, 798-804.
- DUTTON, R. E. & RAHAMAN, M. N. 1992. Sintering, Creep, and Electrical Conductivity of Model Glass-Matrix Composites. *Journal of the American Ceramic Society*, 75, 2146-2154.
- EBERSTEIN, M., REINSCH, S., MULLER, R., DEUBENER, J. & SCHILLER, W. A. 2009. Sintering of glass matrix composites with small rigid inclusions. *Journal of the European Ceramic Society*, 29, 2469-2479.
- FAGENTS, S.A., GREGG, T.K. and LOPES, R.M. eds., 2012. *Modeling volcanic processes: the physics and mathematics of volcanism*. Cambridge University Press. pp. 55-84
- FARQUHARSON, J. I., HEAP, M. J., LAVALLEE, Y., VARLEY, N. R. & BAUD, P. 2016. Evidence for the development of permeability anisotropy in lava domes and volcanic conduits. *Journal of Volcanology and Geothermal Research*, 323, 163-185.
- FRENKEL, J. 1945. Viscous flow of crystalline bodies under the action of surface tension. *J. phys.*, 9, 385.
- FREUNDT, A. & SCHMINCKE, H. U. 1995. Eruption and Emplacement of a Basaltic Welded Ignimbrite during Caldera Formation on Gran-Canaria. *Bulletin of Volcanology*, 56, 640-659.
- GARDNER, J. E., WADSWORTH, F. B., LLEWELLIN, E. W., WATKINS, J. M. & COUMANS, J. P. 2018. Experimental sintering of ash at conduit conditions and implications for the longevity of tuffisites. *Bulletin of Volcanology*, 80.
- GIEHL, C., BROOKER, R. A., MARXER, H. & NOWAK, M. 2017. An experimental simulation of volcanic ash deposition in gas turbines and implications for jet engine safety. *Chemical Geology*, 461, 160-170.
- GISS, E. A., FLETCHER, J. P. & HERRON, L. W. 1984. Isothermal sintering of cordierite-type glass powders. *Journal of the American Ceramic Society*, 67, 549-552.
- GISS, E. A., GUERCI, C. F., WALKER, G. F. & WEN, S. H. 1985. Isothermal Sintering of Spheroidized Cordierite-Type Glass Powders. *Journal of the American Ceramic Society*, 68, C-328-C-329.
- GONNERMANN, H. M. & MANGA, M. 2003. Explosive volcanism may not be an inevitable consequence of magma fragmentation. *Nature*, 426, 432.
- GRUNDER, A. & RUSSELL, J. 2005. Welding processes in volcanology: insights from field, experimental, and modeling studies. *Journal of Volcanology and Geothermal Research*, 142, 1-9.

- HEAP, M. J., FARQUHARSON, J. I., WADSWORTH, F. B., KOLZENBURG, S. & RUSSELL, J. K. 2015. Timescales for permeability reduction and strength recovery in densifying magma. *Earth and Planetary Science Letters*, 429, 223-233.
- HEAP, M. J., KOLZENBURG, S., RUSSELL, J. K., CAMPBELL, M. E., WELLES, J., FARQUHARSON, J. I. & RYAN, A. 2014. Conditions and timescales for welding block-and-ash flow deposits. *Journal of Volcanology and Geothermal Research*, 289, 202-209.
- HEAP, M. J., TUFFEN, H., WADSWORTH, F. B., REUSCHLE, T., CASTRO, J. M. & SCHIPPER, C. I. 2019. The Permeability Evolution of Tuffisites and Implications for Outgassing Through Dense Rhyolitic Magma. *Journal of Geophysical Research-Solid Earth*, 124, 8281-8299.
- HEIKEN, G., WOHLLETZ, K. & EICHELBERGER, J. 1988. Fracture Fillings and Intrusive Pyroclasts, Inyo Domes, California. *Journal of Geophysical Research-Solid Earth and Planets*, 93, 4335-4350.
- HOLLAND, A. S. P., WATSON, I. M., PHILLIPS, J. C., CARICCHI, L. & DALTON, M. P. 2011. Degassing processes during lava dome growth: Insights from Santiaguito lava dome, Guatemala. *Journal of Volcanology and Geothermal Research*, 202, 153-166.
- HORNBY, A. J., KENDRICK, J. E., LAMB, O. D., HIROSE, T., DE ANGELIS, S., VON AULOCK, F. W., UMAKOSHI, K., MIWA, T., DE ANGELIS, S. H., WADSWORTH, F. B., HESS, K. U., DINGWELL, D. B. & LAVALLEE, Y. 2015. Spine growth and seismogenic faulting at Mt. Unzen, Japan. *Journal of Geophysical Research-Solid Earth*, 120, 4034-4054.
- HSUEH, C. H., EVANS, A. G. & MCMEEKING, R. M. 1986. Influence of multiple heterogeneities on sintering rates. *Journal of the American Ceramic Society*, 69, C-64-C-66.
- JAGOTA, A., BOYES, E. D. & BORDIA, R. K. 1992. Sintering of Glass Powder Packings with Metal Inclusions. *Synthesis and Processing of Ceramics : Scientific Issues*, 249, 475-480.
- JAGOTA, A., MIKESKA, K. R. & BORDIA, R. K. 1990. Isotropic constitutive model for sintering particle packings. *Journal of the American Ceramic Society*, 73, 2266-2273.
- JEAN, J. H. & GUPTA, T. K. 1992. Liquid-Phase Sintering in the Glass-Cordierite System - Particle-Size Effect. *Journal of Materials Science*, 27, 4967-4973.
- KENDRICK, J. E., LAVALLEE, Y., VARLEY, N. R., WADSWORTH, F. B., LAMB, O. D. & VASSEUR, J. 2016. Blowing Off Steam: Tuffisite Formation As a Regulator for Lava Dome Eruptions. *Frontiers in Earth Science*, 4.
- KOBBERGER, G. & SCHMINCKE, H. U. 1999. Deposition of rheomorphic ignimbrite D (Mogan Formation), Gran Canaria, Canary Islands, Spain. *Bulletin of Volcanology*, 60, 465-485.
- KOKELAAR, P. & KONIGER, S. 2000. Marine emplacement of welded ignimbrite: the Ordovician Pitts Head Tuff, North Wales. *Journal of the Geological Society*, 157, 517-536.
- KOLZENBERG, S., HEAP, M., LAVALLÉE, Y., RUSSELL, K., MEREDITH, P. & DINGWELL, D. B. 2012. The strength and permeability of tuffisite-bearing andesite in volcanic conduits.
- LAVALLEE, Y., BENSON, P. M., HEAP, M. J., FLAWS, A., HESS, K. U. & DINGWELL, D. B. 2012. Volcanic conduit failure as a trigger to magma fragmentation. *Bulletin of Volcanology*, 74, 11-13.

- LAVALLEE, Y., BENSON, P. M., HEAP, M. J., HESS, K. U., FLAWS, A., SCHILLINGER, B., MEREDITH, P. G. & DINGWELL, D. B. 2013. Reconstructing magma failure and the degassing network of dome-building eruptions. *Geology*, 41, 515-518.
- LEAT, P. T. & SCHMINCKE, H. U. 1993. Large-Scale Rheomorphic Shear Deformation in Miocene Peralkaline Ignimbrite-E, Gran-Canaria. *Bulletin of Volcanology*, 55, 155-165.
- LEPETIT, P., VIERECK-GOETTE, L., SCHUMACHER, R., MUES-SCHUMACHER, U. & ABRATIS, M. 2009. Parameters controlling the density of welded ignimbrites-A case study on the Incesu Ignimbrite, Cappadocia, Central Anatolia. *Chemie Der Erde-Geochemistry*, 69, 341-357.
- LINDOO, A., LARSEN, J. F., CASHMAN, K. V. & OPPENHEIMER, J. 2017. Crystal controls on permeability development and degassing in basaltic andesite magma. *Geology*, 45, 831-834.
- MACKENZIE, J. & SHUTTLEWORTH, R. 1949. A phenomenological theory of sintering. *Proceedings of the Physical Society. Section B*, 62, 833.
- MARON, S. H. & PIERCE, P. E. 1956. Application of Ree-Eyring generalized flow theory to suspensions of spherical particles. *Journal of colloid science*, 11, 80-95.
- MASON, B. G., PYLE, D. M. & OPPENHEIMER, C. 2004. The size and frequency of the largest explosive eruptions on Earth. *Bulletin of Volcanology*, 66, 735-748.
- MEDLIN, C. C., JOWITT, S. M., CAS, R. A. F., SMITHIES, R. H., KIRKLAND, C. L., MAAS, R. A., RAVEGGI, M., HOWARD, H. M. & WINGATE, M. T. D. 2015. Petrogenesis of the A-type, Mesoproterozoic Intra-caldera Rheomorphic Kathleen Ignimbrite and Comagmatic Rowland Suite Intrusions, West Musgrave Province, Central Australia: Products of Extreme Fractional Crystallization in a Failed Rift Setting. *Journal of Petrology*, 56, 493-525.
- MINAY, E. J., BOCCACCINI, A. R., VERONESI, P., CANNILLO, V. & LEONELLI, C. 2005. Sintering of metal fibre reinforced glass matrix composites using microwave radiation. *Advances in Applied Ceramics*, 104, 49-54.
- MUELLER, S., HELO, C., KELLER, F., TADDEUCCI, J. & CASTRO, J. 2018. First experimental observations on melting and chemical modification of volcanic ash during lightning interaction. *Scientific reports*, 8, 1-9.
- MULLER, R., EBERSTEIN, M., REINSCH, S., SCHILLER, W. A., DEUBENER, J. & THIEL, A. 2007. Effect of rigid inclusions on sintering of low temperature co-fired ceramics. *Physics and Chemistry of Glasses-European Journal of Glass Science and Technology Part B*, 48, 259-266.
- NEWHALL, C. G. & SELF, S. 1982. The Volcanic Explosivity Index (Vei) - an Estimate of Explosive Magnitude for Historical Volcanism. *Journal of Geophysical Research-Oceans*, 87, 1231-1238.
- NOGUCHI, S., TORAMARU, A. & NAKADA, S. 2008. Relation between microlite textures and discharge rate during the 1991-1995 eruptions at Unzen, Japan. *Journal of Volcanology and Geothermal Research*, 175, 141-155.
- OKUMURA, S., NAKAMURA, M., UESUGI, K., NAKANO, T. & FUJIOKA, T. 2013. Coupled effect of magma degassing and rheology on silicic volcanism. *Earth and Planetary Science Letters*, 362, 163-170.

- PAISLEY, R., BERLO, K., GHALEB, B. & TUFFEN, H. 2019. Geochemical constraints on the role of tuffisite veins in degassing at the 2008-09 Chaiten and 2011-12 Cordon Caulle rhyolite eruptions. *Journal of Volcanology and Geothermal Research*, 380, 80-93.
- PARIKH, N. 1958. Effect of atmosphere on surface tension of glass. *Journal of the American Ceramic Society*, 41, 18-22.
- PETFORD, N. 2009. Which effective viscosity? *Mineralogical Magazine*, 73, 167-191.
- PIOLI, L. & ROSI, M. 2005. Rheomorphic structures in a high-grade ignimbrite: The Nuraxi tuff, Sulcis volcanic district (SW Sardinia, Italy). *Journal of Volcanology and Geothermal Research*, 142, 11-28.
- QUANE, S. L. & RUSSELL, J. K. 2005. Welding: insights from high-temperature analogue experiments. *Journal of Volcanology and Geothermal Research*, 142, 67-87.
- QUANE, S. L., RUSSELL, J. K. & FRIEDLANDER, E. A. 2009. Time scales of compaction in volcanic systems. *Geology*, 37, 471-474.
- RAHAMAN, M.N., 2003. *Ceramic processing and sintering*. CRC press.
- RAHAMAN, M. N. & DEJONGHE, L. C. 1987. Effect of Rigid Inclusions on the Sintering of Glass Powder Compacts. *Journal of the American Ceramic Society*, 70, C348-C351.
- RAJ, R. & BORDIA, R. 1984. Sintering behavior of bi-modal powder compacts. *Acta Metallurgica*, 32, 1003-1019.
- RIEHLE, J. R. 1973. Calculated Compaction Profiles of Rhyolitic Ash-Flow Tuffs. *Geological Society of America Bulletin*, 84, 2193-2216.
- RUST, A., CASHMAN, K. & WALLACE, P. 2004. Magma degassing buffered by vapor flow through brecciated conduit margins. *Geology*, 32, 349-352.
- RUST, A. & CASHMAN, K. V. 2004. Permeability of vesicular silicic magma: inertial and hysteresis effects. *Earth and Planetary Science Letters*, 228, 93-107.
- RYAN, A. G., RUSSELL, J. K. & HEAP, M. J. 2018. Rapid solid-state sintering in volcanic systems. *American Mineralogist*, 103, 2028-2031.
- SAUBIN, E., TUFFEN, H., GURIOLI, L., OWEN, J., CASTRO, J. M., BERLO, K., MCGOWAN, E. M., SCHIPPER, C. I. & WEHBE, K. 2016. Conduit Dynamics in Transitional Rhyolitic Activity Recorded by Tuffisite Vein Textures from the 2008-2009 Chaiten Eruption. *Frontiers in Earth Science*, 4.
- SCHAUROTH, J., WADSWORTH, F. B., KENNEDY, B., VON AULOCK, F. W., LAVALLEE, Y., DAMBY, D. E., VASSEUR, J., SCHEU, B. & DINGWELL, D. B. 2016. Conduit margin heating and deformation during the AD 1886 basaltic Plinian eruption at Tarawera volcano, New Zealand. *Bulletin of Volcanology*, 78.
- SCHERER, G. W. 1987. Sintering with Rigid Inclusions. *Journal of the American Ceramic Society*, 70, 719-725.
- SCHERER, G. W. 1988. Viscous Sintering with a Pore-Size Distribution and Rigid Inclusions. *Journal of the American Ceramic Society*, 71, C447-C448.
- SCHIPPER, C. I., CASTRO, J. M., TUFFEN, H., JAMES, M. R. & HOW, P. 2013. Shallow vent architecture during hybrid explosive-effusive activity at Cordon Caulle (Chile, 2011-12):

Evidence from direct observations and pyroclast textures. *Journal of Volcanology and Geothermal Research*, 262, 25-37.

SMITH, R. L. 1960. Zones and zonal variations in welded ash flows.

SMITH, T. R. & COLE, J. W. 1997. Somers Ignimbrite Formation: Cretaceous high-grade ignimbrites from South Island, New Zealand. *Journal of Volcanology and Geothermal Research*, 75, 39-57.

SPARKS, R. S. J., MURPHY, M. D., LEJEUNE, A. M., WATTS, R. B., BARCLAY, J. & YOUNG, S. R. 2000. Control on the emplacement of the andesite lava dome of the Soufriere Hills volcano, Montserrat by degassing-induced crystallization. *Terra Nova*, 12, 14-20.

SPARKS, R. S. J., TAIT, S. R. & YANEV, Y. 1999. Dense welding caused by volatile resorption. *Journal of the Geological Society*, 156, 217-225.

SONG, W. J., LAVALLEE, Y., WADSWORTH, F. B., HESS, K. U. & DINGWELL, D. B. 2017. Wetting and Spreading of Molten Volcanic Ash in Jet Engines. *Journal of Physical Chemistry Letters*, 8, 1878-1884.

STASIUK, M. V., BARCLAY, J., CARROLL, M. R., JAUPART, C., RATTE, J. C., SPARKS, R. S. J. & TAIT, S. R. 1996. Degassing during magma ascent in the Mule Creek vent (USA). *Bulletin of Volcanology*, 58, 117-130.

STRECK, M. J. & GRUNDER, A. L. 1995. Crystallization and Welding Variations in a Widespread Ignimbrite Sheet - the Rattlesnake Tuff, Eastern Oregon, USA. *Bulletin of Volcanology*, 57, 151-169.

SUMNER, J. M. & BRANNEY, M. J. 2002. The emplacement history of a remarkable heterogeneous, chemically zoned, rheomorphic and locally lava-like ignimbrite: 'TL' on Gran Canaria. *Journal of Volcanology and Geothermal Research*, 115, 109-138.

TUFFEN, H. & DINGWELL, D. 2005. Fault textures in volcanic conduits: evidence for seismic trigger mechanisms during silicic eruptions. *Bulletin of Volcanology*, 67, 370-387.

TUFFEN, H., DINGWELL, D. B. & PINKERTON, H. 2003. Repeated fracture and healing of silicic magma generate flow banding and earthquakes? *Geology*, 31, 1089-1092.

UBIDE, T. & KAMBER, B. S. 2018. Volcanic crystals as time capsules of eruption history. *Nature Communications*, 9.

VAN DALEN, G. & KOSTER, M. 2012. 2D & 3D particle size analysis of micro-CT images. Unilever Res Dev Netherlands.

VASSEUR, J. & WADSWORTH, F. B. 2019. The Permeability of Columnar Jointed Lava. *Journal of Geophysical Research-Solid Earth*, 124, 11305-11315.

VASSEUR, J., WADSWORTH, F. B., LAVALLEE, Y., BELL, A. F., MAIN, I. G. & DINGWELL, D. B. 2015. Heterogeneity: The key to failure forecasting. *Scientific Reports*, 5.

VASSEUR, J., WADSWORTH, F. B., LAVALLEE, Y. & DINGWELL, D. B. 2016. Dynamic elastic moduli during isotropic densification of initially granular media. *Geophysical Journal International*, 204, 1721-1728.

VASSEUR, J., WADSWORTH, F. B., LAVALLEE, Y., HESS, K. U. & DINGWELL, D. B. 2013. Volcanic sintering: Timescales of viscous densification and strength recovery. *Geophysical Research Letters*, 40, 5658-5664.



- WADSWORTH, F. B. 2016. Densification of permeable liquids and magmas. Doctor of Philosophy Dissertation, Ludwig-Maximilians-Universität.
- WADSWORTH, F. B., VASSEUR, J., LLEWELLIN, E. W. & DINGWELL, D. B. 2017. Sintering of polydisperse viscous droplets. *Physical Review E*, 95.
- WADSWORTH, F. B., VASSEUR, J., LLEWELLIN, E. W., SCHAUROTH, J., DOBSON, K. J., SCHEU, B. & DINGWELL, D. B. 2016. Sintering of viscous droplets under surface tension. *Proceedings of the Royal Society a-Mathematical Physical and Engineering Sciences*, 472.
- WADSWORTH, F. B., VASSEUR, J., SCHAUROTH, J., LLEWELLIN, E. W., DOBSON, K. J., HAVARD, T., SCHEU, B., VON AULOCK, F. W., GARDNER, J. E. & DINGWELL, D. B. 2019. A general model for welding of ash particles in volcanic systems validated using in situ X-ray tomography. *Earth and Planetary Science Letters*, 525, 115726.
- WADSWORTH, F. B., VASSEUR, J., VON AULOCK, F. W., HESS, K. U., SCHEU, B., LAVALLEE, Y. & DINGWELL, D. B. 2014. Nonisothermal viscous sintering of volcanic ash. *Journal of Geophysical Research-Solid Earth*, 119, 8792-8804.
- WAPLES, D. W. & WAPLES, J. S. 2004. A review and evaluation of specific heat capacities of rocks, minerals, and subsurface fluids. Part 1: Minerals and nonporous rocks. *Natural resources research*, 13, 97-122.
- WHITE, M. J. & MCPHIE, J. 1997. A submarine welded ignimbrite crystal-rich sandstone facies association in the Cambrian Tyndall Group, western Tasmania, Australia. *Journal of Volcanology and Geothermal Research*, 76, 277-295.
- WINKEL, A., MESZAROS, R., REINSCH, S., MULLER, R., TRAVITZKY, N., FEY, T., GREIL, P. & WONDRACZEK, L. 2012. Sintering of 3D-Printed Glass/HAp Composites. *Journal of the American Ceramic Society*, 95, 3387-3393.
- YAN, Z., MARTIN, C. L., GUILLON, O. & BOUVARD, D. 2013. Effect of size and homogeneity of rigid inclusions on the sintering of composites. *Scripta Materialia*, 69, 327-330.